BRNO UNIVERSITY OF TECHNOLOGY

VYSOKÉ UČENÍ TECHNICKÉ V BRNĚ

FACULTY OF MECHANICAL ENGINEERING

FAKULTA STROJNÍHO INŽENÝRSTVÍ

INSTITUTE OF PHYSICAL ENGINEERING

ÚSTAV FYZIKÁLNÍHO INŽENÝRSTVÍ

IMAGING OF METAMAGNETIC THIN FILMS USING TEM

ZOBRAZOVÁNÍ METAMAGNETICKÝCH TENKÝCH VRSTEV POMOCÍ TEM

MASTER'S THESIS

DIPLOMOVÁ PRÁCE

AUTHOR
AUTOR PRÁCE
Bc. Jan Hajduček

SUPERVISOR
VEDOUCÍ PRÁCE
Ing. Vojtěch Uhlíř, Ph.D.

BRNO 2021

Master's Thesis Assignment

Institut:	Institute of Physical Engineering
Student:	**Bc. Jan Hajduček**
Degree programm:	Physical Engineering and Nanotechnology
Branch:	no specialisation
Supervisor:	**Ing. Vojtěch Uhlíř, Ph.D.**
Academic year:	2020/21

As provided for by the Act No. 111/98 Coll. on higher education institutions and the BUT Study and Examination Regulations, the director of the Institute hereby assigns the following topic of Master's Thesis:

Imaging of metamagnetic thin films using TEM

Brief Description:

Properties of multifunctional materials are closely linked to the subtle interplay of different order parameters. Transmission Electron Microscopy (TEM) is a unique technique to investigate the link between structure, chemical composition and magnetism on a nanometer scale. Advancing the magnetic imaging of both ferromagnetic and antiferromagnetic order using TEM will be a key prerequisite to explore control local magnetic configurations using strain and electric current.

Master's Thesis goals:

1. Preparation of samples of metamagnetic thin films and multilayers for imaging using TEM.
2. Imaging of the metamagnetic films by magnetic, structural, and chemical mapping.

Recommended bibliography:

COEY, J. M. D., Magnetism and magnetic materials. Cambridge University Press, Cambridge, (2009).

ALMEIDA, T. P. et al., Direct visualization of the magnetostructural phase transition in nanoscale FeRh thin films using differential phase contrast imaging. Physical Review Materials, vol. 4(3), pp. 034410, DOI:10.1103/PhysRevMaterials.4.034410, (2020).

CASTIELLA, M. et al., Structural investigation of magnetic FeRh epitaxial films. Materials Research Express, vol. 2(8), pp. 086401, DOI: 10.1088/2053-1591/2/8/086401, (2015).

Deadline for submission Master's Thesis is given by the Schedule of the Academic year 2020/21

In Brno,

L. S.

....
prof. RNDr. Tomáš Šikola, CSc.   doc. Ing. Jaroslav Katolický, Ph.D.
Director of the Institute   FME dean

Abstract

Complex magnetic materials at the nanoscale are essential in many areas of modern devices, such as digital memories or sensors. Novel technological approaches require the control and understanding of modern magnetic materials down to the atomic scale. One possibility is to exploit high-resolution transmission electron microscopy (TEM), characteristic for its outstanding subatomic resolution. This thesis investigates the options of TEM imaging of metamagnetic materials. These materials are characteristic by displaying coexistence of magnetic phases upon external control. Thin films of metamagnetic FeRh are used as an experimental platform to investigate the various aspects of TEM imaging. FeRh undergoes the metamagnetic phase transition from antiferromagnetic to ferromagnetic phase upon heating. We start with evaluating the sample fabrication processes suitable for our system, which is essential for successful TEM analysis. The differential phase contrast (DPC) technique in TEM is used for the magnetic analysis due to its direct access to the sample magnetic field configuration. An in-depth discussion of DPC signal formation is presented, which is crucial for understanding and analysis of resulting images. Furthermore, we perform structural, chemical, and particularly magnetic imaging of both magnetic phases present in FeRh. Finally, the process of in-situ heating of metamagnetic FeRh lamellae is presented.

Keywords

TEM, metamagnetism, FeRh, differential phase contrast, in-situ analysis.

Abstrakt

Komplexní magnetické materiály v nanoměřítku mají své nezastupitelné místo v moderních zařízeních, jako jsou digitální paměti nebo senzory. Moderní technologické procesy vyžadují porozumění a možnost kontroly moderních magnetických materiálů až na atomární úrovni. Jednou z možných cest je magnetická analýza za použití transmisní elektronové mikroskopie (TEM), která je unikátní díky možnosti zobrazování až v subatomárním měřítku. Tato práce popisuje možnosti zobrazování metamagnetických materiálů metodou TEM. Tyto materiály se vyznačují možností stabilizace více magnetických uspořádání najednou za daných vnějších podmínek. Modelovým systémem pro popis zobrazovacích možností metody TEM byly zvoleny tenké vrstvy metamagnetické slitiny FeRh. Tento materiál prochází při zahřívání fázovou přeměnou z antiferomagnetické do feromagnetické fáze. Podrobně jsou rozebrány procesy výroby vzorků, což je zásadní pro úspěšnou TEM analýzu. Pro magnetické zobrazování vzorků v TEMu je využita technika diferenciálního fázového kontrastu (DPC), umožňující přímé mapování rozložení magnetické indukce ve vzorku. Důsledně je diskutován vznik signálu v DPC, což je nezbytné pro porozumění a analýzu výsledných dat. FeRh vrstvy jsou podrobeny analýze struktury, chemického složení a především magnetických vlastností obou magnetických fází. Závěrem je představen proces přímého ohřevu metamagnetických vrstev v TEMu.

Klíčová slova

TEM, metamagnetismus, FeRh, diferenciální fázový kontrast, in-situ analýza.

I declare that I have written my master's thesis on the theme of *Imaging of metamagnetic thin films using TEM* independently, under the guidance of the supervisor Ing. Vojtěch Uhlíř, Ph.D., and using the sources quoted in the list of literature at the end of the thesis.

Bc. Jan Hajduček

First and foremost, I am extremely grateful to my supervisor Ing. Vojtěch Uhlíř, Ph.D. for his mentoring, continuous support, as well as for many intriguing and inspiring discussions.

I would like to extend my appreciation to the whole group of *Nanomagnetism and spintronics* at CEITEC. Namely, I want to thank M.Sc. Jon Ander Arregi, Ph.D. for his willingness to help whenever needed. I would also like to thank Ing. Michal Horký and Dr. Michal Staňo for all valuable discussions and for making the uniquely familial atmosphere. I gratefully acknowledge Ing. Marek Vaňatka, Ph.D. for his assistance with TEM experiments and the sample fabrication processes. I also address my acknowledgement to Ing. Lucie Motyčková for providing me valuable advice concerning wet chemical etching.

My deep appreciation goes to Ing. Jan Michalička for his willingness, patience, and his valuable advice considering the TEM operation. I would also like to recognize the assistance of Ing. Ondřej Man, Ph.D. considering the TEM sample fabrication.

I am deeply indebted to my family for their encouragement and support through my studies and on whom I could rely throughout my whole life.

<div align="right">Bc. Jan Hajduček</div>

Contents

Introduction

Research of magnetic materials during the last decades brought a vast amount of new technologies, which led to significant performance enhancement in data storage, sensors, and other technologies, where magnetic materials are used at the nanoscale. Besides the new research areas like spintronics [1, 2] or magnonics [3, 4], there are many other application branches of nanomagnetic research, such as utilizing magnetic nanoparticles in biological research [5].

More than one magnetic ordering can be stabilized in magnetic phase transition materials upon varying internal material properties or external conditions. We are particularly interested in materials undergoing *metamagnetic phase transition* (MPT) between *antiferromagnetic* (AF) and *ferromagnetic* (FM) phase. A group of FM materials represents a traditional branch of magnetic materials that are well understood and easily controllable. However, their theoretical performance is fundamentally limited in data storage density, or magnetization dynamics rate [2]. AF materials represent a large group of magnetically ordered materials, that do not possess macroscopic magnetization. Their internal antiparallel alignment of atomic moments allows potentially higher data storage densities and considerably faster dynamics compared to FM materials [6]. The external control and readout of their magnetic state are limited due to the lack of macroscopic magnetization and stray fields, making their external control far more challenging than FM. Access to both of these magnetic states in MPT materials brings new options in the field of magnetic recording [7], spintronic devices [8], or magnetic caloritronics [9, 10].

Using such systems for applications requires deep understanding of individual magnetic phases and their mutual correlation upon phase transition. The whole variety of properties can be revealed by direct imaging of these magnetic phases. There are only a few experimental techniques sensitive to the AF signal. They are either source demanding, e.g., synchrotron X-ray sources, or their spatial resolution is limited, e.g., optical imaging. Atomic-scale imaging of individual AF moments would help to uncover internal properties of AF. One of the few magnetism-sensitive techniques capable of atomic resolution is *transmission electron microscopy* (TEM). This well-developed technique is unique for its subatomic resolution and its comprehensive usability, ranging from structural and chemical analysis to magnetic analysis and beyond. Due to the current advances in *high resolution* (HR) TEM imaging, a growing number of attempts to merge HR-TEM imaging with magnetism led to the first experimental publication dealing with atomic-scale TEM magnetic analysis of AF [11]. Combined with well-developed imaging of FM materials, TEM represents a unique analyzing technique for MPT materials.

This thesis brings an overview study towards TEM magnetic analysis of MPT materials, focusing on novel AF phase imaging. HR imaging results are therefore applicable also for pure AF materials. Thin layers of FeRh alloy are used as a reference system for TEM magnetic analysis. Equiatomic FeRh undergoes MPT close to the room temperature from AF to FM phase upon heating. Among several magnetism-sensitive techniques in TEM, we focus on *differential phase contrast* (DPC) [12] imaging, and the majority of the TEM imaging theory presented is linked to the fundamentals of this particular technique. DPC is currently intensely developed not only for magnetic imaging but also for electric field mapping and more advanced associated techniques, such as integrated DPC [13].

Experimentally, the sample fabrication and data interpretation play a dominant role in TEM analysis. Sample fabrication appears to be one of the most crucial factors de-

fining the final quality of TEM imaging. Several approaches of TEM sample fabrication suitable for thin film analysis have been historically developed. The main differentiating factors are final specimen structural damage, resulting geometry, and fabrication process convenience. These factors of TEM sample fabrication processes are experimentally tested on our particular MPT system. As for the TEM characterization, we cover DPC signal formation, structural analysis of FeRh thin layer systems, possibilities of magnetic imaging of the AF phase, and the novel approach of in-situ control of thin layers in TEM. Achieved results contribute to the current development of TEM magnetic imaging and experimental analysis of complex MPT materials.

The thesis is divided into four chapters. Chapter 1 briefly covers fundamentals of nanomagnetism, magnetic orderings in solids, and most importantly, the internal structure of FM and AF materials required to understand magnetic features observed in TEM. Chapter 2 is dedicated to the general principles of TEM, where we briefly cover the TEM setup, operation modes, image formation, and sample fabrication strategies. Electron interaction with internal electric and magnetic fields in a specimen and their implications to TEM magnetic imaging are covered in chapter 3 together with the state-of-the-art of magnetic imaging in TEM. Finally, chapter 4 summarizes the experimental results of the thesis.

1. Basics of nanomagnetism

Deep understanding of the physical processes in magnetic materials starting from the atomic level up to the macroscale is essential for potential applications of magnetic materials. This chapter briefly summarizes the origin of magnetic properties in solids from the atomic level up to the macroscale, together with different magnetic fields used for such description. A detailed description of these phenomena is widely covered in multiple magnetism theory-related books [14, 15, 16], therefore only a summary is presented. The main focus of this thesis is the TEM imaging of materials undergoing MPT between FM and AF phases. Description of the features observable within these phases and their origin is therefore crucial for successful data interpretation.

1.1. Origin of magnetism in solids

Magnetic properties in materials are mainly determined by electron properties in solids[1]. Magnetic moment is fundamentally linked to the angular momentum [17]. The angular momentum has two components - the *orbital magnetic moment* $\boldsymbol{m}_{\mathrm{orb}}$ and the *spin magnetic moment* $\boldsymbol{m}_{\mathrm{s}}$. Classically, the orbital contribution can be calculated in terms of the orbiting electron around the core combined with the fact that angular momentum is quantized. Based on these assumptions, we get [14]

$$\boldsymbol{m}_{\mathrm{orb}} = -e/(2m_{\mathrm{e}})\boldsymbol{l}, \tag{1.1}$$

where $\boldsymbol{l}$ stands for the orbital angular momentum of an electron, e is an elementary charge, and m_{e} is an electron mass[2]. The spin magnetic moment is a purely quantum property of elementary particles and can be calculated as [14]

$$\boldsymbol{m}_{\mathrm{s}} = -e/(m_{\mathrm{e}})\boldsymbol{s}, \tag{1.2}$$

where $\boldsymbol{s}$ is a spin angular momentum of an electron. Interaction connecting these two contributions is called *spin-orbit coupling*, which gives rise to the total angular moment of a single electron atom $\boldsymbol{j} = \boldsymbol{l} + \boldsymbol{s}$ [14].

In multiple electron atoms, the electron-electron interaction takes place, which complicates the system significantly. Hund's rules can empirically predict the magnetic ground state of a multielectron atom. Based on these rules, we get the spin, orbital, and total angular momentum of a single multielectron atom $\boldsymbol{S}, \boldsymbol{L}$ and $\boldsymbol{J}$, respectively. The total magnetic moment of an atom $\boldsymbol{m}$ can be calculated as

$$\boldsymbol{m} = -(\mu_{\mathrm{B}}/\hbar)(\boldsymbol{L} + 2\boldsymbol{S}), \tag{1.3}$$

where $\mu_{\mathrm{B}} = e\hbar/(2m_{\mathrm{e}})$ is a Bohr magneton, which is typically used as a fundamental unit for an atomic magnetic moment [14].

Formation of the magnetic ordering in solids is a complex process, where lattice periodicity, mutual arrangement of atomic orbitals, material band structure of the material,

---

[1]Nucleus contribution can be neglected due to its much higher mass compared to the electron.

[2]Although the classical approach is an oversimplified model, the result is equivalent to the rigorous quantum mechanical model.

and other solid-state factors have to be considered [18]. Even the interfaces between adjacent materials play an essential role at a nanoscale level, especially in thin-film geometries. For a macroscopic description of magnetic materials, we approximate atomic moments by a continuous variable called magnetization $\boldsymbol{M}$ defined as

$$\boldsymbol{M} = \frac{\sum_i \boldsymbol{m}_i}{V}, \tag{1.4}$$

where V is the specimen volume that the magnetic moments $\boldsymbol{m}_i$ are averaged over. Magnetization $\boldsymbol{M}$ then appears in material relations of Maxwell equations, which are together with the accompanying magnetic fields introduced in the following section 1.2 and used for the characterization of magnetic orderings.

1.2. Magnetic fields in matter

Previously, we introduced the origin of magnetic moment in materials and the accompanied variable magnetization. These moments form magnetic field distribution, where we define the *magnetic field* $\boldsymbol{B}$ with the SI unit of T (Tesla), the *magnetic field strength* $\boldsymbol{H}$ with the SI unit of A/m and the *magnetization* $\boldsymbol{M}$ with the SI unit of A/m, which was introduced in the previous section.

Maxwell equations describe electromagnetic field distributions, and one of them, the Gauss law of magnetism, reads [14]

$$\nabla \cdot \boldsymbol{B} = 0. \tag{1.5}$$

The divergence-less $\boldsymbol{B}$-field implies non-existence of magnetic field monopoles and an alternative possibility to express the $\boldsymbol{B}$-field via the magnetic vector potential $\boldsymbol{A}$, where $\boldsymbol{B} = \nabla \times \boldsymbol{A}$. At the classical level, field and potential approaches are equivalent; however, in quantum mechanics, only the field description through the magnetic potential $\boldsymbol{A}$ is complete, as shown by Aharonov and Bohm in 1959 [19].

Interaction of charged particles with a magnetic field is the key for analysis and imaging of magnetic materials. This interaction is in classical mechanics described in terms of the Lorentz force $\boldsymbol{F}_{\mathrm{L}}$ as

$$\boldsymbol{F}_{\mathrm{L}} = q\boldsymbol{v} \times \boldsymbol{B}, \tag{1.6}$$

where q and $\boldsymbol{v}$ are the particle charge and velocity, respectively.

Another approach to describe magnetic field is through the $\boldsymbol{H}$-field. In free space, there is only a constant μ_0 connecting $\boldsymbol{H}$-field and $\boldsymbol{B}$-field as $\boldsymbol{B} = \mu_0\boldsymbol{H}$. However, in a magnetic material, the magnetization contribution to the total magnetic field has to be considered, and we get

$$\boldsymbol{B} = \mu_0(\boldsymbol{H} + \boldsymbol{M}). \tag{1.7}$$

Different properties of the $\boldsymbol{H}$-field compared to $\boldsymbol{B}$-field allow us to define magnetic charges ρ_{m} analogously to electrostatics as

$$\nabla \cdot \boldsymbol{H} = -\nabla \cdot \boldsymbol{M} = \frac{\rho_{\mathrm{m}}}{\mu_0}. \tag{1.8}$$

In a finite, uniformly magnetized block, we get a non-zero magnetic charge only at the magnetic body surface. These charges form the demagnetizing field $\boldsymbol{H}_\text{d}$ pointing against sample magnetization $\boldsymbol{M}$.

Response of the sample magnetization $\boldsymbol{M}$ to the applied magnetic field $\boldsymbol{H}_\text{ext}$ is described via the dimensionless susceptibility tensor $\widehat{\chi}$, defined as

$$\boldsymbol{M} = \widehat{\chi}\boldsymbol{H}_\text{ext}. \tag{1.9}$$

1.3. Energy contributions in magnetism

Stable configurations of specimen magnetization in solids can be efficiently derived from minimization of the total system energy ϵ taking the form of

$$\epsilon = \epsilon_\text{Z} + \epsilon_\text{ex} + \epsilon_\text{d} + \epsilon_\text{a} + \dots \tag{1.10}$$

where Zeeman energy ϵ_Z, exchange energy ϵ_ex, dipolar energy ϵ_d, and anisotropy energy ϵ_a are the dominant magnetization-dependent energy contributions of the system [14]. Individual terms are described in the following text.

Zeeman energy

Interaction of the magnetization $\boldsymbol{M}$ of the sample volume V with the external magnetic field $\boldsymbol{H}_\text{ext}$ is characterized by Zeeman energy [14]

$$\epsilon_\text{Z} = -\mu_0 \iiint_V \boldsymbol{M} \cdot \boldsymbol{H}_\text{ext}\, d^3\boldsymbol{r}. \tag{1.11}$$

This component tends to align sample magnetization with the external magnetic field direction.

Exchange energy

Exchange interaction couples adjacent atomic moments in solids while forming long-range magnetic ordering, which becomes dominant in FM and AF materials. Exchange interaction is described by the Hamiltonian [14]

$$\hat{\boldsymbol{H}}_\text{ex} = \sum_{i,j \neq i} J_{ij} \hat{\boldsymbol{S}}_{\boldsymbol{i}} \cdot \hat{\boldsymbol{S}}_{\boldsymbol{j}}, \tag{1.12}$$

where J_{ij} is an exchange constant between atomic moments $\hat{S}_i$ and $\hat{S}_j$. In FM materials, $J_{ij} > 0$ leads to parallel alignment of magnetic moments, while the antiparallel coupling is caused by $J_{ij} < 0$ in AF. In a continuous magnetization approximation, the exchange energy ϵ_ex can be expressed as [14]

$$\epsilon_\text{ex} = \iiint_V A \left(\nabla \frac{\boldsymbol{M}}{M_\text{s}} \right)^2 d^3\boldsymbol{r}, \tag{1.13}$$

where A is an exchange stiffness constant, M_s represents saturation magnetization, and integration goes over the sample volume V.

Dipolar energy

Dipolar interaction between magnetic dipoles throughout the whole sample volume V contributes to the sample demagnetizing field $\boldsymbol{H}_\mathrm{d}$. Interaction of this field with sample magnetization $\boldsymbol{M}$ is described by [14]

$$\epsilon_\mathrm{d} = -\frac{\mu_0}{2} \iiint_V \boldsymbol{M} \cdot \boldsymbol{H}_\mathrm{d} \, d^3\boldsymbol{r}, \qquad (1.14)$$

where demagnetizing field $\boldsymbol{H}_\mathrm{d}$ can be calculated from the concept of magnetic charges introduced in section 1.2.

Anisotropy energy

Sample magnetization tends to be aligned along certain directions known as *easy axes* (EA). The minimum-energy orientations are associated with the *shape anisotropy* and *magneto-crystalline anisotropy*. The geometry of the magnetic specimen determines the distribution of magnetic charges forming the demagnetizing field and stray field. Optimization of these charges results in shape anisotropy. Lattice properties and the electronic orbital structure forms EA along specific crystallographic directions. Both of these terms contribute to the anisotropy energy, which in the uniaxial case takes the form of [14]

$$\epsilon_\mathrm{a} = \iiint_V K_\mathrm{u} \sin^2 \theta \, d^3\boldsymbol{r}, \qquad (1.15)$$

where K_u is a uniaxial anisotropy coefficient and θ is the angle between the $\boldsymbol{M}$ and EA direction.

1.4. Magnetic orderings in solids

Several magnetic orderings can be distinguished based on the material atomic magnetic moments, their mutual interactions, and other solid-state properties. The major classes are *diamagnets, paramagnets* (PM), *ferromagnets* (FM) and *antiferromagnets* (AF). Properties of the last two types are essential for this thesis and thereby further discussed.

1.4.1. Ferromagnetic materials

Exchange interaction-driven parallel alignment of neighboring atomic moments in FM materials forms non-zero local magnetization, which characterizes FM ordering. Metallic FM are typically described by two simplified models, the *Stoner model* and *s-d model*. More advanced models are based on density functional theory (DFT) calculations [20].

The *Stoner model* assumes that both spin up and spin down electrons in the electronic band structure exhibit a free electron dispersion. In the case of high electron density at the Fermi level [18] combined with the strong exchange interaction, it may be favorable to split the ↑ and ↓ spin bands. The presence of spin polarization in electron populations induces spontaneous non-zero magnetization, which is characteristic of FM ordering. The Stoner criterion for band splitting is met only by Fe, Co, and Ni in the periodic table [21].

The *s-d model* considers s-orbital band electrons as delocalized, hence mainly representing the conduction electrons, and d-band electrons as localized. Therefore, the molecular field splits only the localized d-band, which is then responsible for the FM properties of the material. This model works well for transition metals [14].

The effect of external magnetic field H on the FM magnetization M is characterized by the hysteresis loop, with a typical profile shown in Figure 1.1 **(a)**. The hysteresis loop consists of a virgin branch starting from the zero field and going to the saturated value of magnetization M_s upon growing magnetic field. By reducing H back to the zero value, we obtain the remanent magnetization M_r state. By further increasing H in the opposite direction, we reach the coercive field, characterized by $M(H = H_c) = 0$.

Thermal stability of FM susceptibility is limited by the transition point at Curie temperature T_C, above which the thermal fluctuations overcome the exchange energy, and the material becomes paramagnetic. For $T < T_C$ the $\chi_{FM}(T)$ dependence is complex and material dependent, however for $T > T_C$, it follows the Curie - Weiss law in the form of [14]

$$\chi_{FM}(T > T_C) \propto \frac{1}{T - T_C}, \tag{1.16}$$
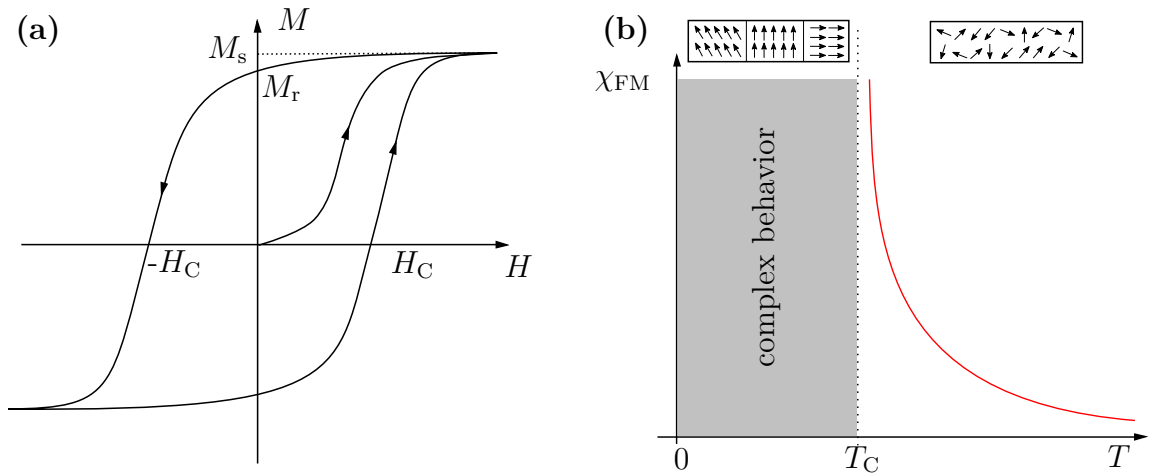
which is shown in Figure 1.1 **(b)**.

Figure 1.1: FM response to applied magnetic field. (a) Ferromagnetic hysteresis loop. Green virgin branch characterizes the response of demagnetized FM, which is followed by hysteresis loops describing FM magnetization upon applied field cycling. **(b)** Thermal dependence of FM susceptibility $\chi_{FM}(T)$. Below the Curie temperature FM shows large susceptibility, while above the Curie temperature FM undergoes a transition to the paramagnetic state, which is described by the Curie - Weiss law.

Another way of FM material control is via passing a spin-polarized current. Spin polarization of conduction electrons is generally induced in FM due to spin splitting of density of bands at the Fermi level [18]. Accompanied transfer of angular momentum from conduction electrons to the FM is capable of magnetization reversal in FM [20]. Utilizing the spin degree of freedom on top of the charge is characteristic for the rapidly evolving field of spintronics [1, 22]. Well-established control of FM states makes them the most widely used magnetic order in applications, such as magnetic memories [23], magnetic

sensors [24], or even nanoparticles in bioresearch [5]. Besides those, novel approaches to application of FM have been developed, such as the racetrack memory [25], skyrmion-based memory [26], information transfer via magnons [3], etc.

Imaging of magnetization features in FM gives us deep insight into the studied material, which is essential for FM applications. Typical topological magnetization features present in FM are covered in the following section.

Magnetic features in FM

Successful data interpretation of FM material imaging requires an understanding of FM magnetization objects formed by energy balance described in section 1.3. On top of the *exchange interaction* aligning the neighboring moments, *dipolar interaction* leads to the splitting of the uniformly magnetized region into *magnetic domains*. These regions of parallel aligned magnetic moments represent the main features observable in FM samples. Anisotropy further modifies domain geometry.

Magnetic field properties expressed by equations (1.5) and (1.7) indicate that closed magnetization structures tend to appear in nature. An example of field distribution in a homogenously magnetized FM rod is shown in Figure 1.2 **(a)** demonstrating the relation between individual quantities describing the magnetic state of a FM body.
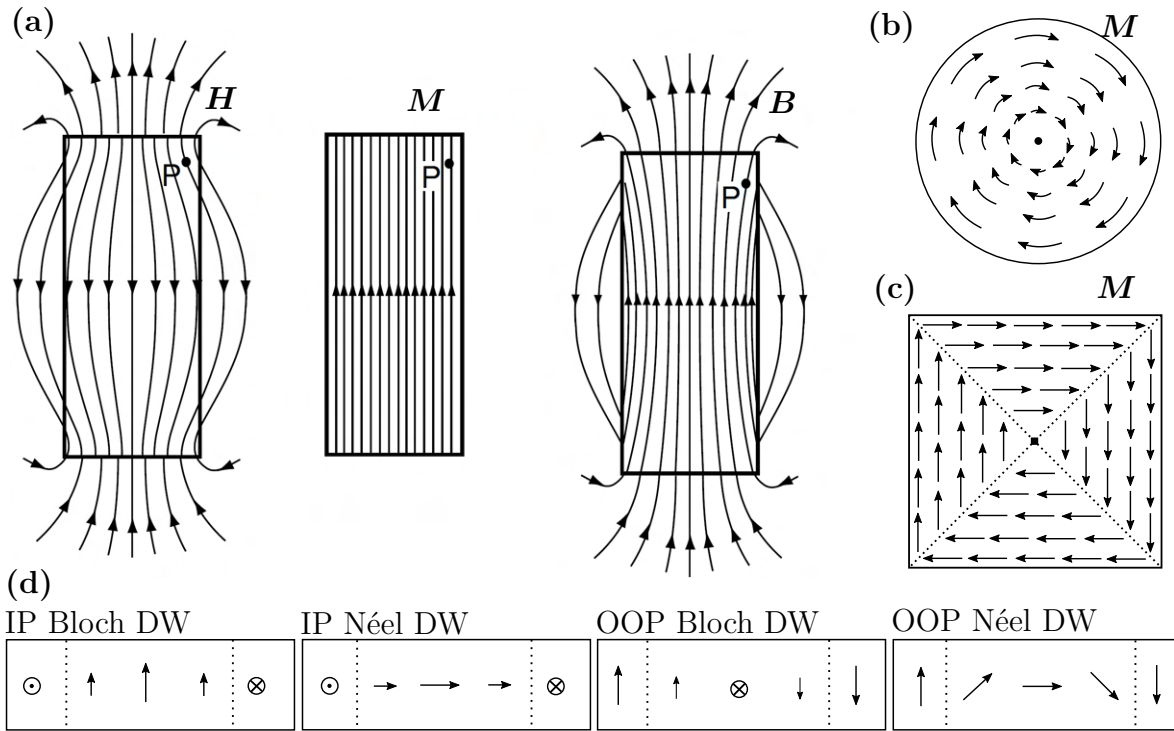

Figure 1.2: Magnetization structures in FM. (a) Distributions of **H**-, **M**- and **B**-field distributions formed by a homogenously magnetized FM rod. Adapted from [14]. **(b)** The magnetization distribution of **(b)** the vortex, **(c)** Landau pattern, respectively. **(d)-(g)** Side views of possible DW magnetization profiles in IP and OOP magnetized FM thin films [15].

B-field and **H**-field distributions associated with the magnetization should be considered for magnetic imaging. Examples of closed magnetization layouts, such as the

Landau pattern [27] or vortex [28] can be found in Figure 1.2 **(b)** and **(c)**. Landau patterns appear in rectangular structures, whereas vortex-like structures are favored in the circularly shaped samples.

Neighboring domains in FM are separated by a *domain wall* (DW), with a magnetization profile defined by particular material and sample geometry. DWs in FM thin films are of Bloch type or Néel type [15], whose magnetization profiles for *in-plane* (IP) and *out-of-plane* (OOP) magnetized thin films are shown in Figure 1.2 **(d)-(g)**. Magnetostatically, the Bloch DW is more stable because this profile does not contribute to dipolar energy. The Néel type is generally favorable in the presence of a chiral interaction, such as the Dzyaloshinskii-Moriya interaction [29].

Imaging of FM materials

Imaging of magnetization features in FM helps us to reveal the internal magnetic properties of studied objects. Several imaging techniques have been historically developed, unveiling different aspects of FM materials. The most conventional ones are briefly summarized in Table 1.1

Table 1.1: Comparison of FM imaging techniques. For each technique, we mention the imaging medium, effect standing behind the FM signal formation, approximate lateral resolution r, typical detection depth d, and sample preparation process required for imaging [30]. Meanings of the used abbreviations: Photoemission electron microscopy (PEEM), X-ray magnetic circular dichroism (XMCD), Magnetic force microscopy (MFM), Scanning probe microscopy (SPM), Light microscopy (LM), Magneto-optical Kerr effect (MOKE), Scanning electron microscopy with polarization analysis (SEMPA).

Technique	Im. medium	Mag. detection effect	r (nm)	d (nm)	Sample prep.
PEEM	X-ray	XMCD	10^1	10^0	surface cleaning
MFM	SPM	Dipolar int.	10^0	-	-
LM	Light	MOKE	10^2	10^1	-
SEMPA	Electrons	Spin dep. scattering	10^1	10^0	surface cleaning
TEM	Electrons	El. deflection by $\boldsymbol{F}_\mathrm{L}$	10^0	-	el. transparency

1.4.2. Antiferromagnetic materials

Antiferromagnetic materials (AF) are a large group of magnetic materials with dominating antiparallel exchange interaction. Such alignment of atomic moments is manifested by zero magnetization. In the early '30s, Louis Néel studied materials that included magnetic atoms but did not possess typical magnetic behavior. Later on, he came up with a concept of antiparallel molecular field, capable of forming materials with such properties [31]. During his Nobel speech in 1970, he described them as "interesting, but useless" [32], which was the common perception for AF during the last century. However, this is not the case anymore since AF materials are now conventionally used as passive elements in the hard-disk drives due to the exchange bias effect [33]. AF are considered a future candidate for ultrafast computational devices and memories due to their insensitivity to the external field and the orders of magnitude faster dynamics than FM [6]. Several AF-based research branches have evolved within the last decade, such as AF magnonics [4],

research of AF insulators [34], AF semiconductors [35], and AF metals [36]. However, the leading topic is the electrical control of AF materials [37, 38, 39], which is essential for AF spintronic applications. General properties of AF are described in this section together with the options of their external control.

The antiparallel exchange allows multiple configurations of magnetic moments, allowing the cancellation of overall magnetization. Based on these AF lattices can be generally *collinear* and *non-collinear*. Collinear AF is characterized by two antiparallel magnetic lattices pointing against each other, while a larger number of sublattices can be found in non-collinear AF. The last configuration considered as AF is the so-called *synthetic AF* (SAF), in which antiparallel coupling occurs between adjacent FM layers [40]. Such coupling is mediated via a thin non-magnetic interlayer, due to the Ruderman-Kittel-Kasuya-Yosida interaction [41]. The rest of the thesis deals only with the simplest coplanar, collinear AF. The schemes of AF categories listed above are shown in Figure 1.3.
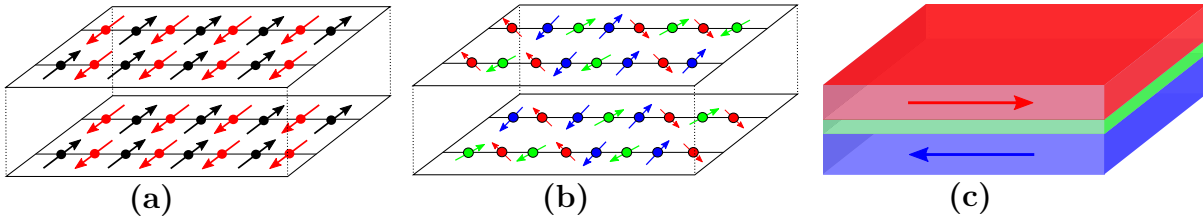

Figure 1.3: Groups of AF materials. Typical spin configuration layout of **(a)** collinear AF lattice, **(b)** non-collinear AF lattice, respectively. **(c)** Scheme of a typical SAF layout.

In collinear AF exchange field might be described in terms of antiparallel molecular field effectively reaching up to $\mu_0 H_{\mathrm{ex}} \sim 10^2$ T [14]. Exchange interaction is responsible for the formation of two magnetic sublattices, whose magnetizations $\boldsymbol{M}_1$ and $\boldsymbol{M}_2$ point against each other. We also define the so-called Néel vector $\boldsymbol{L}$ as $\boldsymbol{L} = \boldsymbol{M}_1 - \boldsymbol{M}_2$.

Another effect defining the direction of $\boldsymbol{L}$ is magnetocrystalline anisotropy[3]. AF anisotropy can be characterized by effective magnetic field in the range of $\mu_0 H_{\mathrm{an}} \sim 10^0$ T [42].

Such strong internal interactions imply ultrafast spin dynamics of AF, where the AF resonance frequency ω is proportional to AF internal fields as $\omega \propto (H_{\mathrm{ex}} H_{\mathrm{an}})^{1/2}$ and reaches the THz range [4]. The dynamic behavior of AF make these systems an ideal candidate for ultrafast computational devices and memories.

The last characteristic field appearing in AF material is the so-called spin-flop field $\mu_0 H_{\mathrm{sf}}$. Spin flop is a state in which applied field $\boldsymbol{H}_{\mathrm{ext}}$ is strong enough to distract antiparallel alignment of sublattices and tilt them slightly along the magnetic field direction. Consequently, non-zero magnetization is induced upon large external fields applied in AF. Effective spin-flop field is in the order of $\mu_0 H_{\mathrm{sf}} \sim 10^1$ T [42].

The main variable defining the effect of external magnetic field on a magnetic material is the AF susceptibility χ_{AF}, which is generally dependent on the applied field direction with respect to $\boldsymbol{L}$. Schematic definition of $\chi_\perp$ and $\chi_\parallel$ is shown in Figure 1.4 **(a)**. Analogously to FM materials, AF lose their magnetic order above a certain temperature, called the *Néel temperature* T_{N}, and become paramagnetic. Temperature dependence of AF $\chi_\parallel$ and $\chi_\perp$ is shown in Figure 1.4 **(b)**. Since the internal characteristic fields of AF ex-

---

[3]Shape anisotropy is not present in AF due to the lack of macroscopic dipolar interaction, which is proportional to the sample magnetization $\boldsymbol{M}$, that is not present in AF.
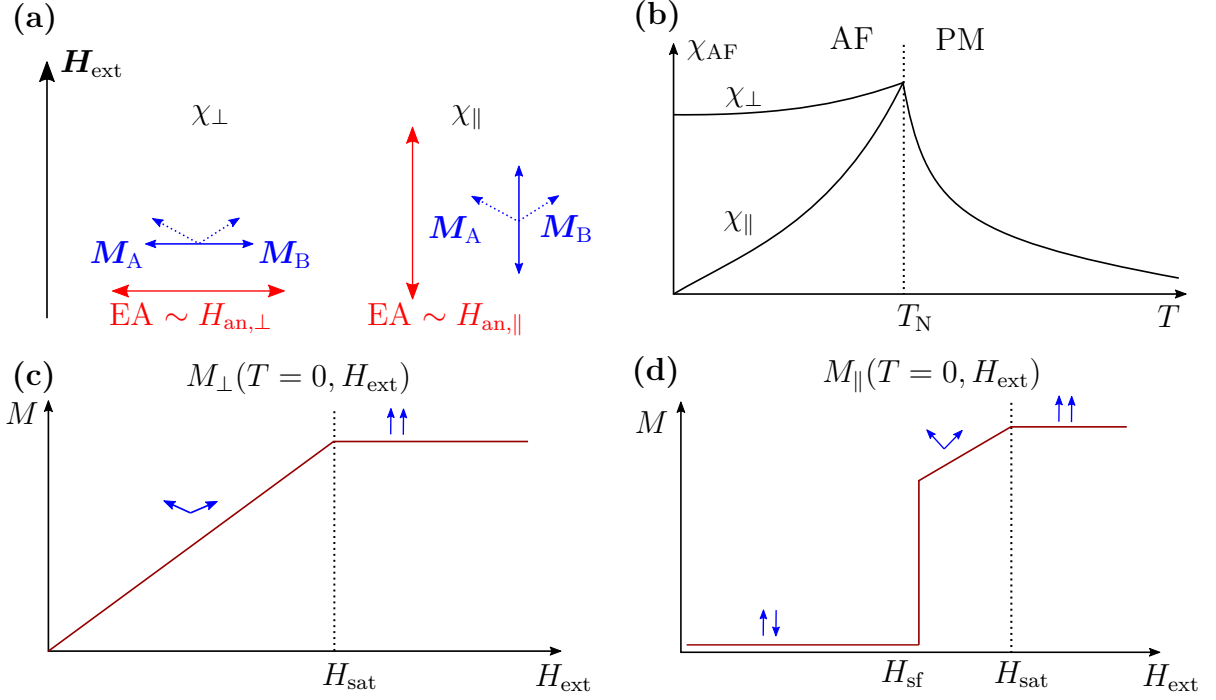
Figure 1.4: Temperature and field dependence of AF susceptibility χ. (a) Definitions of the $\chi_\parallel$ and $\chi_\perp$. **(b)** Thermal dependence of χ_{AF} for external fields $\boldsymbol{H}_{ext}$ directions shown in **(a)**. Evolution of AF magnetization on external field strength for zero temperature are indicated in **(c)** for $\boldsymbol{H}_{ext} \perp \boldsymbol{L}$ and in **(d)** for $\boldsymbol{H}_{ext} \parallel \boldsymbol{L}$.

ceeds usual laboratory fields, AF materials are highly resistant to external magnetic field. However, large fields in the orders of 10^0 T are approachable and can cause deviations of magnetic moments from the ground state. Effects of strong magnetic fields on AF magnetization at zero temperature are shown in Figure 1.4 **(c)** for $\boldsymbol{H}_{ext} \perp \boldsymbol{L}$ and in **(d)** for $\boldsymbol{H}_{ext} \parallel \boldsymbol{L}$. Saturation field H_{sat} corresponds to the state when field is strong enough to reach parallel orientation of AF sublattices and in **(d)** H_{sf} is the spin-flop field, which is dependent on anisotropy strength. For $H_{an} = 0$ **(c)** and **(d)** dependencies would be identical. The main effect appearing in the external fields of 10^0 T is a change of the Néel vector with respect to the external magnetic field direction, which is highly dependent on the AF anisotropy direction and the field strength [15].

Magnetic features in AF

Exchange interaction in AF forms regions with the unified ordering of atomic moments and constant Néel vector $\boldsymbol{L}$, called *AF domains*, which are separated by domain walls. Due to the lack of dipolar interaction in AF, the domain formation is generally different, but the concept of competition between exchange and anisotropy energies is preserved. The study of the AF domains and domain walls properties has been addressed theoretically [43, 44]; however, experimental evaluation remains extremely challenging [11, 45]. The complexity of moments in AF domains escalates because there are multiple ways of atomic moments ordering, leading to zero magnetization. These options of atomic moment configurations in simple cubic lattice are shown in Figure 1.5 **(a)** - **(d)**. G-type of AF ordering shown in Figure 1.5 **(d)** is the most common one due to its lowest exchange energy [15]. On

(a) A-type   **(b)** C-type   **(c)** E-type   **(d)** G-type

(e) k-domains   **(g)** Antiphase

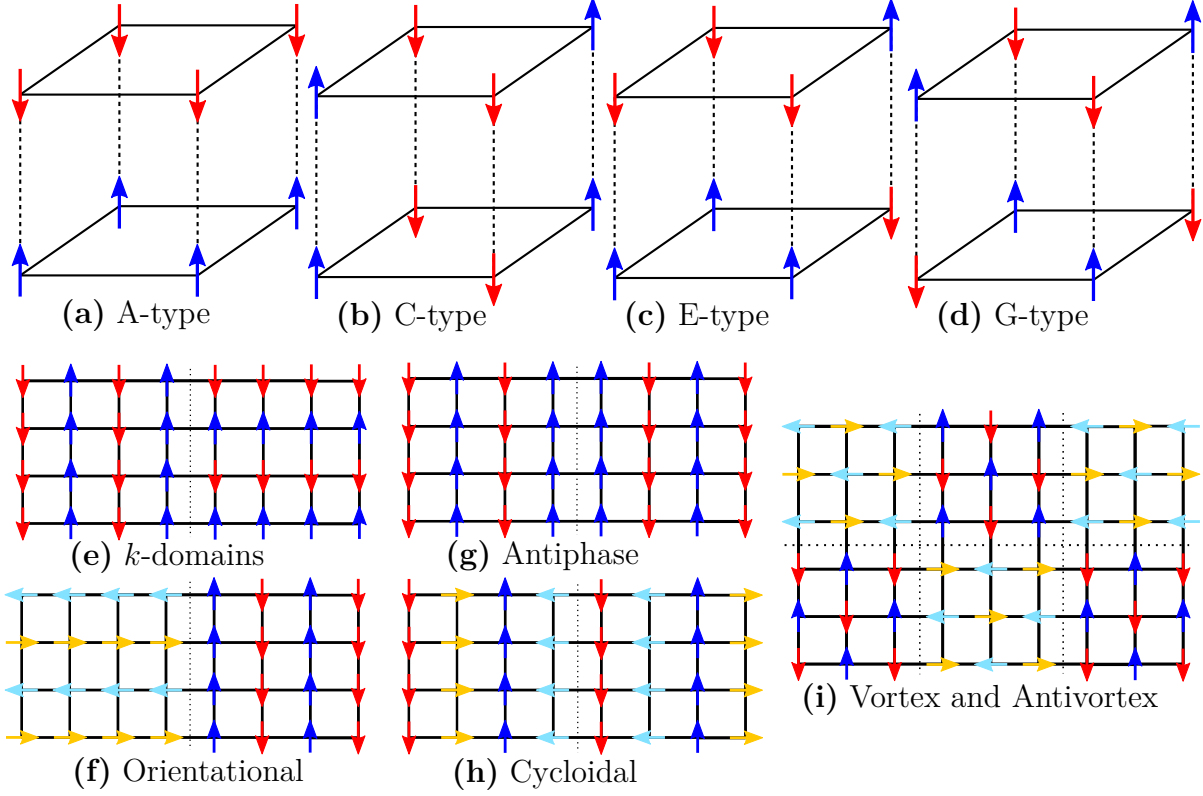**(f)** Orientational   **(h)** Cycloidal   **(i)** Vortex and Antivortex

Figure 1.5: AF domains and DW in a simple cubic lattice. (a) - **(d)** Four types of atomic moments ordering in AF with a simple cubic lattice [15]. **(e)** - **(i)** Different types of DW separating AF domains. Adapted from [46].

top of that, several types of DW profiles connecting these domains can be formed as schematically shown in Figure 1.5 **(e)** - **(i)**.

AF ordering of magnetic moments together with the Néel vector $\boldsymbol{L}$ defines the AF magnetic cofiguration. While AF antiparallel ordering of atomic moments is driven by exchange interaction, the $\boldsymbol{L}$-direction is determined mainly by an external magnetic field and magnetocrystalline anisotropy. Generally, atomic moments tend to align with specific crystallographic directions in the crystal, linked to the lattice properties, electronic structure of the studied material, and nuclear orbitals [14]. Therefore modifications of such solid-state properties might affect the magnetic properties. Since AF interaction mostly appears in epitaxially grown materials, the substrate-induced strain can influence the Néel vector orientation [47] or even the character of exchange coupling significantly. Change of the exchange character appears in materials with other stable magnetic ordering, e.g., magnetic phase transition materials [48, 49, 50]. The effect of strain plays a significant role in studying spatially confined AF structures [51], which could be of interest for AF memories [8]. Electrical readout of AF memory states is possible, utilizing anisotropic magnetoresistance, which depends on the Néel vector direction [14]. Deviations of the Néel vector are therefore critical for successful readout. The higher sensitivity of the AF exchange to crystallographic disorder suggests that anisotropic effects in epitaxially grown layers are much more critical than in FM ordering [52, 53]. Possible scenarios of strain-driven anisotropy in AF are shown in Figure 1.6. In Figure 1.6 **(a)** no strain is induced due to the zero lattice parameter mismatch between the substrate and the thin layer on top. Figure 1.6 **(b)** shows substrate-induced compressive strain forming the EA

for L perpendicular to the direction of lattice elongation [54]. Strained lattice tends to relax the strain upon crystallographic defect formation as in Figure 1.6 **(c)**. The direction of the induced EA may vary depending on the particular AF system .
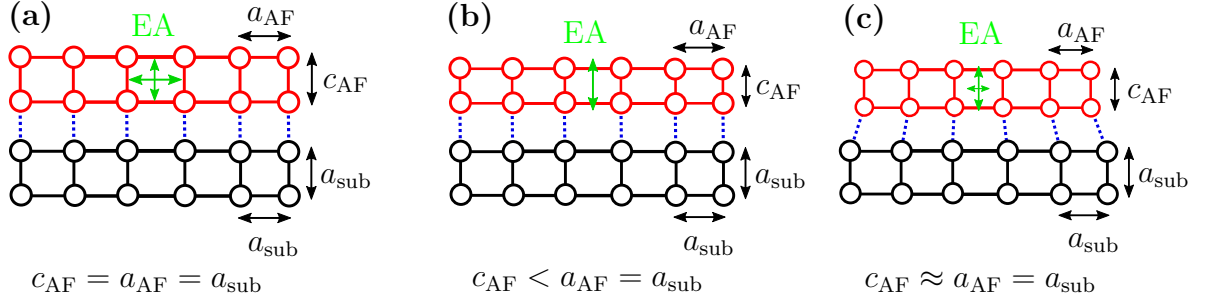

Figure 1.6: Strain controlled direction of L in epitaxial AF. Schemes of the epitaxially grown AF material including indicated lattice parameters showing **(a)** unstrained AF lattice in which the EA are defined purely by bulk lattice properties. **(b)** Strained AF lattice due to lattice mismatch with the substrate implying changes of preferential EA. **(c)** Strain relaxation induced by spatial confinement reducing the EA deviation from **(b)**.

Imaging of AF materials

Imaging techniques of FM materials are primarily based on the interaction with sample magnetization or stray fields. Principles of AF imaging techniques, therefore, have to be chosen differently. Many of them are specific only for a very narrow group of AF materials, based on their lattice symmetry or local uncompensated moments in AF DW [43]. The uncompensated moments can be imaged using conventional techniques like MFM thanks to the stray field formation. Overview of AF imaging techniques can be found in [46]. Several of them are compared in Table 1.2.

Table 1.2: Comparison of AF imaging techniques. Each AF sensitive technique is characterized by the medium used for imaging, effect responsible for the sensitivity to AF, approximate lateral resolution r, typical detection depth d, and sample preparation process required for imaging. All values are considered for the AF signal [11, 46]. Meanings of the abbreviations: Photoemission electron microscopy (PEEM), X-ray magnetic linear dichroism (XMLD), Spin-polarized scanning tunneling microscopy (SP STM), Scanning probe microscopy (SPM), Nitrogen vacancy microscopy (NVM), Light microscopy (LM), Voigt effect (VE).

Technique	Im. medium	Mag. detection effect	r (nm)	d (nm)	Sample prep.
PEEM	X-ray	XMLD	10^1	10^0	Surface cleaning
SP-STM	SPM	SP tunneling	Atomic	1 ML	Ultraclean surf.
NVM	SPM	Zeeman splitting	10^1	-	-
LM	Light	VE	10^2	10^1	-
TEM	Electrons	El. deflection by $\boldsymbol{F}_\mathrm{L}$	Atomic	-	El. transparency

1.5. Metamagnetic phase transition materials

Any substance of fixed chemical composition has multiple material states, so-called phases, which can be stabilized under certain external conditions. All transitions between these phases are considered as phase transitions, and changes of specific material properties manifest them. We can define multiple phase transition types, such as optical, magnetic, superconductive, and many others [55].

We are particularly interested in the magnetic phase transitions, in which significant change of magnetic properties occurs upon the transition. A typical example is the transitions from FM to paramagnet (Curie transition), AF to paramagnet (Néel transition), or so-called *metamagnetic phase transitions* (MPT).

MPT is a type of phase transition accompanied by a significant change of sample magnetization upon applied magnetic field [56, 57]. Such behavior appears in materials undergoing the transition from AF to FM phase due to the stabilization effect of the external field on the FM phase [14]. These materials reflect novel approaches based on which we seek materials combining advantages of both available magnetic orderings, such as fast dynamics of the AF phase and the external control of the FM phase. Several metallic materials undergo MPT from AF to FM, such as CeFeRu, NiMnIn, or FeRh alloys, differentiating mainly in the MPT temperature [58].

The first-order character of AF-FM MPT corresponds to a discontinuous change of the system ordering parameter - magnetization - upon the transition. The first-order transition exhibits a phase coexistence state during the transition [55], at which strong correlation and complex mutual interactions between the phases are expected. This thesis contributes to the development of high-resolution imaging technique for MPT materials.

Experimental investigation of MPT imaging in this thesis is performed on thin layers of the iron-rhodium alloy (FeRh). Equiatomic FeRh undergoes the first order MPT from AF to FM phase upon heating at temperatures close to room temperature ($\sim$ 360 K), making the material a promising candidate for applications with operation temperatures close to room temperature. Besides a well approachable MPT in FeRh, another advantage of the material is the combination of stimuli capable of driving the MPT in FeRh, such as external magnetic field [59], strain [60], or doping [61].

Change of the magnetic properties is accompanied by a lattice volume increase of $(1-2)$ % and a significant reduction in resistivity, as shown in Figure 1.7 **(a)**. Multiple degrees of freedom available in FeRh make this material a test-bed for exploring the interplay of magnetic, electronic, and structural properties [59].

Epitaxial FeRh thin films are usually grown on MgO (001) substrates by magnetron sputtering. Equiatomic FeRh shows CsCl-like, BCC lattice rotated by 45° from the MgO lattice. This configuration induces relatively low lateral compressive strain due to lattice mismatch of -0.17 % in AF phase and -0.05 % in FM phase [50]. Substrate-induced strain deforms FeRh lattice and affects the temperature of MPT by modifying the lattice expansion upon transition [50]. In equiatomic FeRh thin films a minor contribution of the FCC FeRh phase can be found [62]. This metastable FeRh phase does not possess a metamagnetic behavior [63]. Concerning the magnetic properties of the AF phase, antiparallel Fe atomic moments of $m_{\text{Fe}} = 3.3\mu_{\text{B}}$ adopt the G-type AF ordering. In FM phase, parallelly aligned Fe atomic moments of $m_{\text{Fe}} = 3.2\mu_{\text{B}}$ induce the Rh magnetic moment of $m_{\text{Rh}} = 0.9\mu_{\text{B}}$ [64, 65]. The scheme of the FeRh atomic magnetic ordering upon

MPT is depicted in Figure 1.7 **(a)**. Temperature dependence of the magnetic moment of the FeRh thin film, provided in Figure 1.7 **(b)**, exhibits the FeRh MPT. The MPT profile in this thin layer is further confirmed by resistance drop measured in a 1.1 μm-wide FeRh stripe upon heating. According to recent observations, the spatial confinement of the FeRh thin films to the stripes with the width below 500 nm dramatically enhances the sensitivity of the MPT to the magnetic field or temperature upon cooling [52]. This behavior is demonstrated by the temperature evolution of the resistance of a 400-nm-wide nanostripe in Figure 1.7 **(c)**.
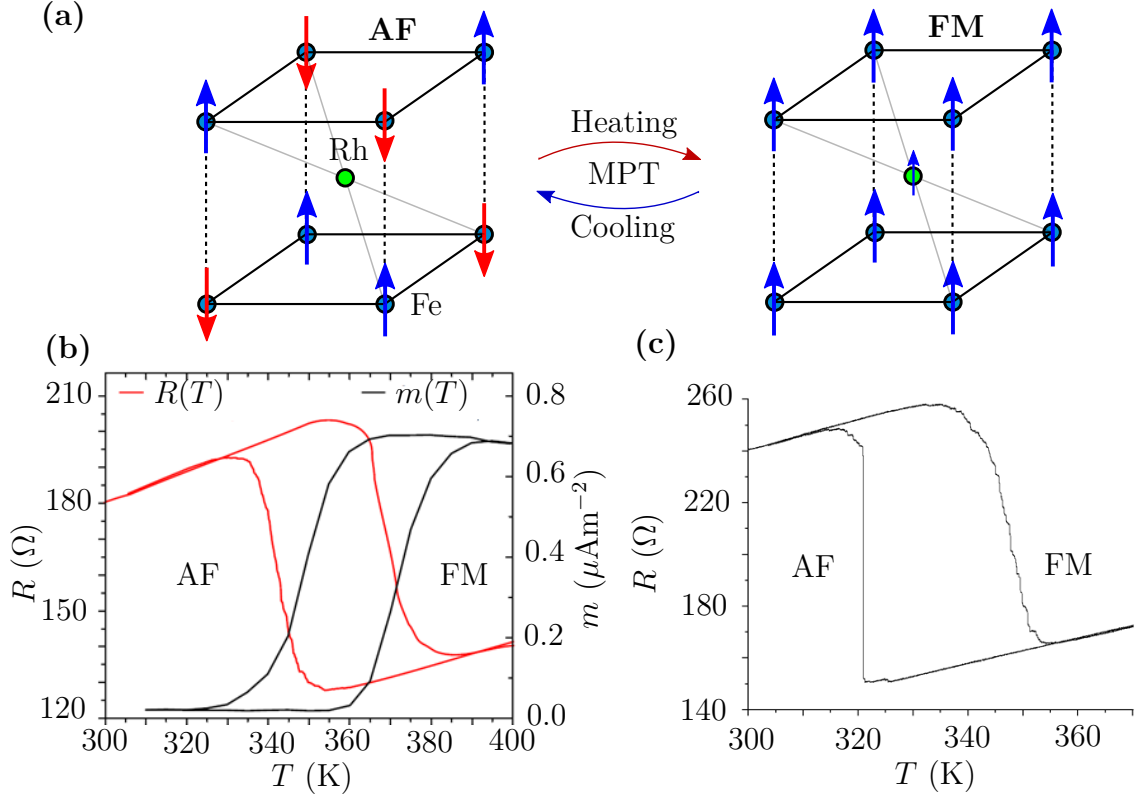

Figure 1.7: Properties of the FeRh MPT. (a) Scheme of the atomic magnetic moment in FeRh upon the MPT. **(b)** Temperature dependence of resistance (red loop) measured in a 1.1-μm-wide stripe along with the temperature dependence of the magnetic moment (black loop) of a corresponding thin film. **(c)** Asymmetrical behavior of resistance in a 400-nm-wide nanowire upon MPT. Adapted from [52].

2. Transmission electron microscopy

The invention of electron microscopy (EM) revolutionized our understanding of materials and their nanoscale properties. After almost 80 years of development, there are two main branches of EM - *scanning electron microscopy* (SEM) and *transmission electron microscopy* (TEM). SEM allows the analysis of bulk samples at nm-resolution; however, state-of-the-art TEMs can reach the atomic resolution, but only with ultrathin electron-transparent samples. Such resolution is essential for today's effort in utilizing nanotechnology. TEM's ability to perform various types of analysis, such as structural, chemical, or even magnetic analysis down to the atomic scale, motivates the use of TEM in this thesis.

This chapter introduces general operating principles and image formation in TEM. Subsequently, we will derive various aspects of TEM magnetic analysis of FM and AF materials in the next chapter. The final part of this chapter is devoted to TEM sample fabrication, which appears to be one of the main difficulties behind TEM.

2.1. Construction and working modes of TEM

Atomic resolution TEM analysis requires a robust, incredibly stable, and precisely aligned setup, divided into three main sections with a characteristic purpose - an *illumination system, objective/stage system*, and *imaging system.*

The illumination part consists of an *electron gun* and *condenser*. This section creates and forms the electron probe in *parallel beam* or in *convergent beam* modes. The electron probe passes through the specimen immersed in the magnetic field of the objective lens. The image embedded in the transmitted electron beam is further magnified with the projector lens and acquired by detectors. Based on the imaging system settings, we define the *imaging mode* and *diffraction mode* of TEM. In the imaging (diffraction) mode, a real image (a diffraction pattern) is transferred onto the detector.

Parallel beam TEM in the imaging mode is also known as *conventional TEM* (CTEM) and in the diffraction mode we talk about the parallel diffraction mode, or *selected area electron diffraction* (SAED). The parallel beam mode often utilizes the objective aperture and SAED aperture, placed in the objective back focal plane (BFP) and the image plane, respectively. The objective aperture cuts the spatial frequencies of the diffraction pattern formed in the objective BFP, allowing us to perform *bright field* (BF) or *dark field* (DF) imaging. The SAED aperture spatially limits the region from which the diffraction pattern is formed.

The convergent mode is practically operated only in the diffraction mode, in which *convergent beam electron diffraction* (CBED) and *scanning TEM* (STEM) imaging can be done. STEM utilizes the signal taken from a spatially localized region for all kinds of spectroscopies available in TEM [66]. The imaging mode with the convergent beam is used mainly for optical alignment of the TEM. The purpose of individual TEM components is briefly described in the following text. Schematic visualization of the whole TEM setup is then shown in Figure 2.1.
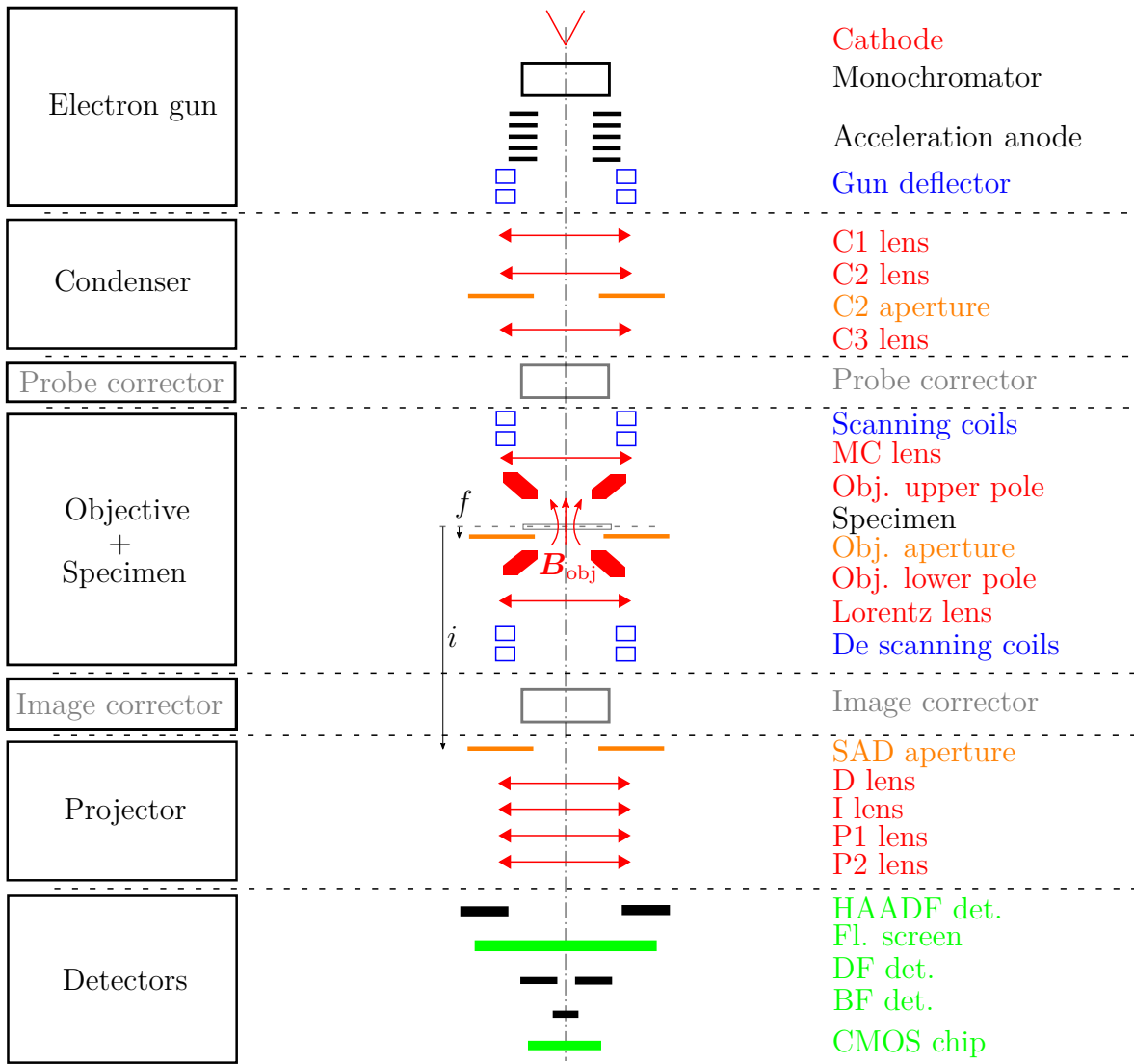
Figure 2.1: TEM setup components. The scheme covers majority of the optical components in TEM discussed in the text. However, the presence of many other components is essential for the full TEM operation, such as electrostatic deflection coils, stigmators for astigmatism correction, valves, blankers, etc. Abberation correctors appear only in top tier setups and their positions are included for completeness [66].

The *Electron source* consists of a high-voltage accelerator, electron gun, and eventually monochromator. An electron beam emitted from the electron gun cathode is accelerated by a high-voltage anode source with very narrow energetical dispersion of fractions of eV. A monochromator can further reduce this dispersion. The beam then continues to the condenser part [66].

The *Condenser part* defines the electron probe character before reaching the specimen. Besides the beam convergence angle, it controls the electron beam current and electron probe diameter. It is conventionally made of 2 or 3 condenser lenses. In probe corrected setups, they are followed by a probe corrector [66].

The *Objective part* includes scanning coils, objective lens, and the specimen itself. These components can be followed by the image corrector of objective-induced optical aberrations. Scanning coils placed before the objective provides scanning in STEM mode. Besides the objective itself, there can be other lenses set in the vicinity of the specimen, such as the *minicondenser* (MC) lens or Lorentz lens. MC lens placed before the objective cooperates with the condenser part on electron probe formation. The objective lens then consists of upper and lower pole pieces, and the specimen is conventionally immersed in a strong objective magnetic field of $(1-2)$ T, which corresponds to the *immersion mode*. The immersion mode of TEM operation plays a significant role in the analysis of magnetic materials. Optionally, we can use the Lorentz lens as an imaging lens instead of the objective, which is placed below the sample plane. Spectroscopy detectors, such as the *Energy dispersive X-ray spectroscopy* (EDX) or *Cathodoluminiscence* (CL) mirror, can be placed in the vicinity of a specimen [66].

The *Projection part* further magnifies the outcoming beam from the specimen, which the objective has already magnified. Nowadays, it usually consists of 4 lenses, which continuously magnify the image from the previous lens. If the object plane of the first lens is set into the objective image plane (back focal plane), we operate in the imaging mode (diffraction mode) [66].

The *Detection part* visualizes the magnified beam and serves for data acquisition. Visualization can be done on a fluorescent screen, which is nowadays recorded by a camera and transferred to the computer. A CCD or CMOS chip can be used for high-quality acquisition, but they are much more sensitive to electron beam damage. In the STEM mode, the signal is acquired directly from the diffraction pattern. Therefore it is beneficial to split this pattern into several annular sections corresponding to individual detector segments. Each of these sections provides different information about the specimen. Annular semiconductor detectors integrating the signal over their whole area are used for this purpose. Starting from the lowest acquisition angle, we use the *bright field* (BF) detector, *dark field* (DF) detector and *high angle annular dark field* (HAADF) detector. We can find additional optics and detectors for *Energy electron loss spectroscopy* (EELS) even below all of these conventional detectors [66].

2.2. Image formation in TEM

TEM setup allows operation in different modes providing multiple types of analysis. Electron-sample interaction, together with the transfer of information from the specimen to the screen via electrons, is non-trivial and is closely related to the wave character of electrons and the electron-sample interaction. The sample modifies the amplitude and phase of the electron wave implying two distinct types of contrasts. Amplitude and phase contrast are then transferred through the whole microscope. Each of these elements contributing to the image formation and information transfer through the TEM setup is described in the following section.

2.2.1. Wave-particle dualism of an electron

Nearly one hundred years ago, in 1924, Louis de Broglie came up with the idea of a relation between the particle momentum p with its wavelength λ as $\lambda = h/p$, where h stands for the Planck constant [67]. This wave-particle dualism has been fully developed in later quantum mechanics. Utilizing wave properties of electrons is essential for the successful realization of electron microscopy. In this section, a basic theory standing behind this dualism is presented.

Particle properties are described mainly by the particle momentum p and energy E. Relativistically corrected quantum theory of an electron introduced in the late '20s of the 20th century characterized by the Klein-Gordon equation [68, 69] and Dirac equation [70] corrects the electron behavior at velocities approaching the speed of light c. Following the derivation from [71], we can define the relativistically corrected electron momentum as

$$p = \sqrt{2em_0U^*}, \tag{2.1}$$

where m_0 stands for the rest mass of an electron, e for elementary charge, and U^* for relativistically corrected acceleration voltage defined as

$$U^* = U\left(1 + \frac{eU}{2m_0c^2}\right). \tag{2.2}$$

The total energy of an electron is then calculated as

$$E = \sqrt{p^2c^2 + m_0^2c^4} = \gamma m_0 c^2, \tag{2.3}$$

where γ is a relativistic correction factor dependent on the electron velocity v defined as

$$\gamma = \left(1 - \frac{v^2}{c^2}\right)^{-1/2}. \tag{2.4}$$

Wave properties of electron arise from quantum theory in general, where wave function ψ takes the form of

$$\psi(\boldsymbol{r}) = A(\boldsymbol{r})e^{i[\boldsymbol{k}\cdot\boldsymbol{r}+\phi(\boldsymbol{r})]}, \tag{2.5}$$

where A stands for the wave function amplitude and the phase consists of the wavevector $\boldsymbol{k}(\boldsymbol{r})$ and phase shift $\phi(\boldsymbol{r})$. The position dependent relativistic wave vector $\boldsymbol{k}(\boldsymbol{r})$ for an electron accelerated to the potential U detected in electric field ($\boldsymbol{E} = -\nabla V$) and magnetic field ($\boldsymbol{B} = \nabla \times \boldsymbol{A}$) is affected by the local electric potential $V(\boldsymbol{r})$ and magnetic potential $\boldsymbol{A}(\boldsymbol{r})$ as

$$\boldsymbol{k}(\boldsymbol{r}) = \frac{\sqrt{2em_0(U^* + V(\boldsymbol{r}))}}{\hbar}\boldsymbol{e}_p - \frac{e}{\hbar}\boldsymbol{A}(\boldsymbol{r}). \tag{2.6}$$

We can define the corresponding electron wavelength λ, defined as $\lambda = 2\pi/|\boldsymbol{k}|$, which in an electric and magnetic potential free region reads

$$\lambda = \frac{h}{[2m_0eU^*]^{1/2}}. \tag{2.7}$$

Besides the electron wavelength, we can define the relativistic electron velocity v, which can be calculated from equation 2.3, where v is hidden in γ, as

$$v = \frac{1}{1 + \dfrac{eU}{m_0 c^2}} \sqrt{\frac{2eU^*}{m}}. \tag{2.8}$$

Considering the typical conditions in TEM, with an acceleration voltage of $U = 300$ kV we get $\lambda = 1.97$ pm and $v = 2.33 \cdot 10^8$ ms^{-1} $= 0.78c$. The ultimate resolution of an aberration-free microscope with an ideal electron source is determined by diffraction effects, expressed by the Rayleigh criterion [72]. Based on that, we get a resolution of 30 pm for the angle of semiconvergence $\alpha = 30$ mrad and the acceleration voltage of at $U = 300$ kV. However, the real resolution of the electron microscope is mainly limited by the aberrations arising from electromagnetic lenses, apertures, and other construction imperfections together with the electron source energy dispersion. Therefore, the best TEMs are equipped with aberration correctors or with electron source monochromators leading to the ultimate resolution close to 50 pm [73, 74, 75].

2.2.2. Electron-sample interaction

Complex electron-sample interaction in TEM varies depending on the sample character. In thin electron-transparent samples, we tend to approximate this interaction by a single scattering process, in which only one scattering event is considered. Generally we distinguish *elastic* and *inelastic* electron-sample interaction. There is no measurable transfer between elastically scattered electrons and the specimen, which is not the case for inelastic scattering. Scattering coherency and the outcoming angle of electrons after scattering represent the others differentiating factors. Coherent scattering is defined by a well-defined phase relationship between scattered electrons. Therefore, coherent interaction is accompanied by interference phenomena [66].

Elastic scattering is linked to the electrostatic interaction of an electron beam with atomic cores and electron clouds in the specimen and usually occurs at the outcoming angles of 1°-10°. Elastic scattering is mostly coherent at low angles and incoherent at large angles, where Rutherford scattering with atomic nuclei dominates. Elastically scattered electrons also generate a diffraction pattern of crystalline samples. Rutherford scattering dominates at large outcoming angles, and it is a dominant source of signal in STEM HAADF images. Its incoherent character protects this signal from all interference phenomena, allowing direct correlation between HAADF atomic signal and actual atomic positions [66].

Energy transfer in *inelastic scattering* results from multiple types of inelastic processes in the sample. Energy transferred from the electron probe to the sample electron clouds might generate X-rays, secondary electrons, or collective excitations such as plasmons or phonons. Multiple spectroscopy techniques have been developed based on these interactions, such as EDX, EELS, or CL. Inelastic scattering occurs at very low angles below 1° and is almost always incoherent [66].

Above mentioned scattering phenomena can be translated into the *amplitude contrast* and *phase contrast* present in acquired images. In other words, all interactions modify the amplitude and phase of the transmitted electron wave. Both of these contrast forms

are always present in real samples. However, we tend to define measurement conditions such that one type of contrast strongly dominates.

2.2.3. Amplitude contrast

Attenuation of the electron wave amplitude occurs with mass-thickness contrast arising from incoherent elastic Rutherford scattering. The differential cross-section of Rutherford scattering $d\sigma_{\mathrm{R}}(\theta)$ was derived in 1911 [76] and follows

$$d\sigma_{\mathrm{R}}(\theta) = \frac{e^4 Z^2}{16(4\pi\epsilon_0 E_0)^2} \frac{d\Omega}{\sin^4(\theta/2)}, \tag{2.9}$$

where Z is an atomic number of the atom that an electron with the energy E_0 is scattered from. This electron is deviated by the angle of $\theta/2$ into the annular spatial angle $d\Omega$. Equation (2.9) reflects strong dependence of Rutherford scattering on Z. The number of scattering events grows with the sample thickness, resulting in sample thickness dependence in amplitude contrast. Amplitude contrast dominates in amorphous samples. In crystalline samples, it competes with Bragg diffraction contrast mainly at the electron outcoming angles below 5°, which is linked to the coherent phase contrast [66].

2.2.4. Phase contrast

Apart from the amplitude change of the electron wave upon scattering, coherent scattering events maintain the relation between the electron wave phases. Outcoming phase-shifted electron waves interfere with non-scattered electron waves, which results in phase contrast. The total phase shift of the outcoming electron wave function $\phi(\boldsymbol{r})$ (introduced in equation (2.5)) consists of

$$\phi(\boldsymbol{r}) = \phi_{\mathrm{str}}(\boldsymbol{r}) + \phi_{\mathrm{el\text{-}mag}}(\boldsymbol{r}), \tag{2.10}$$

where $\phi_{\mathrm{str}}(\boldsymbol{r})$ and $\phi_{\mathrm{el\text{-}mag}}(\boldsymbol{r})$ correspond to the phase shift created by the interaction with periodic structure and by sample internal electric and magnetic field, respectively. Structural analysis of the crystalline samples is well developed and understood technique. Therefore we only present a few aspects of this theory, considering that much broader characterization of physical processes standing behind structural analysis and diffraction can be found in [66] including the associated references. On the other hand, analysis of electromagnetic fields at high spatial resolution is a novel, rapidly evolving area of TEM analysis. Besides the short introduction in this section, the whole chapter 3 is dedicated to that topic.

Structural phase contrast

Structural analysis in TEM is possible due to the subatomic wavelength of the electron probe allowing diffraction on the sample lattice. We assume an incoming planar electron wave, which is scattered by individual atoms of the specimen lattice. Considering the incoming plane wave $\psi = \psi_0 e^{i\boldsymbol{k}\cdot\boldsymbol{r}}$ scattered by a point charge representing the sample atomic nuclei, we get the outcoming spherical wave in the form of [66]

$$\psi_{\mathrm{sc}} = i\psi_0 f(\theta) \frac{e^{ikr}}{r}, \tag{2.11}$$

where $f(\theta)$ corresponds to the atomic scattering amplitude, which is generally a function of the scattering angle θ, electron wavelength λ, and atomic number Z, while e^{ikr}/r represents a spherical wave. If we stack individual atoms into lattice with positions (x_i, y_i, z_i), we can define the so-called *structural factor* $F(\theta)$, characterizing the overall amplitude and phase of the scattered wave, as [66]

$$F(\theta) = \sum_i f_i(\theta) e^{i(hx_i + ky_i + lz_i)}, \tag{2.12}$$

where the sum goes over atoms in one unit cell of the sample lattice and (h, k, l) are Müller indices of atomic planes forming the crystal structure. At certain outcoming angles, we get constructive interference visible in the TEM diffraction mode as diffraction spots. These waves continue to interfere and create HR TEM images to reveal atomic lattice structure. We tend to relate the HRTEM mode closely with phase contrast [66].

Different mutual orientations of the lattice and the electron probe will then provide distinct contrast even at lower magnifications, sometimes referred to as *diffraction contrast*. Besides that, we often deal with manifestations of *dynamical scattering theory* [66], which significantly contributes to the image contrast in the regions with precisely fulfilled diffraction conditions. The electron beam is well aligned with atomic columns corresponding to the lattice *zone axis* (ZA). ZA corresponds to the direction along the intersection of two or more atomic planes[1] in crystalline samples. Dynamical scattering theory deals with multiple scattering events, which is more likely to appear in thick samples or under very precisely defined Bragg diffraction conditions, when an electron beam travels along the ZA of the crystal [66]. An example of such signal is shown in BF TEM micrographs of an MgO substrate lamella in Figure 2.2. Significant changes of the dynamical diffraction signal suggest specimen bending. Intense lines then evolve upon different sample tilts, as shown in Figure 2.2 **(a)** − **(c)**. This signal has to be considered in the data interpretation of crystalline samples.

(a) $\alpha = 0°$ **(b)** $\alpha = 1°$ **(c)** $\alpha = 2°$
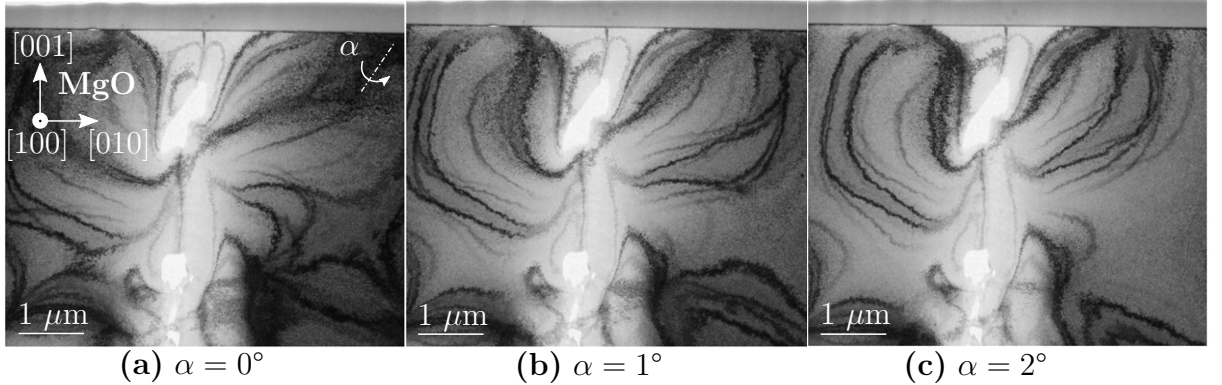
Figure 2.2: Dynamical diffraction effect in MgO lamella. BF TEM micrographs of MgO lamella along [100] ZA showing a significance of dynamical diffraction signal. Sample tilt along indicated direction of **(a)** 0°, **(b)** 1° and **(c)** 2° demonstrate the evolution of diffraction contrast upon specimen tilt.

---

[1]To identify a particular ZA, we use the notation [UVW], which is a direction that is common to all intersecting planes of the ZA.

Electro-magnetic phase contrast

Internal electric and magnetic fields within the specimen with their corresponding potentials contribute to the transmitted electron wave phase through the local changes of electron wavevector introduced in equation (2.6). The total phase shift caused by electric and magnetic fields is achieved by integration of the electromagnetic wavevector deviations over the regions with non-zero electric and magnetic potentials as

$$\phi_{\text{el-mag}}(x,y) = \phi_{\text{el}}(x,y) + \phi_{\text{mag}}(x,y) = \frac{e}{\hbar v}\int V(x,y,z)dl - \frac{e}{\hbar}\int \boldsymbol{A}(x,y,z)\cdot d\boldsymbol{l}, \quad (2.13)$$

where v is an incoming electron velocity in the z-direction, V and $\boldsymbol{A}$ are electric and magnetic potentials and $d\boldsymbol{l}$ is an infinitesimal unit of electron trajectory [71].

A detailed description of the field detection and quantitative evaluation in TEM is further described in chapter 3.

2.2.5. Information transfer through the TEM

Sample-induced modulation of the electron wave leaving the specimen is transferred to the detector to reveal the specimen properties. The formalism of the amplitude and phase information transfer in parallel beam TEM is adopted from the Abbe theory [77, 78], which is conventionally used in the theory of light microscopy.

Besides the parallel illumination mode, image formation and its transfer in the convergent beam mode must be considered. The *reciprocity principle* from light optics justifies adopting most of the theory from parallel mode into the coherently scattered electrons in STEM. Lastly, we will briefly introduce a formalism for incoherently scattered electrons in the HAADF STEM mode.

Reciprocity principle

The reciprocity principle is a general principle in the wave theory, based on which electron ray trajectories can be reversed in time; therefore, we can switch image and source points. We further consider the relationship between coherent a STEM source and coherent imaging in parallel TEM. According to the reciprocity principle, the phase contrast in parallel beam TEM is equivalent to a STEM image recorded with a point detector on the optical axis, which approximately corresponds to the BF STEM imaging mode. Consequently, a great deal of theory and principles of information transfer from the parallel TEM mode is valid in BF STEM. Conical illumination in the convergent beam mode makes the derivation more complicated and requires the superposition of many incident waves with different incidence angles [79]. A rigorous mathematical derivation of this principle for TEM can be found in [80].

CTEM image formation

Transfer of the amplitude and phase information to the detector can be described in terms of Abbe theory of imaging [77], which can be for parallel beam TEM briefly summarized in the following points:

- The incident electron wave formed by the condenser system ψ_{inc} is modulated after passing through the sample. This corresponds to the multiplication by a complex sample transmission function $t(\boldsymbol{r}) = S(\boldsymbol{r})e^{i\phi(\boldsymbol{r})}$ modifying the amplitude and phase of transmitted wave ψ_{t} as $\psi_{\mathrm{t}}(\boldsymbol{r}) = \psi_{\mathrm{inc}}t(\boldsymbol{r})$.
- The transmitted wave is then imaged by the objective lens. The diffraction pattern formed in the BFP of the objective corresponds to the Fourier transform of the transmitted wave $\psi_{\mathrm{t}}(\boldsymbol{k}) = FT\{\psi_{\mathrm{t}}(\boldsymbol{r})\}$.
- Aberrations introduced mostly by the objective lens might be mathematically implemented in terms of an additional phase shift to the diffraction pattern as a complex exponential function $e^{-i\chi(\boldsymbol{k})}$. Note that the aberration function $\chi(\boldsymbol{k})$ is strongly dependent on the spatial frequency $\boldsymbol{k}$.
- The wave function in the image plane $\psi_{\mathrm{i}}(\boldsymbol{r})$ is then an inverse Fourier transform of the aberration modulated diffraction pattern written as $\psi_{\mathrm{i}}(\boldsymbol{r}) = FT^{-1}\{\psi_{\mathrm{t}}(\boldsymbol{k})e^{-i\chi(\boldsymbol{k})}\}$.
- The recorded image $g(\boldsymbol{r})$ is equivalent to the intensity of ψ_{i} as $g(\boldsymbol{r}) = |\psi_{\mathrm{i}}(\boldsymbol{r})|^2$. This can be rewritten as a convolution of the wave transmitted through the specimen with the so called *point spread function* defined as $h_0(\boldsymbol{r}) = FT^{-1}\{e^{-i\chi(\boldsymbol{k})}\}$, which then follows $g(\boldsymbol{r}) = |\psi_{\mathrm{t}}(\boldsymbol{r}) * h_0(\boldsymbol{r})|^2$.

In the case of aberration-free imaging, only amplitude contrast coming from the $S(\boldsymbol{r})$ function can be revealed in the detected intensity. Phase modulation, introduced by the aberration phase shift $e^{-i\chi(\boldsymbol{k})}$, mixes the amplitude and phase contribution and makes even the phase-contrast detectable. Zernike showed in 1935 [81] that the optimal phase shift added in the Fourier space is $\pm\pi/2$, which can be reached by aberrations or by phase plates [82]. As pointed out before, there is a strong dependence of the information transfer on spatial frequency.

The effect of aberrations on the resulting image is covered by the so called *Contrast transfer function* (CTF) defined as $CTF = FT\{h_0(\boldsymbol{r})\}$, which can be further separated into Amplitude CTF (ACTF) and phase CTF (PCTF) defined as $ACTF = \cos\chi(\boldsymbol{k})$ and $PCTF = \sin\chi(\boldsymbol{k})$, respectively. Additionally, effects of electron scattering on the specimen together with gun properties and incoherent aberrations modulate the amplitude of ACTF and PCTF through the so called *envelope function $E(k)$*, which vanishes at large $|\boldsymbol{k}|$. By applying the results of Zernike, the higher PCTF gets, the more pronounced phase contrast becomes for certain spatial frequency. We therefore seek for the largest interval of spatial frequencies in PCTF, which represents unchanged sign of the phase contrast. PCTF is highly dependent on the system defocus, which is an easily adjustable aberration in CTEM through the objective excitation. In 1949 Scherzer derived [83], that the widest range of visible spatial frequencies is reached for the so called *Scherzer defocus* $\Delta f_{\mathrm{Scherzer}}$, which can be calculated as

$$\Delta f_{\mathrm{Scherzer}} = -1.2\sqrt{C_{\mathrm{s}}\lambda}, \tag{2.14}$$

where C_{s} is a spherical aberration coefficient and λ is an electron wavelength. In the case of the aberration-corrected microscope, we can correct aberrations up to the 3rd order. Aberration correction pushes the information limit such that it is now determined mainly by the chromatic aberration, however, the phase contrast gets much weaker [71].

Based on the reciprocity principle, the BF STEM mode forms equivalent phase contrast as CTEM, and we can adopt the derived PCTF properties for phase contrast in BF STEM. [84]. Despite that, we briefly cover the image formation formalism also for STEM mode.

STEM image formation

In the STEM mode, we have to consider the convergent probe character and operation in the diffraction mode. The convergent probe can be viewed as a superposition of plane waves with different wavevectors $\boldsymbol{k}$ with a maximum value of $k_{\max}$. The condenser system determines the convergence angle α represented by $\alpha = \lambda k_{\max}$, where $k_{\max}$ is the maximal spatial frequency transferred by the apertures. The probe function is then expressed as [84]

$$\psi_{\mathrm{p}}(\boldsymbol{r}) = A_{\mathrm{p}} \int_0^{k_{\max}} exp[-i(\chi(\boldsymbol{k}) + \boldsymbol{k} \cdot \boldsymbol{x})]d^2\boldsymbol{k}, \tag{2.15}$$

where $\chi(\boldsymbol{k})$ is an aberration function introduced by the objective lens and A_{p} is a normalizing constant. After passing the beam through the sample we get $\psi_{\mathrm{t}}(\boldsymbol{r}) = t(\boldsymbol{r})\psi_{\mathrm{p}}(\boldsymbol{r})$. The diffraction plane is transferred by projector system to the detector, where we detect

$$g(\boldsymbol{k}) = |\psi_{\mathrm{t}}(\boldsymbol{k})|^2 = |FT\{t(\boldsymbol{r})\psi_{\mathrm{p}}(\boldsymbol{r})\}|^2. \tag{2.16}$$

Based on the detector geometry, we usually do not detect $g(\boldsymbol{k})$ directly. Instead, we detect integrated signal over particular detector segment geometry as

$$g_{\det} = \int_{\det} g(\boldsymbol{k})d\boldsymbol{k}, \tag{2.17}$$

which is then pixel by pixel plotted on the screen. The STEM detector geometry conventionally corresponds to an annular shape, collecting a specific spatial frequency range determined by the TEM optics. In BF STEM with dominant coherent imaging, we get equivalent CTF as in the CTEM mode due to the reciprocity principle. A simplified STEM scheme showing the electron probe profile, overlapping diffraction discs and detector geometry is shown in 2.3 (a).
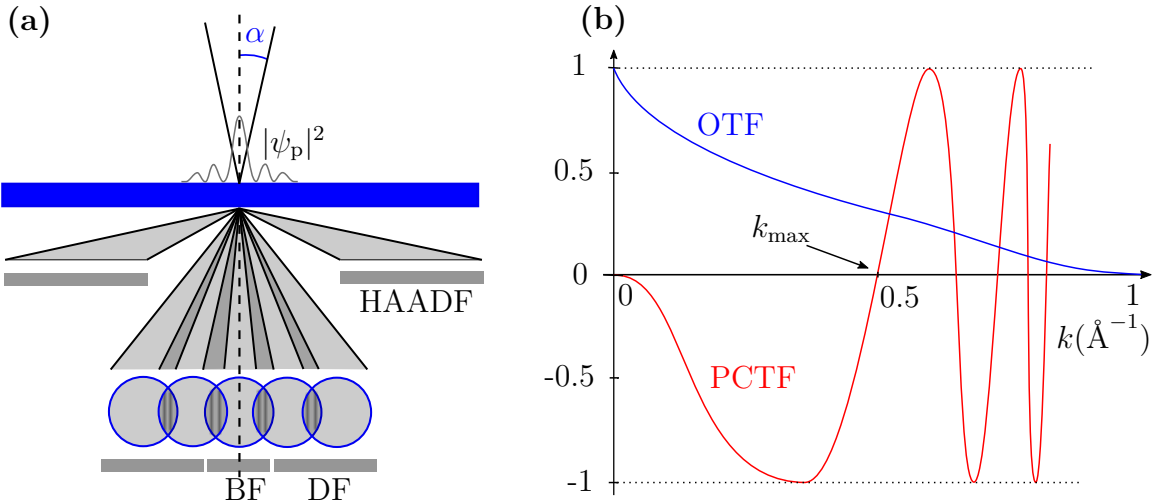
Figure 2.3: Image formation in STEM. (a) Scheme of the STEM geometry showing the convergent probe, overlapping diffraction discs and detector geometry. **(b)** Comparison of PCTF for coherent imaging with OTF for incoherent scattering. PCTF characterizes phase contrast transfer in CTEM and BF STEM and OTF is applied in STEM HAADF mode. Adapted from [86].

Non-coherently scattered electrons dominate in the HAADF mode, where electrons undergo Rutherford scattering. No coherent scattering effects and phase shift phenomena have to be considered, which results in non-oscillatory transfer function [85]. By analogy with light optics [77], this function is referred to as the *optical transfer function* (OTF) for incoherent imaging. Consequently, OTF of the HAADF mode, denoted by H_{HAADF}, corresponds to the Fourier transform of the electron probe intensity as [86]

$$H_{\text{HAADF}} = FT\left\{|\psi_{\text{p}}(\boldsymbol{r})|^2\right\},\tag{2.18}$$

which has a non-oscillatory decreasing character with the cut-off frequency close to $2k_{\text{max}}$, where k_{max} is the maximum spatial frequency passed by the apertures. Based on that, the HAADF mode is often used for ultimate resolution STEM imaging [86].

Comparison of the CTF (valid for the CTEM and BF STEM modes) representing coherent imaging with OTF (valid for the HAADF STEM mode) for incoherent scattering for the same defocus and spherical aberration coefficient is shown in Figure 2.3 **(b)**.

2.3. Sample fabrication for TEM

One of the main requirements for the TEM analysis is the electron transparency of TEM samples. Such a condition nearly always requires the change of initial sample geometry. The sample has to fit into the TEM sample holder allowing discs with 3 mm in diameter and 0.5 mm in height. There is a multitude of possible ways to reach electron transparency. Here we will limit ourselves to techniques used in material sciences suitable for the analysis of thin films. We introduce lamella fabrication using *focused ion beam* (FIB), free-standing samples on a TEM grid, thin films on a TEM membrane, and samples on a TEM grid.

2.3.1. Lamella fabrication

Dual-beam systems combining Ga ion FIB with SEM represent a widely used and versatile toolset, which can be used even for TEM specimen fabrication of so-called lamellae. These thin electron transparent plates of studied material became the most widely used TEM sample geometry for material science. The fabrication process is presented step by step in Figure 2.4 **(a)-(f)**. The first step corresponds to the deposition of the capping layer using the *gas injection system* (GIS) to limit ion irradiation of the desired sample region. We cut out an approximately 1 μm thick plate, which is lifted out using a nanomanipulator and attached to the Cu TEM lamella grid using GIS. Lamella attachment to the grid can be realized in two ways as in 2.4 **(g)**. The Cu TEM lamella grid is shown in 2.4 **(h)**. The last step corresponds to polishing the specimen using FIB to reach electron transparency, usually about or below 100 nm in thickness. Sample irradiation by an ion beam represents the most critical disadvantage of lamella fabrication, especially for ion irradiation sensitive samples [53, 87].

2.3.2. TEM grids and membranes

Thin films grown on a substrate can be imaged in the planar and cross-section view. Planar analysis of thin films in TEM can be performed on a free-standing thin layer
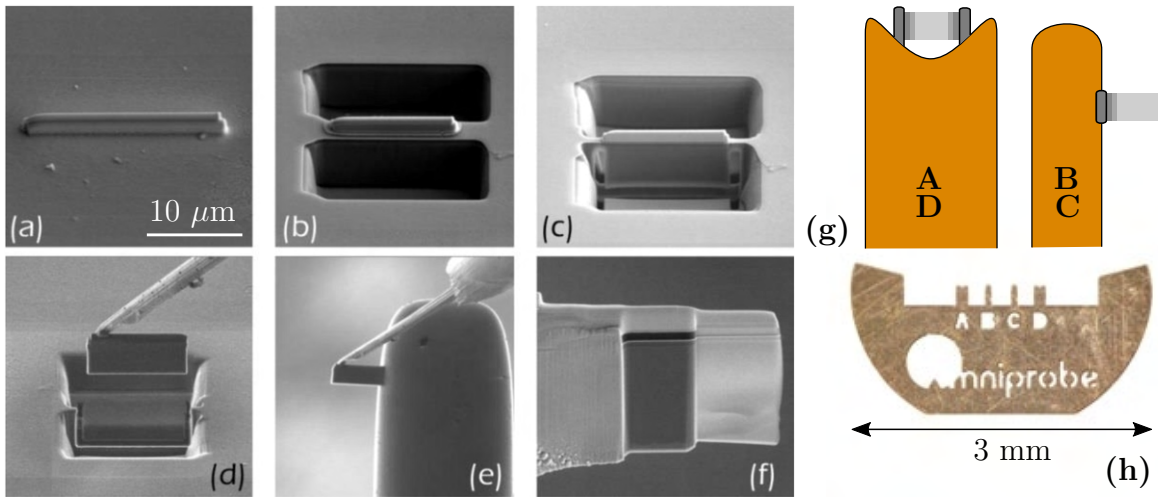
Figure 2.4: Lamella fabrication process. Step by step process of lamella creation. **(a)** GIS deposition of the capping layer on a thin film, followed by FIB milling shown in **(b)** and **(c)**. **(d)** Unpolished lamella attached to the nanomanipulator via GIS is lifted from the substrate and **(e)** welded to the Cu TEM grid. **(f)** Final ion beam polishing is done to reach electron transparency. Adapted from [88]. **(g)** Two main strategies of lamella attachment to the Cu TEM lamella grid, with a typical geometry shown in **(h)**. Adapted from [89].

detached from the substrate. Non-epitaxially grown thin films might be deposited directly on an electron transparent membrane.

The detachment of the thin layer can be done by chemical etching of the substrate, and the film is then transferred onto the TEM grid [90]. The TEM grid geometry is in Figure 2.5. The grid is made of a solid frame, covered by electron transparent carbon with a thin layer of Formvar in between as shown in 2.5 **(a)**. The resulting carbon net inside frame windows, indicated in 2.5 **(b)**, supports electron transparent studied objects placed on top. Carbon net properties vary with particular grid types, and examples of holey and lacey carbon layers are presented in Figure 2.5 **(c)** and **(d)**. Chemically detached epitaxially grown thin films from the substrate should be stress-free; otherwise, curling-up after lift-off will make them practically unusable for the observations [91].

A complementary approach usable mostly for non-epitaxial thin layers is the deposition directly on electron transparent membranes. Thin-film properties can be then studied without any further sample modification. Combined with lithography, even nanostructures can be probed in TEM. Figure 2.5 **(e)** shows the profile of TEM membrane, with corresponding SEM micrograph in Figure 2.5 **(f)**. A supportive thin layer is conventionally made of an amorphous 30 - 60 nm thick layer of Si_3N_4, which prohibits epitaxial growth on top.
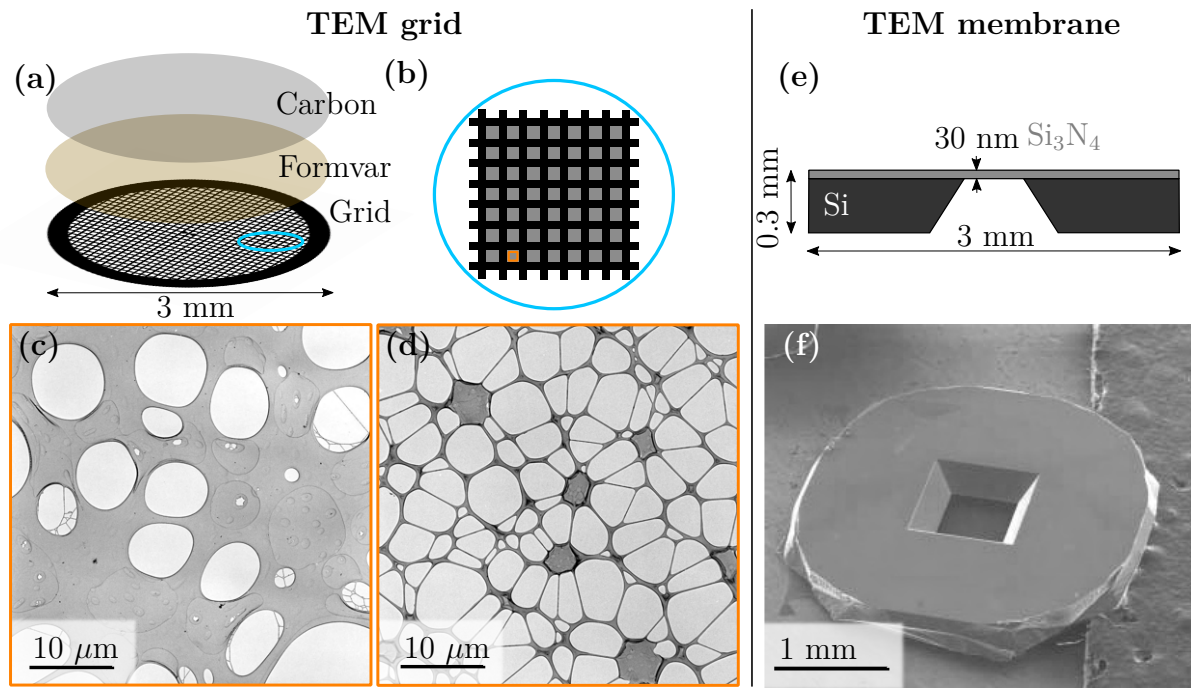
Figure 2.5: TEM grid and membrane geometry. **(a)** Layout of a TEM grid consisting of the frame, Formvar layer and carbon supportive layer. **(b)** Scheme of the electron transparent window with a detailed image showing the structure of **(c)** holey [92] and **(d)** lacey [93] carbon films. **(e)** TEM membrane geometry showing an Si frame covered by a thin layer of Si_3N_4. **(f)** SEM image providing the top view on a TEM optimized membrane [94].

3. Electric and magnetic field imaging in TEM

The previous chapter described the TEM image formation and the information embedded in individual TEM imaging modes. Analysis of magnetic properties of materials requires a few more aspects to be added. The magnetic field of the specimen interacts with the electrons in a TEM probe similarly to electric fields through the Lorentz force. Therefore, we cover electric and magnetic field properties in TEM specimens and the detection to extract these two signals.

After a general introduction of electric and magnetic field distribution in solids, we further develop the relation between phase contrast formalism and electric and magnetic fields mentioned in section 2.2.4. Consequently, we introduce magnetism-sensitive techniques, focusing on *differential phase contrast* (DPC), which will also be used for experiments. Since DPC is operated in the STEM mode, we go through imaging aspects of STEM in further detail to understand the field distribution we observe in the sample. The final part briefly covers state of the art in TEM imaging of AF materials and materials undergoing MPT, particularly FeRh.

3.1. Electric and magnetic fields in matter

Electron deflection can be caused both by electric and magnetic fields. We assume field distribution $\boldsymbol{E}(\boldsymbol{r}_\perp, z)$ and $\boldsymbol{B}(\boldsymbol{r}_\perp, z)$ across the thin TEM sample of thickness d. Overall deflection of electrons is caused by the field distribution across the whole specimen thickness. Therefore it is beneficial to define averaged fields over the sample thickness as [95, 96]

$$\overline{\boldsymbol{E}}(\boldsymbol{r}_\perp) = \frac{1}{d} \int_0^d \boldsymbol{E}(\boldsymbol{r}_\perp, z) dz, \tag{3.1}$$

$$\overline{\boldsymbol{B}}(\boldsymbol{r}_\perp) = \frac{1}{d} \int_0^d \boldsymbol{B}(\boldsymbol{r}_\perp, z) dz. \tag{3.2}$$

Origin of these internal specimen fields $\boldsymbol{E}(\boldsymbol{r}_\perp, z)$ and $\boldsymbol{B}(\boldsymbol{r}_\perp, z)$ are described in the following section.

3.1.1. Electric field origin

Starting from the atomic scale, each atomic nucleus induces a radial electric field with an amplitude linearly dependent on the atomic number Z, decreasing with the radial distance from the nucleus. Electrons orbiting around the nucleus are negatively charged, and their overall contribution to the total electric field can be described in terms of electron cloud shielding [97], which effectively lowers the nuclear field. Interatomic bonds further modify the electron density in the atomic core vicinity, thus contribute to the electric field distribution. Quantitative modeling of electric field distribution must be performed through *density functional theory* (DFT) calculations [95, 96]. Typical values of the electric field in the vicinity of the atomic nucleus are in the order of $10^0 - 10^1$ V/pm [98, 95].

In crystalline materials, the lattice unit cell can be defined [18]. In materials with no macroscopic electric polarization, we expect that averaging the fields over the unit cell should lead to exact cancellation of the electric field from atomic columns at a larger scale [96, 99]. Macroscopically, we can only define average electrostatic potential over the unit cell, the so-called *mean inner potential* (MIP) V_{MIP} as [100]

$$V_{\text{MIP}} = \frac{1}{\Omega} \int_{\Omega} \phi(x, y) dV, \tag{3.3}$$

where Ω is the area of the projected unit cell and $\phi(x, y)$ is the internal sample potential arising mainly from the atomic cores. Macroscopically, MIP is a constant value across the sample volume, causing a constant phase shift of the transmitted electron wave based on equation (2.13).

Non-zero macroscopic electric fields in the specimen can be found in many different samples, such as in semiconductors [101] or in strained sample regions [102]. Such field distribution can be effectively studied using TEM electro-magnetic field-sensitive techniques mentioned later in this chapter.

3.1.2. Magnetic field origin

Magnetic properties of the material originate from atomic moments $\boldsymbol{m}$ as described in the magnetism introductory section 1.1. Each moment can be seen as a source of its own local magnetic $\boldsymbol{B}$-field distribution. Quantitatively, this field distribution can only be described in terms of DFT simulations [96]. Solid-state properties then determine magnetic ordering; hence macroscopic magnetic field distribution [18].

FM-aligned magnetic moments result in a non-zero magnetic field corresponding to the sample magnetization. Dipolar interaction then contributes through the demagnetizing field and stray field. The stray field is the only magnetic field component outside of the FM body, as described in section 1.2.

On the other hand, no macroscopic magnetization and stray fields are formed in AF due to its antiparallel exchange interaction. The only detectable magnetic signal can come from the atomic scale magnetic field.

3.2. Electric and magnetic field induced TEM phase contrast formalism

It was shown in chapter 2 that an electron wave passing through the region with non-zero electric potential V and magnetic potential $\boldsymbol{A}$ is phase shifted by $\phi_{\text{el-mag}}$, as defined in equation (2.13). The spatially evolving electron beam phase shift results in the beam deflection angle $\beta_{\text{el-mag}}$ as

$$\beta_{\text{el-mag}} = \frac{\lambda}{2\pi} \frac{d\phi_{\text{el-mag}}}{dx}. \tag{3.4}$$

This situation is illustrated in Figure 3.1, where situation **(a)** shows no phase shift of the electron wave, **(b)** a constant phase shift of the specimen and finally **(c)** linearly growing phase shift resulting in the beam deflection β.
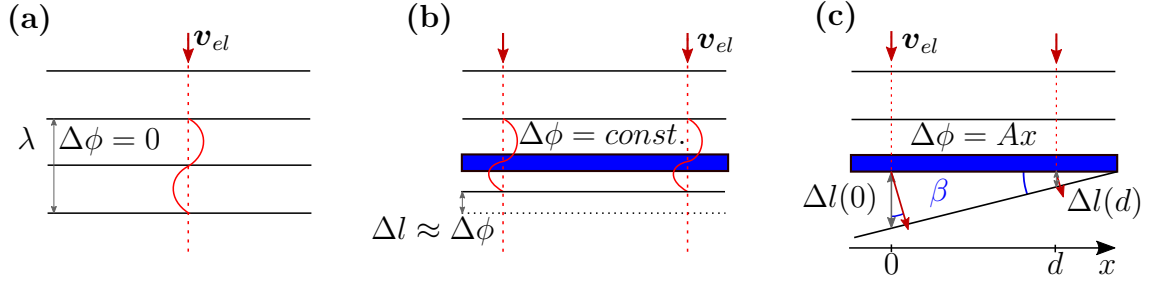
Figure 3.1: Phase shifts of electron wave and beam deflection. (a) Electron wave with indicated wavefronts without a sample. **(b)** Constant phase shift $\Delta\phi$ induced by the sample shifting the wavefronts by a distance Δl. **(c)** Deflection of the electron wave by the β angle induced by a linearly growing phase shift $\Delta\phi(x)$.

In the language of the Lorentz force, the electron deflection is caused only by components of $\boldsymbol{E}$ and $\boldsymbol{B}$ perpendicular to the electron velocity. By combining equations (2.13) and (3.4) and considering the IP sample internal fields $\boldsymbol{E}_{\mathrm{IP}}$ and $\boldsymbol{B}_{\mathrm{IP}}$ across the TEM sample of thickness t, we get deflection angles

$$\beta_{\mathrm{el}}(x,y) = -\frac{e\lambda}{hv}\int_t \boldsymbol{E}_{\mathrm{IP}}(x,y,z)dz, \tag{3.5}$$

$$\beta_{\mathrm{mag}}(x,y) = \frac{e\lambda}{h}\int_t \boldsymbol{B}_{\mathrm{IP}}(x,y,z)dz. \tag{3.6}$$

The above mentioned behavior implies that only the electron beam deflection angle or direct phase-shift mapping can visualize electric and magnetic fields in the specimen. The principles of field-sensitive techniques are described in the following section.

3.3. Field sensitive techniques in TEM

Several TEM techniques have been developed to reveal electric and magnetic field signal distribution in the specimen. An essential factor for magnetic imaging is an immersive character of modern objective lenses, which is described in the following section. We continue by describing magnetism-sensitive techniques, such as the Lorentz TEM, electron holography, and electron magnetic circular dichroism, but with the main focus devoted to differential phase contrast imaging.

3.3.1. Magnetic field-free imaging

Immersive objective lenses in modern TEMs produces magnetic field along the TEM optical axis reaching up to 2 T. In most FM TEM samples, this field is sufficient to saturate sample magnetization in out of plane direction to the sample plane. Since the electron beam deflection is induced only by the in-plane magnetic component of the sample internal magnetic field, no magnetic signal would be detected [103]. By switching off the objective lens, we eliminate the immersive magnetic field allowing the FM signal observation; however, TEM magnification is reduced significantly. This operation mode is known as *field-free* TEM. Magnification of the objective lens can be partially substituted by the so-called Lorentz lens, placed below the specimen plane, which produces magnetic

field that does not affect the specimen. The objective magnetic field might also be utilized as an external OOP magnetic field source within TEM. The objective lens magnetic field represents a significant issue prohibiting atomic resolution of magnetic imaging in TEM. Novel objective lens geometries can overcome this limitation [104].

On the contrary to FM, exchange interaction in AF maintains antiparallel ordering even in the presence of the large objective field. AF anisotropy and AF susceptibility determines the Néel vector direction as explained in section 1.4. The atomic magnetic signal of AF can be potentially resolved in the objective-on mode, opening a new era of high-resolution magnetic imaging in TEM.

3.3.2. Differential phase contrast

Differential phase contrast (DPC) is STEM technique based on the detection of the CBED pattern intensity deflection. This deflection comes from the sample internal electric or magnetic fields. The deflection angle is measured through the *segmented annular detector* [12] or *pixelated detectors* [105].

Pixelated detectors detect the whole diffraction pattern for each point on the specimen and calculate misplacement of the so-called *center of mass* (COM) of the diffraction pattern. If we consider the diffraction pattern with the intensity distribution $I(\boldsymbol{k})$, we define the COM position $\boldsymbol{k}_{\mathrm{COM}}$ as

$$\boldsymbol{k}_{\mathrm{COM}} = \int \boldsymbol{k} I(\boldsymbol{k}) d\boldsymbol{k}. \tag{3.7}$$

Considering the radially symmetrical diffraction pattern, we can calculate the deflection angle β as $\beta = \lambda|\boldsymbol{k}_{COM}|$. These detectors provide high-speed data acquisition. Since we acquire a 2D pattern for each scanned point on the 2D sample surface, this technique is known as 4D STEM [105, 106].

Segmented annular detectors represent split a STEM annular detector split into 4 or 8 segments. Based on the comparison of signals from the opposite segments, we can estimate the deflection angle of the beam in two perpendicular orientations to get directional information about the beam deflection. The most basic model assumes uniform intensity of the zero-order diffraction disc. This central disc is expanded over the segmented detector by the TEM projector section. Importantly, we are technically looking at the BF signal providing phase-contrast analogous to the CTEM described in section 2.2.5. We can therefore expect a large effect of diffraction contrast in DPC.

For large scale field imaging we assume constant deflection of the electron trajectory by the Lorentz force without CBED pattern intensity redistribution [107]. Considering all these approximations, using a 4-segmented detector in the conventional DPC geometry shown in Figure 3.2 **(a)** and **(b)**, we can define electron beam deflection β in two directions as

$$\beta_{\mathrm{AC}} = \alpha \frac{\sqrt{2}\pi}{4} \frac{A - C}{A + B + C + D}, \tag{3.8}$$

$$\beta_{\mathrm{BD}} = \alpha \frac{\sqrt{2}\pi}{4} \frac{B - D}{A + B + C + D}, \tag{3.9}$$

where α is the angle corresponding to the maximum spatial frequency of the non-deflected direct beam and $A, B, C,$ and D are the signals measured on the individual detector segments [12].
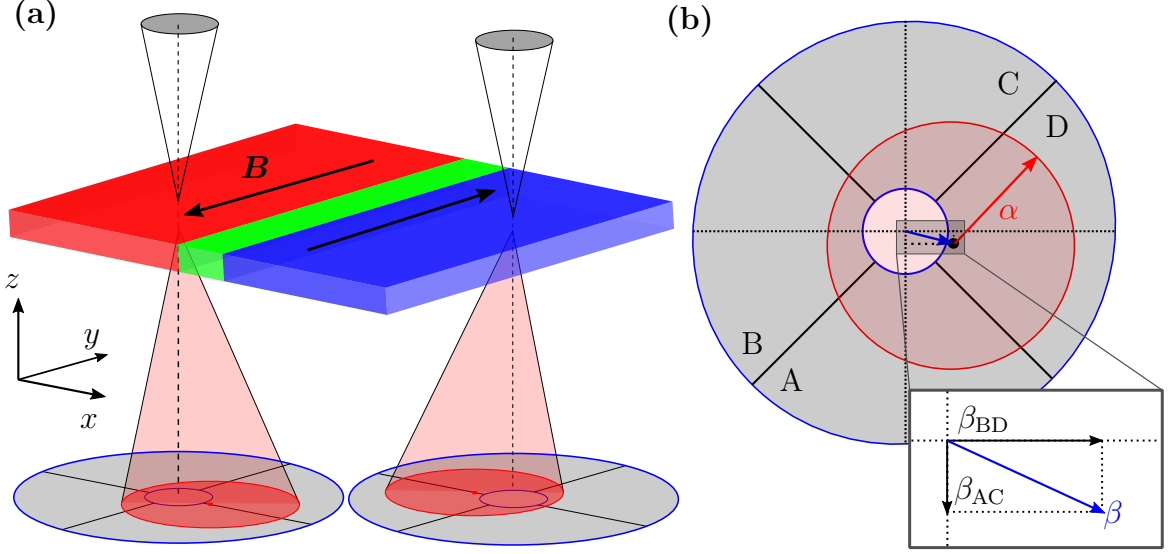

Figure 3.2: DPC experimental setup. **(a)** Scheme of the DPC experiment with the $\boldsymbol{B}$-field indicated in the specimen. **(b)** Segmented detector geometry with the inset showing individual components of the beam deflection.

The quantitative approach from equations (3.8) and (3.9) represent only a basic approximative field evaluation without the assumption of diffraction pattern modulation appearing at high resolution or in crystalline samples [107].

High resolution field evaluation in DPC requires a more sophisticated evaluation process. Under the assumption of an ultrathin sample of units of nm [95], we can approximate the electron beam profile intensity on the specimen as $I(\boldsymbol{r}_\perp, z) \approx I(\boldsymbol{r}_\perp, 0) = I(\boldsymbol{r}_\perp)$, where z goes across the sample thickness. The fields detected $\overline{\boldsymbol{E}}_{\mathrm{det}}(\boldsymbol{r}_\perp), \overline{\boldsymbol{B}}_{\mathrm{det}}(\boldsymbol{r}_\perp)$ using DPC correspond to the convolution of the averaged fields $\overline{\boldsymbol{E}}(\boldsymbol{r}_\perp), \overline{\boldsymbol{B}}(\boldsymbol{r}_\perp)$ with the electron probe intensity $I(\boldsymbol{r}_\perp)$ as [95, 96]

$$\overline{\boldsymbol{E}}_{\mathrm{det}}(\boldsymbol{R}) = \int \overline{\boldsymbol{E}}(\boldsymbol{r}_\perp) I(\boldsymbol{r}_\perp - \boldsymbol{R}) d^2 \boldsymbol{r}_\perp, \tag{3.10}$$

$$\overline{\boldsymbol{B}}_{\mathrm{det}}(\boldsymbol{R}) = \int \overline{\boldsymbol{B}}(\boldsymbol{r}_\perp) I(\boldsymbol{r}_\perp - \boldsymbol{R}) d^2 \boldsymbol{r}_\perp. \tag{3.11}$$

where $\boldsymbol{R}$ represents the electron beam position on the specimen. However, the effect of electron probe profile on the detection quality is considerable only at atomic-scale imaging since the profile beam intensity width is in the order of 10^1 pm for a 300 keV electron probe. The expectation value of the electron momentum deflection $\Delta \langle \boldsymbol{P}_\perp \rangle$ after passing through the specimen can be then expressed as [96]

$$\Delta \langle \boldsymbol{P}_\perp \rangle = -\frac{ed}{v} \left[\overline{E}_{\mathrm{det}} + v \left(-\overline{B}_{\mathrm{det},y}, \overline{B}_{\mathrm{det},x} \right) \right], \tag{3.12}$$

which essentially corresponds to the quantum mechanical treatment of the Lorentz force effect caused by $\overline{\boldsymbol{E}}_{\mathrm{det}}$ and $\overline{\boldsymbol{B}}_{\mathrm{det}}$.

In 2019, Edström et al. [96] published a DFT simulation of internal magnetic fields within the unit cell of FM FePt. The results are summarized in Figure 3.3. Figure 3.3 **(a)** compares simulated DPC signals considering both electric and magnetic fields with a pure magnetic signal. They were simulated for 2.7 nm thick FePt layer at 300 kV. The radial color wheel indicates the direction of the Lorentz force vectors depicted in Figures 3.3 **(a)** and **(b)**. The images clearly show the dominant deflection effect caused by atomic electric fields, which can be up to 10^3 times stronger than magnetic field-induced deflection. Magnetic field simulations are then shown in 3.3 **(b)**, where we can see Lorentz force distribution within the unit cell. In 3.3 **(c)** x- and y-components of magnetic field are presented with and without 300 kV beam profile blurring. By introducing the blurring effect of a 300 kV beam, the field amplitude drops at least by a factor of 3, demonstrating the importance of the beam profile evaluation for atomic resolution mapping.
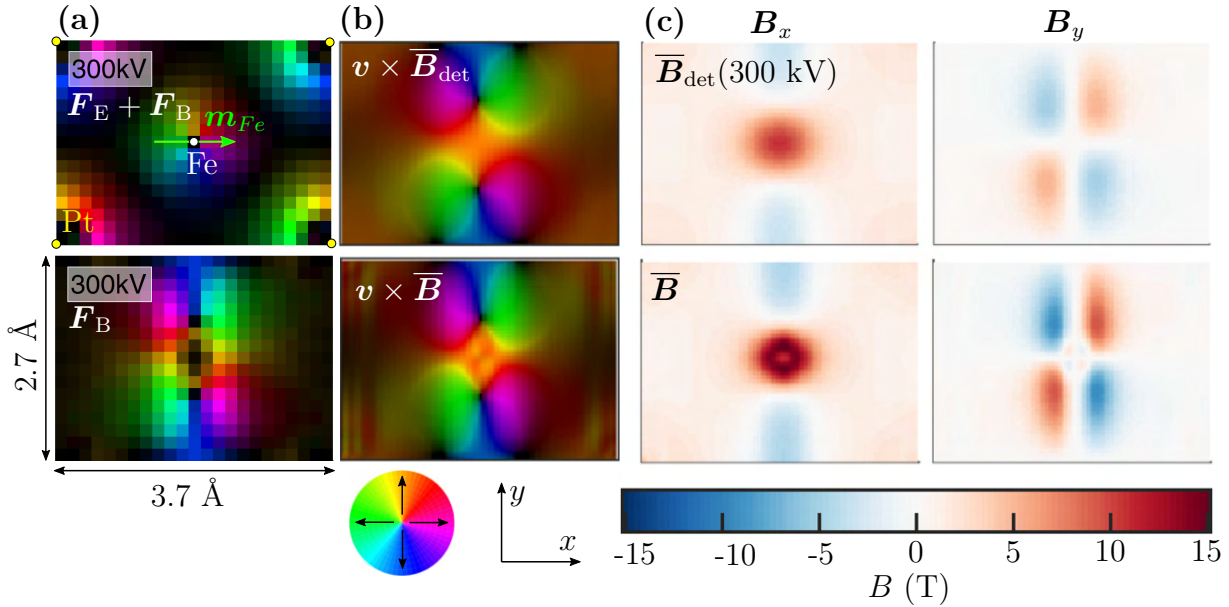
Figure 3.3: DPC simulations of the $\boldsymbol{B}$-field within an FePt unit cell. (a) DPC signal simulated for a 2.7 nm thick layer of FePt at 300 kV showing the dominating electric component in the beam deflection. **(b)** Magnetic field induced Lorentz force distribution coming from the simulated magnetic field distributions, with components plotted in **(c)**. Simulated $\overline{\boldsymbol{B}}$-field averaged over the FePt unit cell together with $\overline{\boldsymbol{B}}_{\mathrm{det}}$ show blurring effect of a 300 kV beam profile. The radial color-wheel indicates the direction of the visualized Lorentz force vector. Adapted from [96].

3.3.3. Other TEM field sensitive techniques

Most of the TEM magnetism-sensitive techniques are based on magnetic phase contrast detection. We briefly cover the most traditional ones, such as the Lorentz TEM and electron holography. The term Lorentz microscopy is sometimes used as an umbrella term for magnetism-sensitive techniques in TEM. However, here it stands for Fresnel and Foucault imaging. Lastly, we will briefly introduce a magnetism-sensitive approach based on electron dichroism. This EELS-based technique provides results similar to the X-ray magnetic dichroism mapping used with polarized X-ray sources [108].

Lorentz TEM

Lorentz TEM (LTEM) refers to the CTEM techniques visualizing the magnetic signal of the specimen, allowing a much faster acquisition rate than DPC. There are two distinct strategies of magnetic field visualization, *Fresnel imaging* and *Foucault imaging*. Although these two techniques can reveal similar information, the origin of the signal detected is entirely different. Generally, these techniques are used only for qualitative field imaging at μm scale, usually for FM domain walls mapping [109]. Principles of both of these techniques are illustrated in Figure 3.4.

The *Fresnel mode* is based on visualizing phase contrast by image defocusing, which in the weak phase object approximation of aberration-free TEM imaging is not distinguishable [66]. Defocus required for clear visualization is in the order of hundreds of μm, reducing the resolution significantly. The resolution is further compromised by the objective field-free operation mode required for FM imaging. In this mode, we are sensitive only to spatial derivatives of electric and magnetic fields equivalent to the second derivatives of magnetic phase contrast [103].

The *Foucault mode* utilizes the objective aperture to specify the angular range of diffracted beams allowing the selection of the electrons deviated only by one direction of the specimen magnetic field. Uneven distribution of electrons in the image leads to contrast between the opposite magnetic domains [103]. The spherical shape of the objective aperture limits the signal significantly, which results in very noisy signal.
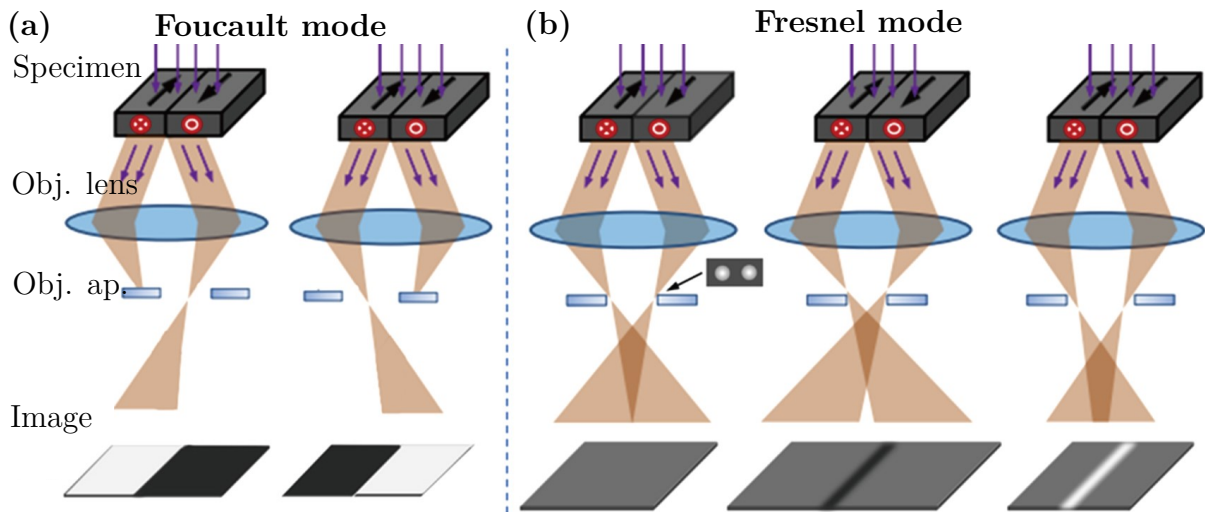
Figure 3.4: Lorentz TEM imaging. Schematic visualization of the magnetic contrast formation in **(a)** Foucault LTEM mode and **(b)** Fresnel LTEM mode. Adapted from [110].

Electron holography

Electron holography (EH) in TEM adopts the principle of the off-axis holography in light microscopy [111]. Optical biprism is replaced by the electrically biased fiber deflecting the electrons and causing interference between the reference incident wave (reference wave) and the wave modulated by the specimen (object wave) as illustrated in Figure 3.5. Both the amplitude and phase modulation of the specimen wave are implemented within the

interference pattern, and they can be extracted by Fourier analysis. Phase shift distribution then allows the reconstruction of the electromagnetic field distribution through the equations (3.4) - (3.6). The separation of electric and magnetic contributions is then the key step for successful data interpretation. Besides the ability of quantitative field mapping, EH is also sensitive to the detection of MIP [100], which is not possible using other mentioned techniques. More EH-related details can be found in the study by Lichte [71].
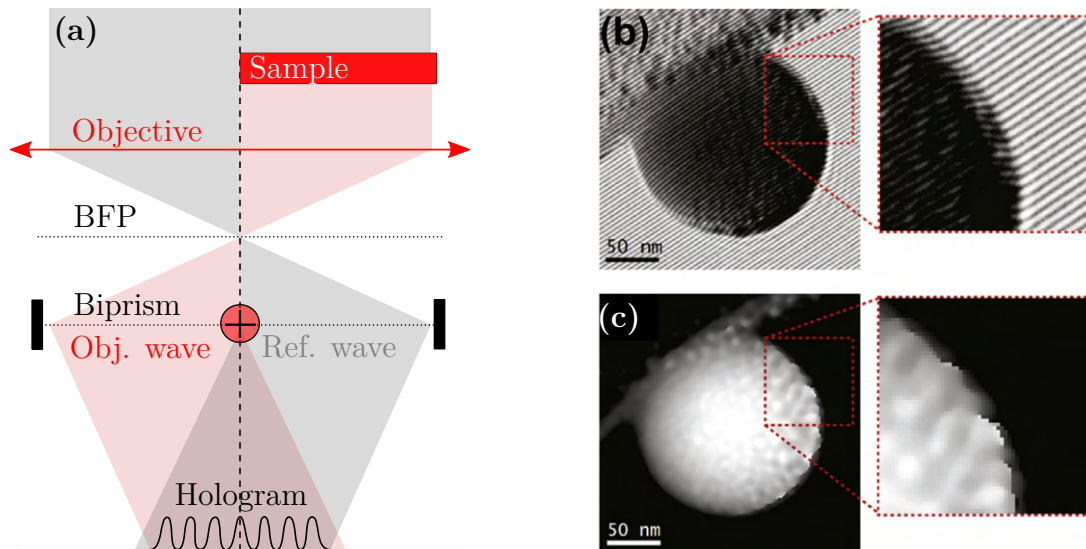
Figure 3.5: Electron holography in TEM. (a) TEM electron holography setup with a specimen deviated from the optical axis and the biprism. **(b)** Example of the electron hologram showing interference fringes. **(c)** Phase shift distribution reconstructed from **(b)**. Adapted from [112].

Electron magnetic circular dichroism

Analogically to XMCD, we can utilize the *electron magnetic circular dichroism* (EMCD) to probe magnetism in TEM. EMCD is based on the formal equivalence of the X-ray polarization vector and momentum transfer vector during inelastic electron scattering. Hence, subtraction of two EELS spectra formed from a different set of diffracted beams provides magnetism-related information analogous to XMCD [108]. EMCD recently demonstrated its capability to study magnetism in TEM up to the atomic scale [113, 114, 115, 116]. An important factor is that there is no need for the field-free TEM operation mode to acquire EMCD data [108]. More general information related to this technique can be found in [117, 118].

3.4. State of the art magnetic imaging in TEM

Ideal TEM imaging of MPT requires sensitivity to both magnetic phases associated with the transition, i.e., FM and AF phases. The capability to detect and analyze both phases of the MPT separately opens a vast playground to study interactions and correlations between the individual phases. The imaging will be probed on the equiatomic FeRh system.

FM materials have been conventionally studied using various techniques described in section 1.4.1 including TEM, for decades. Therefore we do not cover the state of the art of FM imaging using TEM performed in the field-free mode. On the other hand, the lack of stray field and macroscopic magnetization in AF prohibits magnetic imaging in TEM. Recent advances in HR imaging brought the first pioneering studies towards atomic-scale magnetic field mapping in AF [11]. TEM analysis of AF has the potential to become a revolutionary imaging technique in the rapidly evolving research of AF. Ultimately, this can lead to a better understanding of more complex phenomena involving AF, such as MPT. The following text provides state of the art of TEM imaging of AF, together with the TEM analysis of MPT in FeRh. All published MPT mapping studies in FeRh only deal with FM detection in TEM, and AF magnetism is not studied by any means.

3.4.1. TEM analysis of antiferromagnets

There have been two approaches used for the magnetic analysis of AF materials using TEM.

Loudon in 2012 [119] uses electron diffraction in TEM for the structural analysis of AF NiO, where AF peaks are formed corresponding to AF periodicity. It was observed that these peaks vanish when the specimen is heated above the Néel temperature. This technique allows only AF analysis at the scale of hundreds of nm and does not resolve magnetism-related information locally.

High-resolution mapping of internal magnetic fields in AF CuMnAs has been published recently by Křížek, et al. [11], in which high-resolution DPC is used for AF domain mapping. Visualization of antiparallel aligned magnetic moments of Mn atomic columns in CuMnAs demonstrates the enormous potential of atomic resolution DPC. It was shown that even TEM without a probe-corrector is capable of detecting local magnetic signal in AF. An example of atomically sharp AF domain structure visualized by DPC is shown in Figure 3.6. Besides the atomically resolved magnetism in TEM, a more profound understanding of magnetic signal at atomic resolution provides better insight into the interpretation of high-resolution DPC data [96], which are essential for novel techniques such as integrated DPC [13].
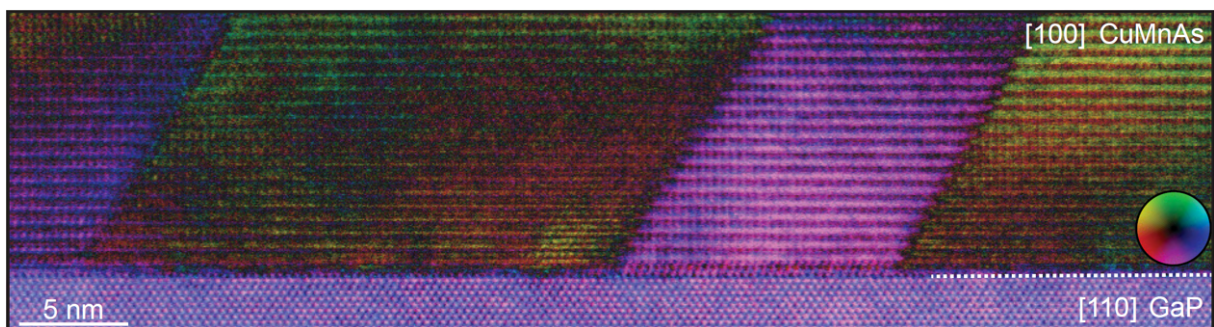
Figure 3.6: Antiferromagnetic domains imaged by DPC. An overview image of an AF CuMnAs thin layer in a cross-section lamella acquired by high resolution DPC. Adapted from [11].

3.4.2. MPT imaging in TEM

TEM has already been utilized for the analysis of MPT due to its versatility. Properties of MPT of the FeRh alloy have been introduced in section 1.5. FeRh is used as a model system due to its MPT accessibility in the vicinity of room temperature, hence optimal for experimental evaluation of the MPT imaging. Besides magnetism, chemical properties of FeRh thin layers using TEM EDX were extensively characterized in [120].

As stated before, sample fabrication is a crucial step for any TEM analysis. Ideally, the sample fabrication process should not modify the sample properties and not even the MPT. A characteristic property of MPT is transition temperature, reflecting various parameters of the specimen, such as strain [59] or amorphization [53]. Table 3.1 compares MPT thermal shifts from published studies in which MPT was probed by magnetism sensitive techniques in TEM. In [121], several sample fabrication procedures have been tested. Although the highest homogeneity was reached for FIB fabricated lamellae, no MPT was detected for $T > 0$ °C showing a decrease of MPT temperature of more than 60 K compared to the continuous film. The best results were reached using a NiAl buffer layer underneath FeRh, showing nearly no transition temperature shift with respect to the continuous film. The reason might originate from the fact that the NiAl buffer layer enhances atomic order in the AF phase leading to bulk like MPT even in layers thinner than 20 nm. On the other hand, NiAl introduces a more considerable lattice mismatch with respect to FeRh on MgO [122]. An HF etched FeRh thin layer measured in [121] showed a decrease of MPT temperature of 20 K. A significant reduction of 65 K in MPT temperature was also observed in [123]. FIB lamella annealing introduced in [124] led even to an increase of the transition temperature by more than 20 K. Effects of structural reconstruction accompanied by elemental intermixing with neighboring layers are expected to cause the rise of the MPT temperature [61].

The significant thermal shift from [121, 123] can be correlated with the modifications of MPT temperature measured on confined structures fabricated by EBL in [51]. In this study, a decrease of 20 K between 300 nm wide wires and micron-sized structures was detected, caused by strain relaxation.

Concerning the origins of these significant MPT shifts, the majority of the specimens were fabricated using FIB. Therefore, a certain level of lattice amorphization by Ga ion beam irradiation and geometrical confinement accompanied by strain relaxation are expected. The strain relaxation effect on MPT position comes from the bias between the lattice parameters of individual phases in FeRh [59]. However, if geometrical confinement relaxes the strain, transition goes back to its natural form, which results in the MPT shift. It is expected, that all reported shifts of FeRh MPT most probably result from the interplay between the spatial confinement, strain relaxion, and the sample fabrication process.

The FeRh FM phase was imaged using EH by Gatel [123], and using DPC by Almeida [124], to identify spatially resolved transition and phase coexistence across the thin layer profile. Both studies prove the concept of residual interfacial FM thin layers induced by strain and elemental stoichiometry variances close to the interface [125]. An extensive analysis by Gatel shows the evolution of MPT temperature across the layer profile with an extension of the MPT in interfacial regions with a reduced transition temperature. These data are shown in figure 3.7. Such interface-induced effect extends up to 15 nm into the FeRh layer, proving the importance of the interfaces. Unique high resolution field-free

Table 3.1: MPT shifts induced by TEM sample fabrication. Specimen properties from selected publications with the indicated sample layout, TEM specimen fabrication technique, magnetism sensitive technique used in TEM and resulting transition temperature shift defined as $\Delta T = T_{\text{MPT,bulk}} - T_{\text{MPT,TEM}}$. * = lamella annealing at 873 K for 1 h.

Ref.	Sample layout (nm)	Sample fabrication	Mag. TEM	ΔT (K)
[121]	MgO/FeRh (53)	FIB lamella (IP)	DPC	>60
[121]	GaAs/NiAl (40)/FeRh (50)	FIB lamella (IP)	DPC	<5
[121]	MgO/FeRh (45 - 50)	HF etching of MgO	DPC	~20
[123]	MgO/FeRh (50)	FIB lamella (OOP)	EH	~65
[124]	MgO/FeRh (53)	FIB lamella (OOP)*	DPC	-25

EH imaging in [123] reaching 0.5 nm has been achieved in a dedicated Lorentz mode setup with the B-core corrector in a 2-biprism configuration of electron holography [126]. Propagation of the FM phase from the FeRh/MgO interface has been confirmed using DPC in the study by Almeida [124], where DPC images of a cross-sectioned FeRh layer were taken at various temperatures.
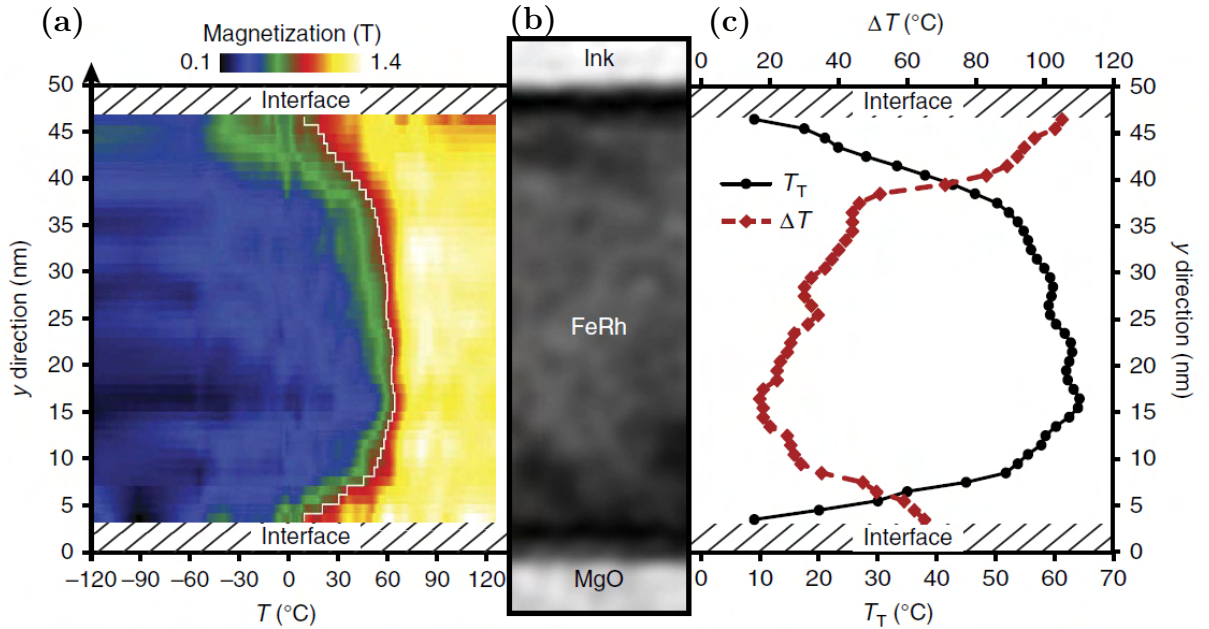
Figure 3.7: Ferromagnetic phase across an FeRh thin layer. (a) Temperature dependence of the FeRh magnetization as a function of the layer depth demonstrating the interfacial effect on MPT in FeRh. **(b)** TEM amplitude image of a specimen cross-section. **(c)** Transition temperatures T_{T} together with the transition width Δ_{T} showing the correlation between high T_{T} and low Δ_{T}. Adapted from [123].

4. Experiment

The experimental part of this thesis is divided into several subsections covering various aspects of TEM analysis of metamagnetic thin films. After summarizing the experimental setup used for the analysis, the comparison of different TEM sample fabrication processes is presented. The subsequent magnetic analysis in TEM is performed using DPC. Firstly, the basic principles of DPC are demonstrated on an amorphous FM material and then on a non-magnetic crystalline material to understand the DPC signal formation, the effect of the magnetic field, and the consequences of sample crystallinity. The influence of sample internal magnetic field will be demonstrated on permalloy nanostructures fabricated using *electron beam lithography* (EBL) on amorphous Si_3N_4 membranes. DPC analysis of crystalline samples will then be presented for a non-magnetic MgO monocrystal. This knowledge will then justify the DPC analysis of metamagnetic FeRh further supported by evaluating structural and elemental properties. The final part presents DPC mapping of an in-situ heated FeRh lamella to study the temperature evolution of magnetism in TEM.

4.1. Experimental setup

TEM analysis has been performed in FEI Titan^{TM} Themis 60-300 cubed microscope at the CEITEC Nano core facility in Brno. A high brightness Schottky X-FEG electron gun produces ane electron beam which can be accelerated up to 300 kV. All measurements presented were acquired at the accelerating voltage of 300 kV. A 3-lens condenser system defines the probe properties. The microscope is equipped with a spherical aberration CEOS GmbH image corrector. The detection system includes a fluorescent screen, 16 MPx 16 bit CMOS-based CETA 16M^{TM} camera with an optically-coupled scintillator, and a set of STEM detectors including BF, two DF, and HAADF semiconductor-based detectors. The upper DF detector is a DPC optimized 4-segment detector. A double tilt CompuStage holder from the FEI company was used for all experiments performed at room temperature. In-situ heating experiments were performed using the **Fusion Select** sample holder by the Protochips company.

Protochips Fusion Select is a holder for in-situ heating and electrical characterization in TEM. It combines the options of specimen double-tilt while heated and electrically biased. The sample-loading part of the holder is shown in Figure 4.1 **(a)**. There are six electrical channels connected to the sample chip (indicated by the green rectangle) through metallic needles. Figure 4.1 **(b)** shows the geometry of an electro-thermal chip allowing simultaneous heating and electrical biasing of the sample loaded onto the chip. Metallic needles, schematically shown in the image, electrically connect the holder to metallic conductive stripes on the chip leading to the close vicinity of the specimen. Individual channels are indicated by letters, where channels A and F are used for heating and the remaining four channels B, C, D, and E for electrical biasing. The area for TEM imaging is further magnified in Figure 4.1 **(c)**. Heating is realized by electrical biasing of the SiC layer indicated by gray color through channels A and F. The remaining electrical contacts surround nine electron transparent circular windows optimized for TEM imaging.
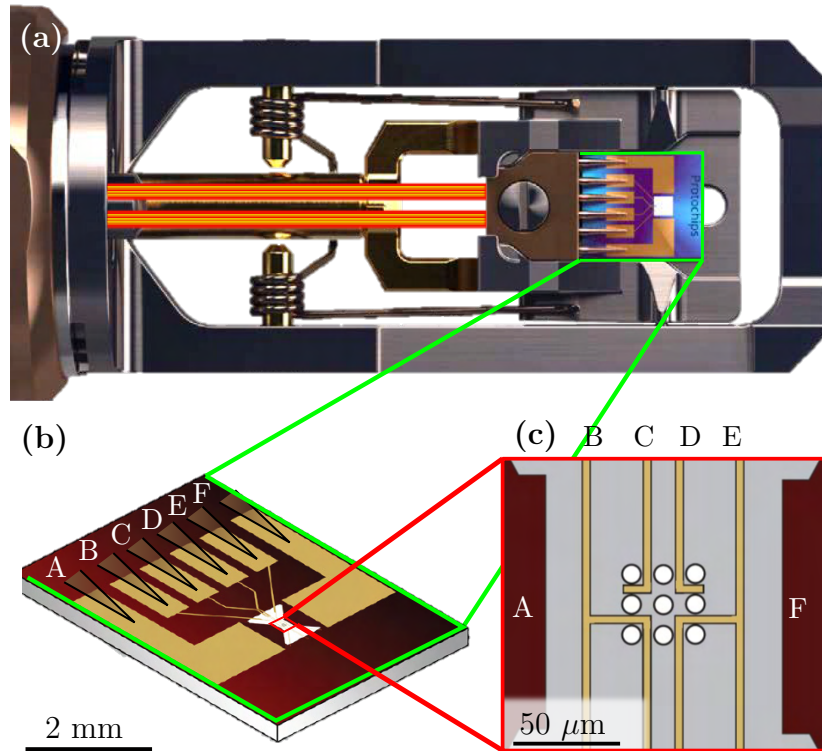
Figure 4.1: In-situ TEM setup. (a) Top view of the Fusion Select TEM holder by Protochips^{TM}. **(b)** Electrothermal chip used as a specimen holder with six electrical channels indicated by letters A to F. Red rectangle shows the position for lamella loading which is further magnified in **(c)**. **(c)** Chip area for the final loading of the lamella. Yellow stripes represent W conductive paths connected to individual electrical channels. Channels A and F provide electrical biasing of the SiC grey layer serving as a heating element of the lamella. The remaining ones serve for electrical biasing of the specimen.

FIB/SEM based experiments, containing mainly TEM lamella fabrication, were done using a dual-beam FEI Helios NanoLab 660 setup. A Schottky FEG electron source as well as Ga liquid metal ion source operate up to 30 kV. Additional 3D movements of the sample stage, including stage rotations, a nano-manipulator (NM), and GIS system for electron and ion beam induced deposition (EBID and IBID, respectively), make the system optimal for TEM lamella observation and fabrication.

EBL of permalloy structures on the membrane was performed using an SEM/E-beam writer MIRA from Tescan equipped with the Lithography system Raith Elphy plus. Electrons are emitted from a Schottky cathode and can be accelerated up to 30 kV. The laser interferometry stage offers exact stage movement essential for EBL.

4.2. TEM sample fabrication processes

The importance of fabrication processes on the resulting quality of TEM analysis has been introduced in section 2.3 including the descriptions of individual fabrication processes. We aim to evaluate the resulting sample properties, as well as the versatility, convenience,

and reproducibility of each fabrication approach. In particular, lamella fabrication using FIB and chemical detachment of the FeRh thin films will be tested.

Lamella fabrication by FIB

TEM lamella fabrication using dual-beam systems became very popular for TEM samples due to the relative simplicity of the process, its convenience, and relatively broad SEM/FIB dual-beam systems availability. There are two basic geometries of FIB made cross-section lamellae corresponding to the schemes provided in Figure 2.4 **(g)**.

Characterization of the lamellae made from FeRh thin films grown on MgO is shown in Figure 4.2. TEM images of MgO/FeRh lamellae welded from one side and from two sides to the TEM lamella grid are shown in Figure 4.2 **(a)** and **b**, respectively. A defocus of 3 μm highlights the rapid evolution of diffraction contrast across the specimen, suggesting significant lattice bending. This effect comes from the ion beam-induced internal stress in MgO and can be partially reduced by a more frequent alternation of the lamella sites during polishing. Enhanced robustness of the lamella is reached in the geometry provided in Figure 4.2 **(b)** due to the solid mechanical support from both sites, which stabilizes the lamella from its macroscopic deflection.

TEM micrograph in Figure 4.2 **(c)** acquired from a region indicated in 4.2 **(a)** shows a well-defined profile of the FeRh thin layer within the lamella. On top of the FeRh film, a 2 nm thick Pt capping layer is deposited as a protective layer. The area from the yellow rectangle was used for EDX mapping provided in Figure 4.2 **(d)**. Atomic elemental ratios were extracted from the EDX mapping and are plotted in Figure 4.2 **(d)**. EDX scan proves very little Ga contamination of the FeRh thin layer itself. Only a weak diffusion of the Fe and Rh atoms into the C capping is observable. Interfacial elemental diffusion is significantly reduced by the Pt capping layer created directly after FeRh deposition. Ideally, we would expect equivalent ratios of Fe and Rh in the thin layer and Mg and O in the substrate. These equivalences are broken partially due to the automatic process of EDX quantification and different diffusion properties of the elements within the neighboring atoms.

Considering the subsequent TEM magnetic analysis, particularly of the FeRh AF phase, well adjustable configuration of the FeRh lattice with respect to the electron beam is required. Optimal configuration can be conveniently reached during the versatile FIB lamella fabrication by adjusting the bulk sample lattice orientation with respect to the initial FIB milling direction. This aspect is further described in section 4.4.2

MgO substrate etching

Besides the traditional cross-section lamella geometry, there are other ways of reaching electron transparency to analyze thin films in TEM. One approach is to peel off the thin layer from the substrate. In the case of MgO substrate, this can be done through chemical etching with an aqueous solution of ethylenediaminetetraacetic acid (EDTA), which releases Mg^{2+} ions into water and dissolves the MgO. At the same time, it leaves the FeRh layer chemically and structurally intact [127]. TEM sample fabrication together with the TEM analysis is summarized in Figure 4.3. The process of releasing of a 20 nm thick FeRh thin film releasing from an MgO substrate is schematically provided in Figure 4.3 **(a)**. Etching was performed in a 0.3 M solution of EDTA disodium salt at 75
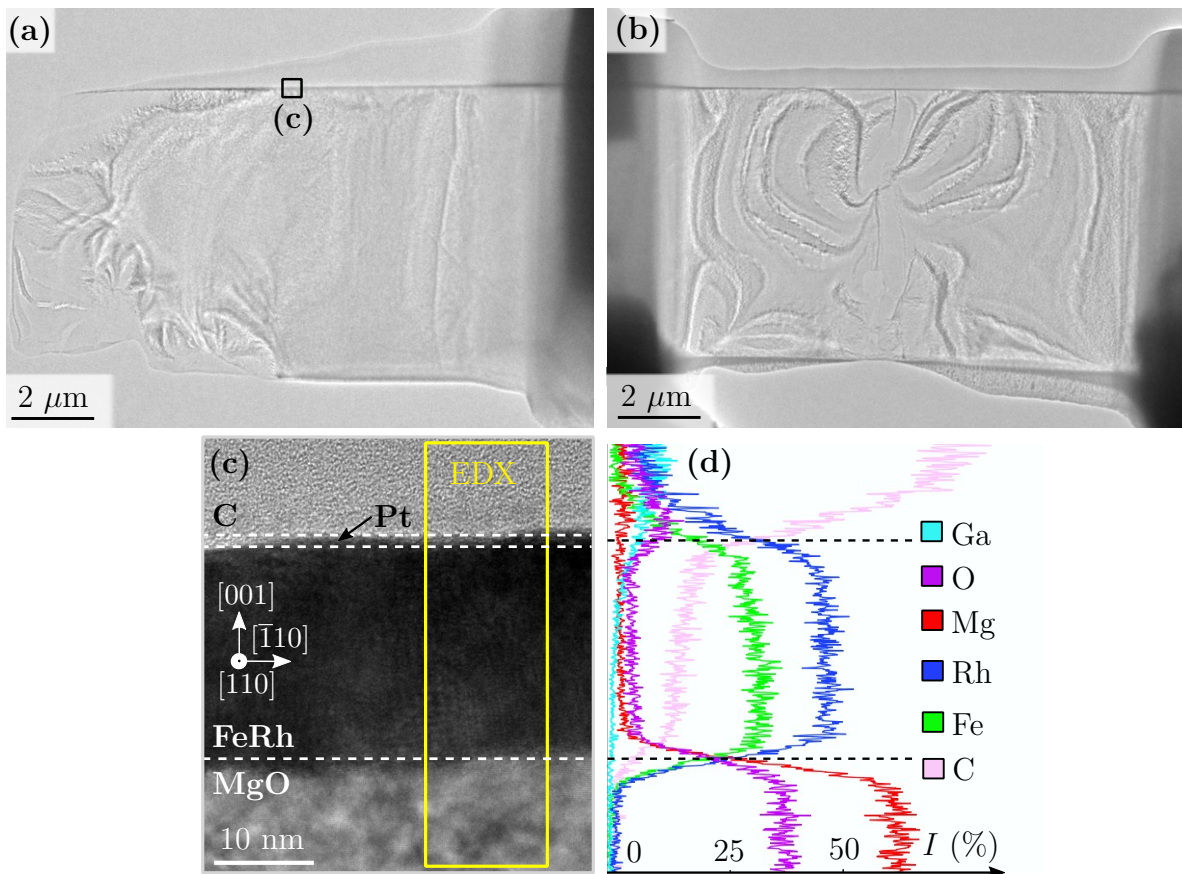
Figure 4.2: Characterization of TEM lamellae. TEM micrographs with a defocus of 3 μm of the lamellae welded from **(a)** one side, **(b)** two sides, to the TEM lamela grid. **(c)** TEM micrograph acquired from the region indicated in **(a)** showing the FeRh thin layer profile including the scheme of the area used for EDX analysis. **(d)** EDX atomic ratios profile providing well defined elemental distribution within the lamella.

°C, and the FeRh layer was released after 6 hours of etching. The FeRh layer floating on the solution surface was then carefully transferred onto a piece of paper. A photo of the layer detached from the MgO substrate and placed on a paper in Figure 4.3 **(a)** shows a slightly disrupted layer after the removal from the solution. The lattice mismatch between MgO and FeRh represents the main origin of the thin layer bending, which highly degrades the whole process. The extremely fragile freestanding FeRh layer immediately crumbles into μm-sized FeRh flakes. These flakes were then transferred onto a TEM holey grid. Lucie Motyčková did the etching process. A detailed analysis of releasing FeRh films from MgO substrates can be found in her Master's thesis [127]. A TEM micrograph of the FeRh flake, presented in Figure 4.3 **(b)**, confirms the significant bending of the dissolved FeRh flakes. An extreme level of the FeRh lattice bending results in intense diffraction contrast. An HRTEM image of the lattice within one of the FeRh flakes is provided in Figure 4.3 **(c)**. Locally well-ordered FeRh lattice confirms structurally intact FeRh lattice after etching. FeRh crystallinity and BCC lattice-type orientation are evident from the SAED diffraction pattern provided in the image inset. TEM images from Figure 4.3 were acquired by Marek Vaňatka.
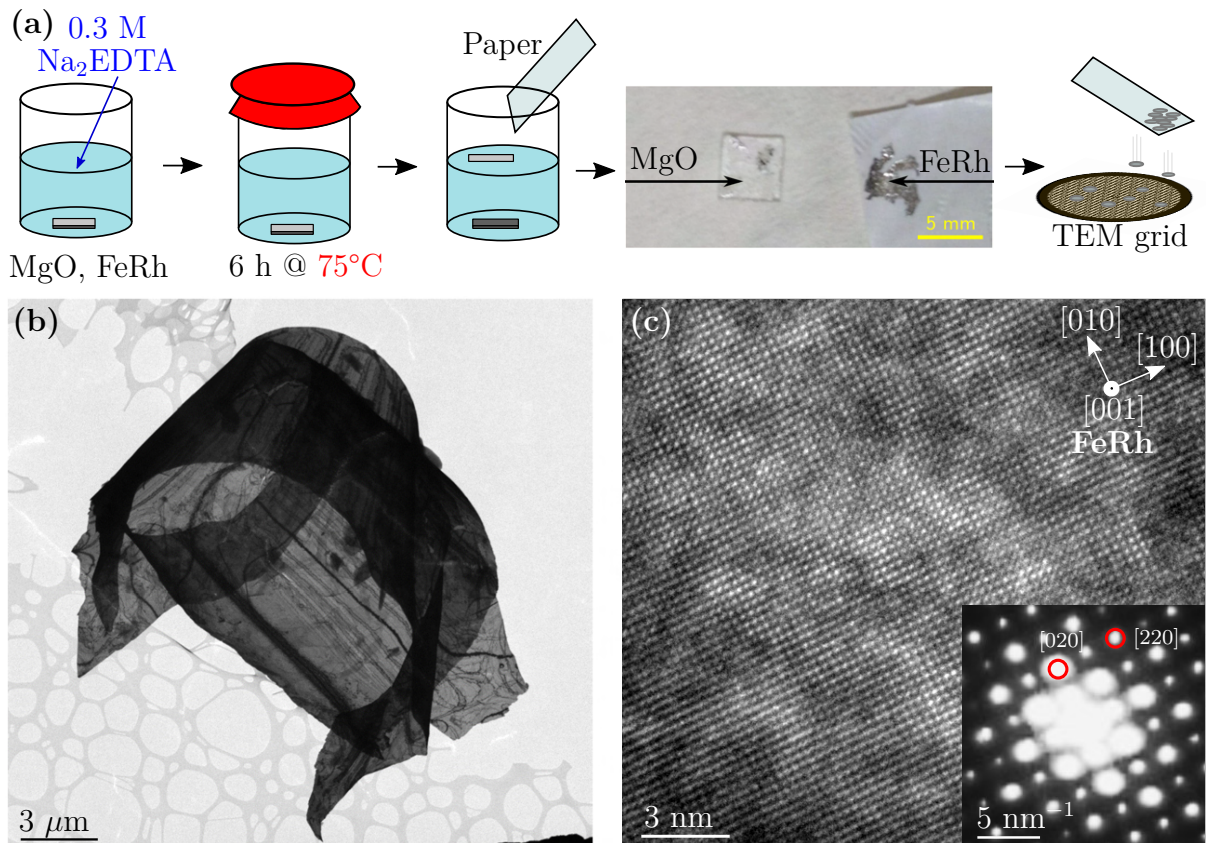
Figure 4.3: Chemical detachment of FeRh from MgO. (a) Process of chemical etching, in which an MgO substrate with a thin FeRh film deposited on top was put into a 0.3 M solution of Na$_2$EDTA for 6 h at an elevated temperature of 75 °C. The released layer was then transferred onto a piece of paper as shown in the photo adapted from [127]. The freestanding FeRh film crumbled into μm-sized flakes, which were then transferred on the TEM grid. **(b)** TEM micrograph of an FeRh flake on a holey grid showing significantly bent topology with highly pronounced diffraction contrast. **(c)** HRTEM image of the FeRh lattice confirming the maintained crystallinity of the specimen. The FeRh BCC lattice and its orientation was extracted from the SAED pattern provided in the inset.

To sum up, the chemical process of FeRh detachment from the substrate results in amorphization-free FeRh freestanding films. Significantly limited control of the sample geometry and its crystallographical orientation represent the main drawbacks of this sample fabrication procedure. Besides that, a highly deformed FeRh lattice may affect the material properties, which is not suitable for the subsequent TEM analysis.

Outcome of the sample fabrication processes

Specimen fabrication is a crucial step for the TEM analysis, and two different sample fabrication strategies for the TEM analysis of thin films were tested. In our case, we seek a reproducible sample fabrication process with a minimized influence of the fabrication procedure on the specimen to maintain the sample properties unchanged in order to provide relevant information about the bulk specimen.

Chemical etching represents an ion beam irradiation-free process to produce electron transparent specimens. However, curling-up of the strained FeRh layer after detachment

limits the usability of this process significantly. Fragility of the freestanding FeRh flakes also limits the reproducibility of the process. On the other hand, lamella fabrication represents a versatile process producing decent uniform electron transparent specimens. Lamella bending can be partially reduced by welding the lamella from both sides to the TEM grid. Ga implementation seems to be well controlled within the FeRh thin layer, particularly when protected by a thin Pt protective layer. The ability of the FIB fabrication to produce an adjustable FeRh lattice orientation of the lamella is also appropriate for magnetic analysis of the AF phase. Based on these factors, FIB lamellae fabrication will be exclusively used for further TEM investigation of FeRh thin films.

Room temperature DPC analysis of FeRh will be performed using lamellae geometry shown in Figure 4.2 **(b)**, fabricated by a conventional process introduced in Figure 2.4. However, in-situ TEM analysis requires a modified configuration for a successful lamella loading onto the chip shown in 4.1. The process, presented in Figure 4.4, is particularly valid for electro-thermal chip geometry from 4.1 **(b)**. The configuration of lamella transfer onto the chip is illustrated in Figure 4.4 **(a)**. A grey triangular stub holds the chip indicated blue. The close vicinity of the GIS gun to the chip requires lamella attachment to the NM under a non-zero angle, in our case 31°.

A small angle between the lamella and chip, optimally 7°, is required for successful polishing to the electron-transparent state. Subsequently, local IBID of tungsten is used for lamella attachment to the chip. On top of that, metallic W provides a conductive connection of the lamella to the chip, making this process suitable also for electrical biasing experiments. Sample geometry for the ion beam polishing is schematically shown in Figure 4.4 **(b)**, which is reached by stage rotation of 180° and an increase of the stage tilt angle from 7° to 14°. A non-zero tilt of the lamella with respect to the chip allows safe FIB polishing without damaging the supportive layer. The resulting state of the specimen after FIB polishing is displayed by the SEM image in Figure 4.4 **(c)**. An FIB-made groove behind the lamella was created to avoid FIB damage to the chip during the FIB polishing. The electron transparent region indicated by the yellow rectangle is magnified in Figure 4.4 **(d)**. The final lamella was made from a metamagnetic, 60 nm thick FeRh layer deposited on an MgO substrate. MPT properties of the thin film specimen used for the lamella fabrication are provided by *vibration sample magnetometry* (VSM) in Figure 4.4 **(e)**. VSM maps the overall sample magnetization upon both heating and cooling in an IP applied magnetic field of 1 T. The diamagnetic response of the sample to magnetic field was corrected. The transition begins at 360 K and the FeRh is fully FM above 390 K upon heating. An FeRh thin film with a relatively high MPT temperature with respect to the room temperature was selected due to previously published significant reduction of the MPT temperature in the FeRh lamellae [123].

4.3. Signal evaluation of DPC

TEM magnetism sensitive techniques have been introduced in section 3.3. The DPC will be used exclusively due to its direct link between the measured signal and internal electric and magnetic fields within the specimen. Besides that, this technique is capable of mapping field distributions down to the atomic scale. The TEM setup used for the experiments is equipped with a 4-segment DF STEM detector collecting four integrated signals
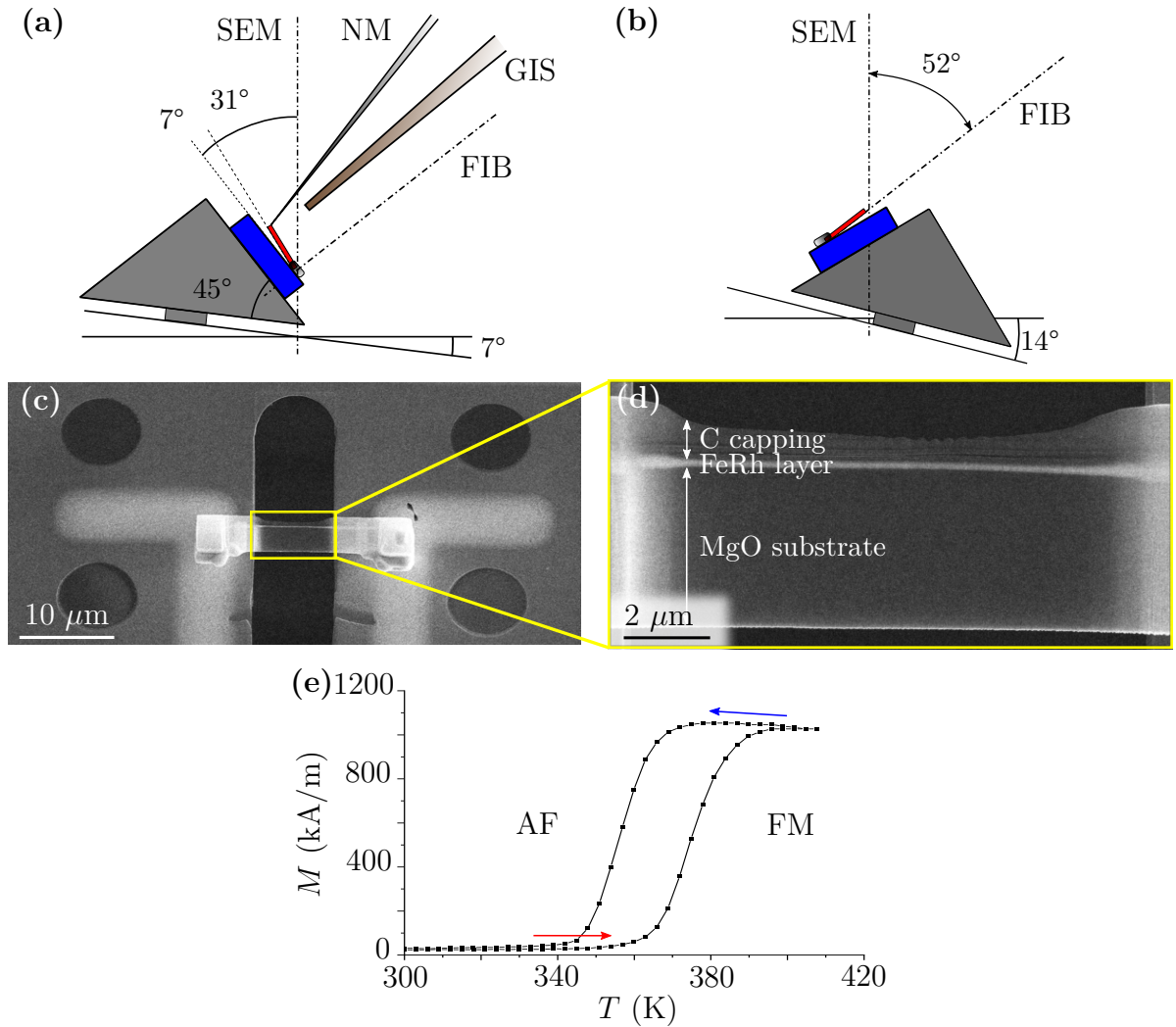
Figure 4.4: Lamella fabrication process for in-situ TEM analysis. **(a)** Dual-beam system configuration for the lamella loading onto the electrothermal chip. Pre-tilt of the lamella with respect to the nano-manipulator of 31° prevents the chip from collision with the GIS tube. **(b)** Dual-beam system configuration for the final ion-beam polishing. Lamella tilt of 7° from the chip protects the fragile chip from ion beam damage during the polishing process. **(c)** SEM image of the final electron transparent specimen after polishing. Area in the yellow rectangle is further magnified in **(d)**. **(d)** Detail of the electron transparent region showing the specimen layout. Thickness of the FeRh layer is 60 nm. **(e)** Temperature dependence of bulk FeRh specimen used for the sample fabrication process measured by VSM. The FeRh thin film undergoes transition from the AF to FM phase in the range of 360 K to 390 K. The VSM loop was acquired by J. A. Arregi.

from individual segments. Subtraction of the signal from opposite segments provides information about the angular intensity deflection of the CBED pattern, representing an origin of DPC signal formation. Full CBED patterns for specific specimen spots can be visualized only manually using the fluorescent screen or CETA camera.

TEM magnetic imaging of FM ordering requires reduced objective lens excitation to limit the immersive magnetic field of the specimen. Based on that, the IP magnetization

component of the sample is preserved, resulting in the magnetic DPC signal. Reduced objective excitation is reached by using the so-called *low-magnification* (LM) mode operating at 4.24 % of the objective excitation available both for the CTEM and STEM modes. The specimen is immersed in a magnetic field of approximately 140 mT created dominantly by the objective lens upon these conditions. A minor component of 7 mT comes from the mini-condenser lens. This field is sufficiently low to maintain a particular FM signal within the specimen. A fully compensated magnetic field-free mode in DPC STEM can be reached through combined condenser and objective focusing. Desired objective excitation is set in the focusing-by-objective regime. The resulting defocus is then compensated by re-excitation of the condenser system. According to the discussion provided in section 1.4.2, antiparallel ordering of atomic moments should be kept even in the magnetic fields applied by the objective, allowing HR DPC imaging of the AF phase as demonstrated in [11].

The DPC analysis of magnetism in crystalline specimens requires an understanding of magnetization- and crystallinity-induced signal. The following section evaluates a pure magnetic DPC signal originating from the amorphous FM permalloy microstructures in the LM-DPC regime. Secondly, DPC imaging of a non-magnetic MgO monocrystal is presented. Understanding the DPC signal formation within these two basic systems justifies analyzing the magnetic properties of complex metamagnetic systems via DPC.

4.3.1. DPC in amorphous ferromagnets

Demonstration of magnetization-induced DPC signal formation is performed on amorphous permalloy (Py, $Ni_{80}Fe_{20}$) microstructures. The specimen was fabricated by an EBL lift-off processing of a 30 nm thick Py film evaporated on a 30 nm thick Si_3N_4 membrane. Marek Vaňatka did the complete sample fabrication. Results of the DPC analysis on Py microstructures are presented in Figure 4.5.

A scheme of the final specimen configuration in TEM is provided in Figure 4.5 **(a)**. The DPC analysis is performed on 3 μm Py squares. The area without Py contains only an amorphous membrane producing no macroscopic DPC signal. Therefore, all DPC signal is considered to be of a magnetic origin. Hence, the plotted signal direction corresponds to the sample internal $\boldsymbol{B}$-field distribution. DPC mapping of square-like structures is provided in Figure 4.5 **(b)**. The image was acquired in the LM imaging mode resulting in the applied OOP objective field of 140 mT. External field results in magnetic configurations of Py squares deformed from their ground state represented by the Landau pattern. A clear displacement of the vortex cores from the centers of the Landau patterns indicates a non-zero IP component of the external magnetic field, which can be compensated by the sample tilt. A field-free operation mode with a fully compensated objective field brings the Py magnetization back to the undisturbed Landau pattern, as indicated in the inset by the yellow rectangle. 2D DPC data allow vectorial magnetic field maps to be extracted from the images, as shown in Figures 4.5 **(c)** and **(d)** taken from the regions indicated in 4.5 **(b)**. As DPC maps the $\boldsymbol{B}$-field distribution in the sample, the signal arises predominantly from the Py magnetization within the microstructures, as shown in 4.5 **(c)**, whereas in the structure surroundings the DPC maps the IP stray field projection, provided in 4.5 **(d)**.

The magnetic signal of the Py microstructures originates from the uniform deflection of the CBED pattern shown in 4.5 **(c)** acquired from the positions indicated in 4.5 **(b)**
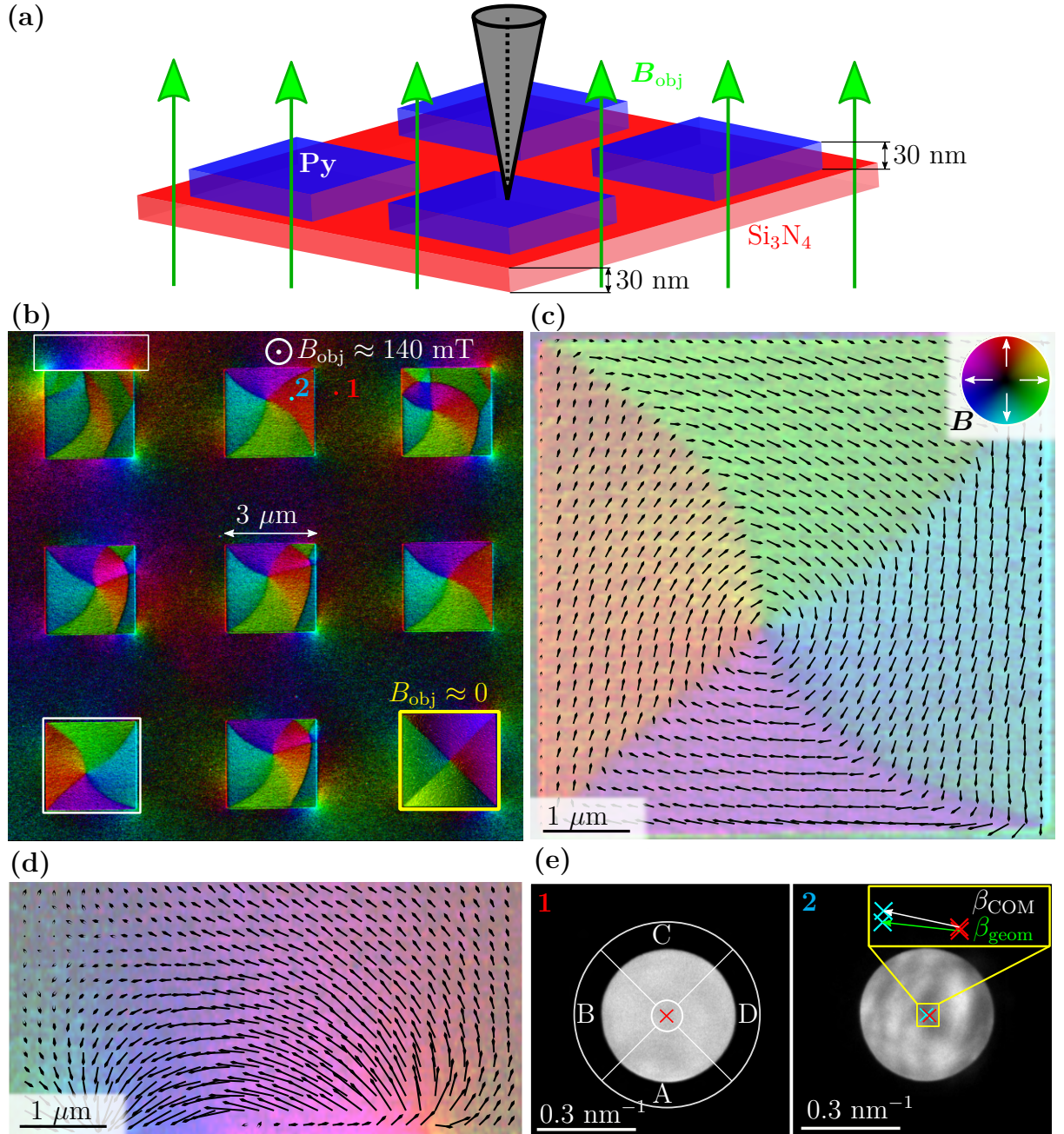
Figure 4.5: LM-DPC of permalloy microstructures. **(a)** Geometry of the membrane with Py microstructures within the TEM. **(b)** LM-DPC map of the sample showing the internal magnetic configuration of the specimen with the OOP objective field of 140 mT. White boundaries indicate regions used for vectorial magnetic field mapping in **(c)** and **(d)**. Inset in the yellow frame shows the magnetization state of a Py square acquired at field-free conditions. **(c)** Vectorial map of the B-field within the Py square. **(d)** Magnetic stray field distribution in the vicinity of the FM Py square. **(e)** Central discs of CBED patterns acquired on fluorescent screen taken from the positions **1** and **2** indicated in **(b)**. The central CBED disc with the radius α is deflected by angle β due to the presence of specimen magnetic field. Both the geometrical deflection of the disc β_{geom} as well as the calculated deflection of the COM of the CBED pattern β_{COM} are indicated.

by red and blue dots. Pattern **1** is acquired from the membrane and is considered to be magnetically unaffected. The angle α represents the radius of the CBED central disc. Pattern **2** is acquired from the Py domain resulting in a geometrical deviation of $\beta_{geom} \approx 19$ μrad. Considering the magnetic shape anisotropy of thin films introduced in section 1.3, a uniform IP magnetization across the whole Py thickness of 30 nm is assumed. By applying equation 3.6, we get the **B**-field amplitude of $B = 1.3 \pm 0.3$ T from the evaluation of the four CBED patterns. The saturation magnetization of Py gives the internal magnetic field of 1.0 T [28]. The discrepancy between the measured and calculated field amplitude values may result from the Py layer's local inhomogeneities after the sample fabrication process or relatively low resolution (512×512) px of the camera used for the CBED patterns acquisition. All diffraction patterns were acquired using an electron beam convergence angle of 0.2 mrad, determining the angular size of the central CBED disc diameter of $\alpha = 214$ μrad. The projector camera length was set to 18 m. The resulting collection area of the segmented DPC detector is shown in the CBED pattern **1**. Intensity modulations present within the central CBED disc are of non-magnetic origin and may lead to a faint deviation of the DPC signal. The effect of a non-magnetic signal is embedded within the evaluation of the COM (defined by equation (3.7)) of the CBED patterns indicated by β_{COM}, which in total provide quantitatively the same results as the geometrical evaluation. The non-magnetic contribution is below the error of the analysis, which would not be the case in the evaluation of high-resolution CBED patterns. Quantitative evaluation of the DPC signal intensities provided by equations (3.8) and (3.9) turned out to be unreliable since the detected intensities from individual detector segments vary depending on the microscope alignment and settings. Calculated field amplitudes within Py microstructures using this approach extracted from multiple measurements gave the values ranging from 3 T to 5 T. These amplitudes are far from the values corresponding to the Py saturation magnetization.

To conclude, geometrical CBED pattern evaluation provides the most reliable **B**-field quantification. COM-evaluation of the CBED pattern is affected by the presence of a non-magnetic signal coming from the intensity modulation of the central CBED disc. However, in our case, the difference between the geometrical and COM quantification was below the error of the analysis. Direct **B**-field quantification from the acquired intensities is unreliable and varies depending on the TEM settings.

4.3.2. DPC in non-magnetic crystalline samples

The DPC signal originates from the uneven intensity distribution in the CBED pattern. The diffraction phenomena taking place in crystalline samples redistributes the CBED pattern intensity significantly. It is therefore expected that diffraction contrast (see section 2.2.4) will play a significant role in the DPC analysis of crystalline samples. Here we evaluate the DPC signal from the non-magnetic monocrystalline MgO lamella at the microscale and the atomic scale. In both cases, the TEM operates in a conventional objective-on mode allowing the operation down to the atomic resolution.

The experiments are summarized in Figure 4.6. The MgO lamella significant bent due to the FIB-induced lattice strain results in a well pronounced dynamical diffraction contrast. Since this signal belongs to the group of phase-contrast phenomena, the signal is expected to appear in DPC as well. An STEM BF image of the MgO lattice, provided in Figure 4.6 **(a)** shows the presence of this contrast. A DPC map of the same area
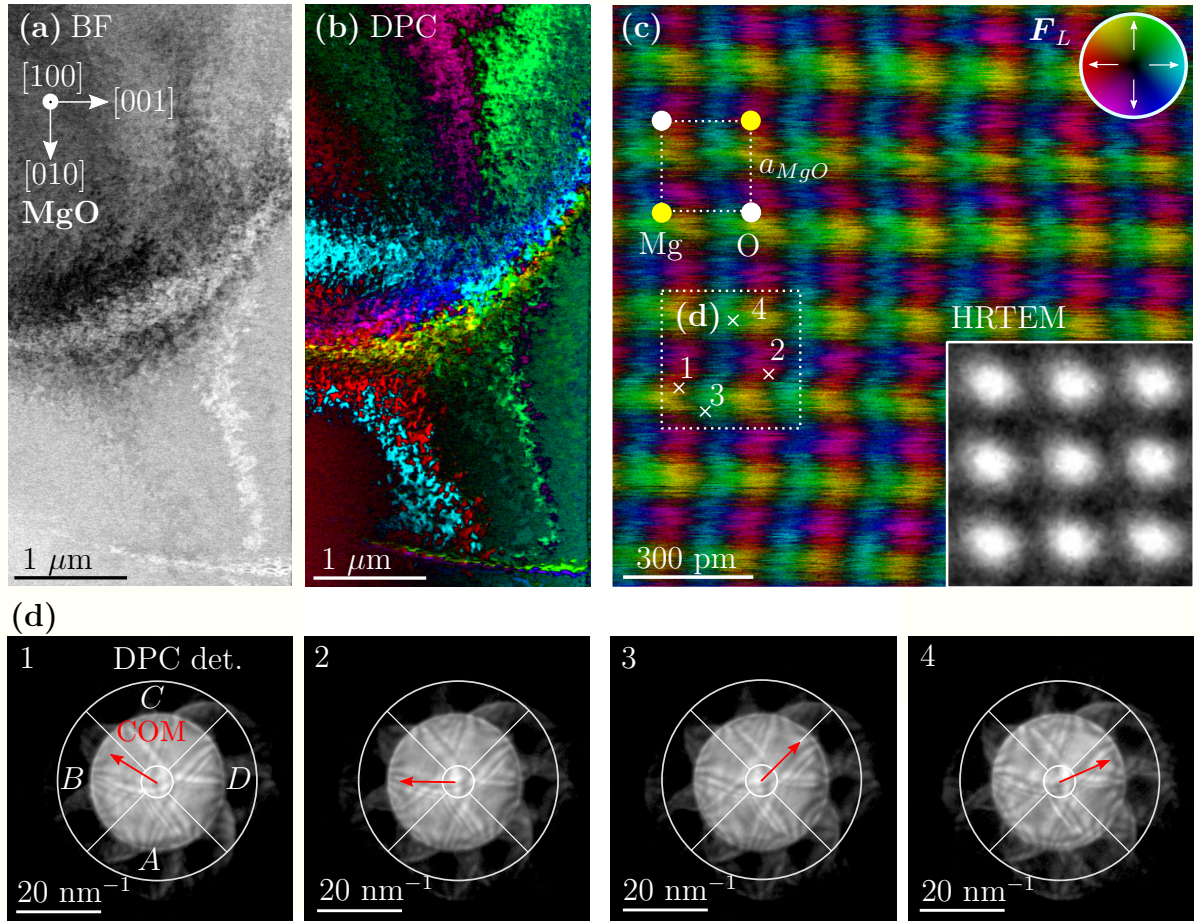
Figure 4.6: DPC in monocrystalline MgO. (a) BF STEM image of the MgO mono-crystalline lamella showing significant diffraction contrast lines. **(b)** STEM DPC scan of the identical region as in **(a)** manifesting the associated DPC contrast to the dynamical diffraction lines. **(c)** Atomic scale DPC of the MgO lattice demonstrating the capability to map radial electric field of individual atomic columns. Atomic positions are indicated both by the scheme of the unit cell and by the HRTEM micrograph in the right bottom corner. Numbers in the white dotted rectangle indicate the positions of the CBED patterns provided in **(d)**. **(d)** Demonstration of the DPC contrast formation through the CBED patterns acquired from the regions indicated in **(c)**. Intensity modulations of the CBED pattern result in the deviation of the COM from the center of the DPC detector. Indicated detector size corresponds to the real detector size at the used camera length. Red arrows indicate the deviation direction of the COM for each pattern.

is shown in Figure 4.6 **(b)** and demonstrates the intense effect of dynamical diffraction on the DPC. These contrast lines also indicate regions with a well-aligned zone axis offering the best lattice imaging conditions. Monocrystalline character of the specimen then allows mapping of electric field distribution surrounding the atomic columns as shown in Figure 4.6 **(c)**. The scheme of the MgO unit cell indicates the atomic column positions. The HRTEM inset of the MgO lattice in the right bottom part further correlates the DPC scan with the atomic column signal from the HRTEM mode. At this resolution, the effect of the signal blurring due to the beam profile introduced by equations (3.10) - (3.12) starts to play a significant role. Further evaluation of this blurring would require in-depth

data processing, which is beyond the scope of this thesis. Principle of the DPC contrast formation at the atomic scale is demonstrated in Figure 4.6 (d) on CBED patterns. These patterns were acquired from the different positions concerning the MgO atomic columns, which are indicated in Figure 4.6 (c). The effect of intensity modulation of the CBED pattern represents the main origin of the DPC signal. The direction of the accompanied DPC signal can be extracted by calculating the COM positions (defined by equation 3.7) of these patterns. Red arrows indicate directions of the COM deviations from the center of the DPC detectors for each CBED pattern. The signal strength is highly modulated by the intensity of higher-order diffracted discs, which hinders straightforward signal quantification. All images from Figure 4.6 were acquired with the beam convergence angle of 10 mrad, in the objective-on mode, with the projector system camera length of 360 mm. Evaluation of the crystalline samples using DPC confirmed the enormous importance of parasitic diffraction contrast, prohibiting the straightforward signal quantification within the crystalline specimens. This effect may become crucial during the investigation of atomic-scale magnetism, which is expected to produce orders of magnitude weaker signal compared to the atomic electrical fields as discussed in section 3.3.2. A faint deviation of the sample lattice from the ideal Zone axis alignment may limit the negative effect of this parasitic signal. Besides that, we managed to map the atomic DPC signal, which might be interpreted in a non-magnetic material as the radial electric field of the atomic columns. Importantly, in crystalline samples, the DPC signal originates from the intensity redistribution resulting from the interference phenomena within the overlapping regions of the diffracted CBED discs. However, it has been previously demonstrated that the presence of the field modulates the intensity of the CBED pattern accordingly; hence the COM of the CBED pattern is deviated [96]. These arguments justify qualitative equivalence between the HR DPC signal and electric and magnetic field distribution.

Previous characterization of the DPC signal proved the possibility of magnetic signal mapping and signal quantification only at the microscale in amorphous materials. This observation originates from the simplicity of the CBED patterns of amorphous materials without any presence of the higher-order diffracted discs. However, diffraction phenomena are unavoidable in crystalline samples. The corresponding overlap of the discs results in interference modulating the intensity distribution of the CBED pattern, as well as the DPC signal. The signal still provides information about the field distribution, but the signal interpretation and quantification become much more challenging. Successful analysis of the magnetic contrast in crystalline materials will require imaging conditions at which the magnetic signal dominates over the parasitic signals.

4.4. TEM analysis of FeRh

Metamagnetic materials undergoing MPT, such as FeRh, represent complex systems serving as a testbed to analyze an interplay between structural, electrical, and magnetic properties. All of these aspects can be probed within TEM. This section begins by summarizing the structural properties of FeRh using the TEM diffraction mode. Furthermore, magnetic analysis using DPC in the field-free and HR regimes together with chemical analysis helps to unveil the magnetic properties of FeRh using TEM. Finally, subsection 4.4.3 final part is devoted to the in-situ DPC analysis of FeRh upon heating.

4.4.1. Structural analysis of FeRh

Lattice properties of epitaxially grown thin layers are conventionally probed by X-ray diffraction techniques, allowing the structural characterization of the whole specimen. However, this approach does not provide local structural information, which can be efficiently obtained in TEM. In case of the parallel diffraction mode, the sample area is restricted by the SAED aperture. The smallest region used for the parallel beam diffraction corresponds to the circle with a diameter of 200 nm in the sample plane. Hence, the signal will always be mixed with the signal from neighboring layers in the thin-film geometry.

The results of structural analysis of an equiatomic FeRh thin film are shown in Figure 4.7. Figure 4.7 **(a)** shows the acquisition areas for individual diffraction patterns shown in Figures 4.7 **(b)** and **(c)**. Note that the acquisition regions are shown only schematically and that the patterns were acquired from two lamellae made from two different equiatomic 25 nm thick FeRh films. Figure 4.7 **(b)** provides the SAED diffraction pattern of the BCC lattice, which in equiatomic composition adopts metamagnetic behavior. Epitaxial BCC FeRh grows with a relative 45° IP rotation to the MgO NaCl-type lattice as indicated in the scheme reconstructed from the SAED pattern. Figure 4.7 **(c)** provides the SAED pattern demonstrating the presence of FCC FeRh within the lamella.
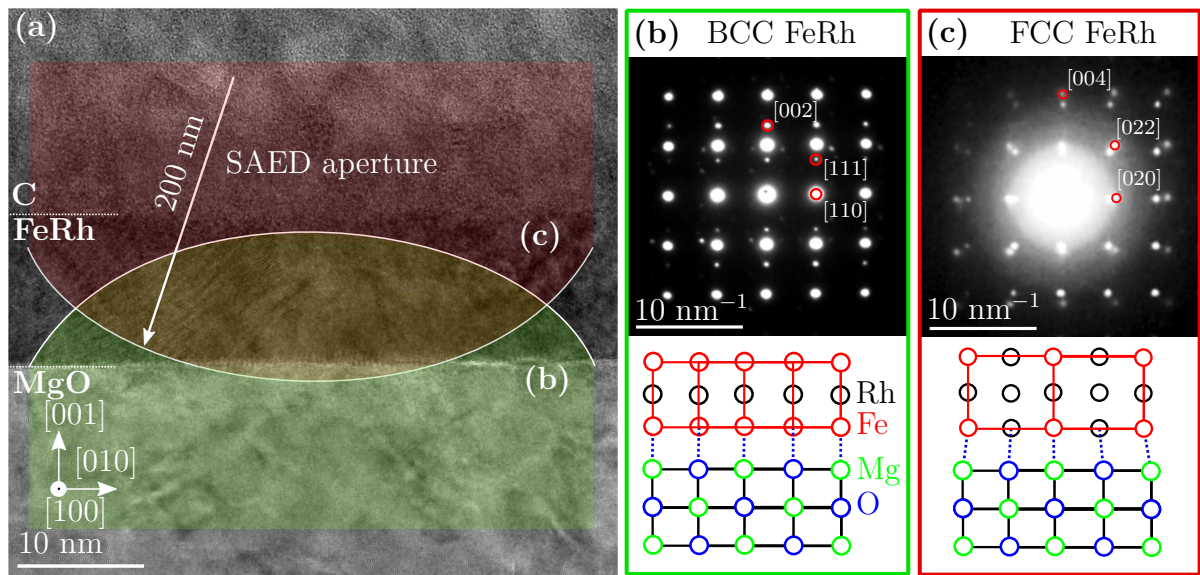
Figure 4.7: Structural analysis of equiatomic FeRh lattice. (a) TEM micrograph of the cross-section lamella schematically indicating the regions from which the diffraction patterns in **(b)** and **(c)** were acquired. **(b)** SAED diffraction pattern showing the BCC-FeRh lattice type characteristic for metamagnetic FeRh. Strong signal from the MgO lattice is visible in the pattern. Schematic atomic configuration reconstructed from the SAED pattern indicates a 45° rotation between the BCC FeRh and MgO lattices. **(c)** SAED diffraction pattern of the metastable FCC FeRh lattice. A strong signal from the amorphous carbon capping layer appears due to the major presence of the C capping in the probed area. A well-defined signal from the MgO substrate can be recognized as well. The reconstructed configuration shows no rotation of FeRh FCC lattice to MgO lattice.

Besides that, a strong parasitic signal from the amorphous C capping layer and well-defined MgO lattice signal can be distinguished. Their presence comes from the major presence of the C capping layer and minor presence of the MgO substrate in the area selected for the diffraction. Epitaxial FCC FeRh phase grows unrotated with respect to the MgO lattice, resulting in a lattice mismatch as high as 11 % [62]. The reconstructed lattice configuration is shown in the scheme below the FCC SAED pattern. Even though the FCC phase is not conventionally observed in XRD patterns of well-ordered equiatomic FeRh thin films [50], it can be found in FIB-made lamella. On the contrary to the study from Castiella, et al. [62], we observed this phase even in a lamella made from the metamagnetic FeRh. Its presence may arise from the local structural disturbances or the FIB irradiation.

In conclusion, TEM offers spatially resolved structural analysis of thin layers and can unveil various lattice types from the diffraction pattern. In optimally grown FeRh films, the BCC lattice corresponding to the bulk form dominates over the other lattice types. Apart from that, a minor presence of metastable FCC FeRh phase in the FIB made TEM lamella of the metamagnetic thin film was observed.

4.4.2. Magnetic and chemical analysis of FeRh

Previous evaluations of the DPC signal provided an insight into the field-free magnetic imaging and the field mapping on crystalline samples. Both of these aspects can be utilized for FeRh magnetic imaging in AF and FM phases. Among other material factors, a chemical ratio of Fe and Rh affects the FeRh magnetic state significantly. Fe rich FeRh does not undergo a phase transition and is fully FM. However, it keeps the BCC lattice same as the equiatomic FeRh.

TEM elemental and magnetic imaging of FeRh at room temperature are performed on two lamellae containing compositionally different FeRh layers. Both lamellae were analyzed using EDX to confirm the chemical properties of both samples and were imaged using DPC in LM field-free and conventional objective-on modes.

- *Sample 1* (FM FeRh) contains an Fe-rich ($Fe_{80}Rh_{20}$), 25 nm thick FeRh thin film grown on an MgO(001) substrate. Results of the FM sample analysis are provided in Figure 4.8.
- *Sample 2* (AF FeRh) includes a 60 nm thick layer of equiatomic FeRh grown on an MgO(001) substrate. The film undergoes a phase transition from the AF to FM phase in the range from 360 K up to 390 K. Results of the AF phase analysis are provided in Figure 4.9.

Analysis of FM FeRh

An LM DPC image of FM FeRh is provided in Figure 4.8 **(a)** showing a relatively uniform DPC signal indicating a uniformly magnetized FM layer, with magnetization oriented along the thin FM stripe. Figure 4.8 **(b)** shows the DPC scan of the FM layer immersed in a strong objective field of 2.1 T. The uniform signal suddenly vanishes in the strong applied field, which well corresponds to the alignment of the magnetization with the objective field. The remaining non-uniform DPC signal corresponds to the strain fields
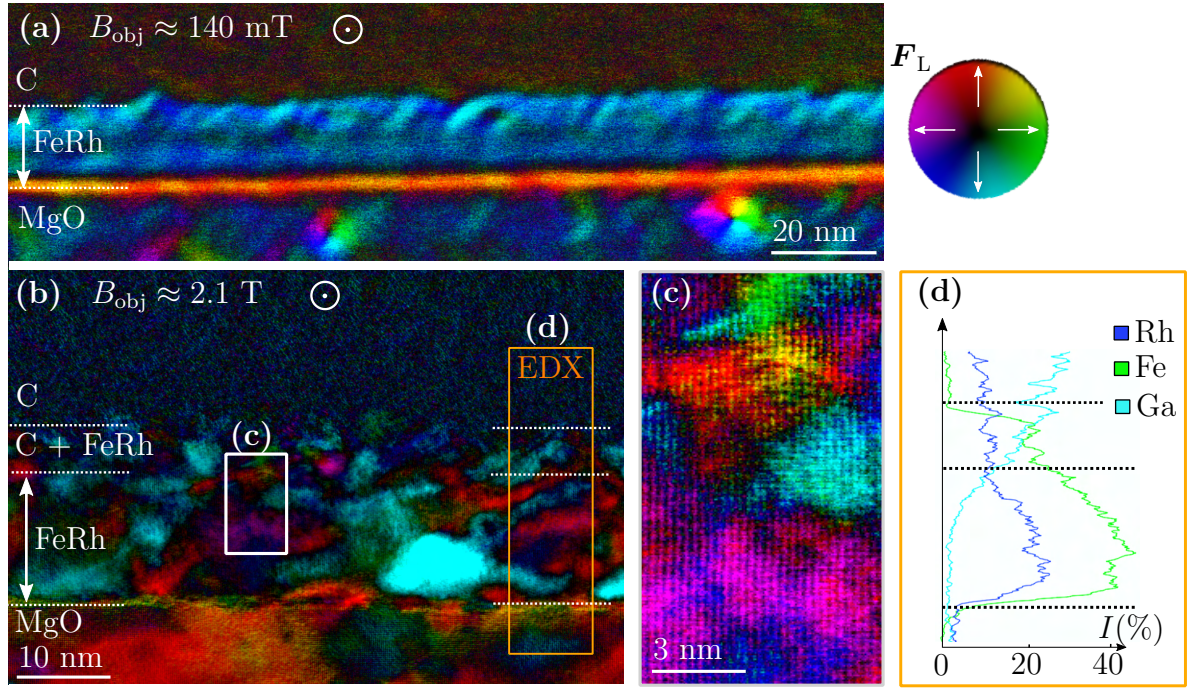
Figure 4.8: Magnetic properties of Fe-rich FM FeRh thin film. (a) LM-DPC scan of FM FeRh showing a uniform signal across the layer suggesting a uniform magnetization of the layer. **(b)** DPC scan of the FM layer acquired upon strong objective field. The signal is dominated by strain fields. Indicated rectangles represent regions used for the DPC detail in **(c)** and the EDX scan in **(d)**. **(c)** Detail of DPC demonstrating the signal strength of the strain fields comparable to the atomic plane signal. **(d)** EDX profile showing atomic ratios of Fe, Rh, and Ga proving Fe-rich stoichiometry and thus confirming FM order of the thin film. Strong elemental intermixing is evident at the FeRh interface with the C capping due to the absence of the Pt capping layer on top of FeRh.

present within the specimen. Continual gradients show almost identical character to the strain fields observed by [11] in the case of strained CuMnAs. Figure 4.8 **(b)** further shows the area in a white rectangle magnified in the Figure 4.8 **(c)** and orange rectangle defining the area for EDX mapping provided in Figure 4.8 **(d)**. The detail of the DPC map provided in Figure 4.8 **(c)** shows that the signal strength of random strains is capable to hide the signal coming from the atomic planes. An EDX map of atomic ratios provided in Figure 4.8 **(d)** shows the dominance of Fe over Rh confirming the FM ordering of the layer. Significant elemental intermixing is visible at the interface with the carbon capping layer.

Analysis of AF FeRh

An LM-DPC image of the equiatomic FeRh layer in Figure 4.9 **(a)** shows a gradual contrast suggesting the absence of uniform magnetization. Based on that, we assume that the layer is in the AF phase. The AF FeRh typically adopts the G-type of AF, with atomic moment configuration illustrated in Figure 4.9 **(b)**. The FeRh lattice aligned along the [110] ZA gives uncompensated magnetic moments of the atomic columns along this direction. A small deviation from this orientation would result in observation of corresponding stripes, rather than spots, of the uncompensated moment, while the deviation
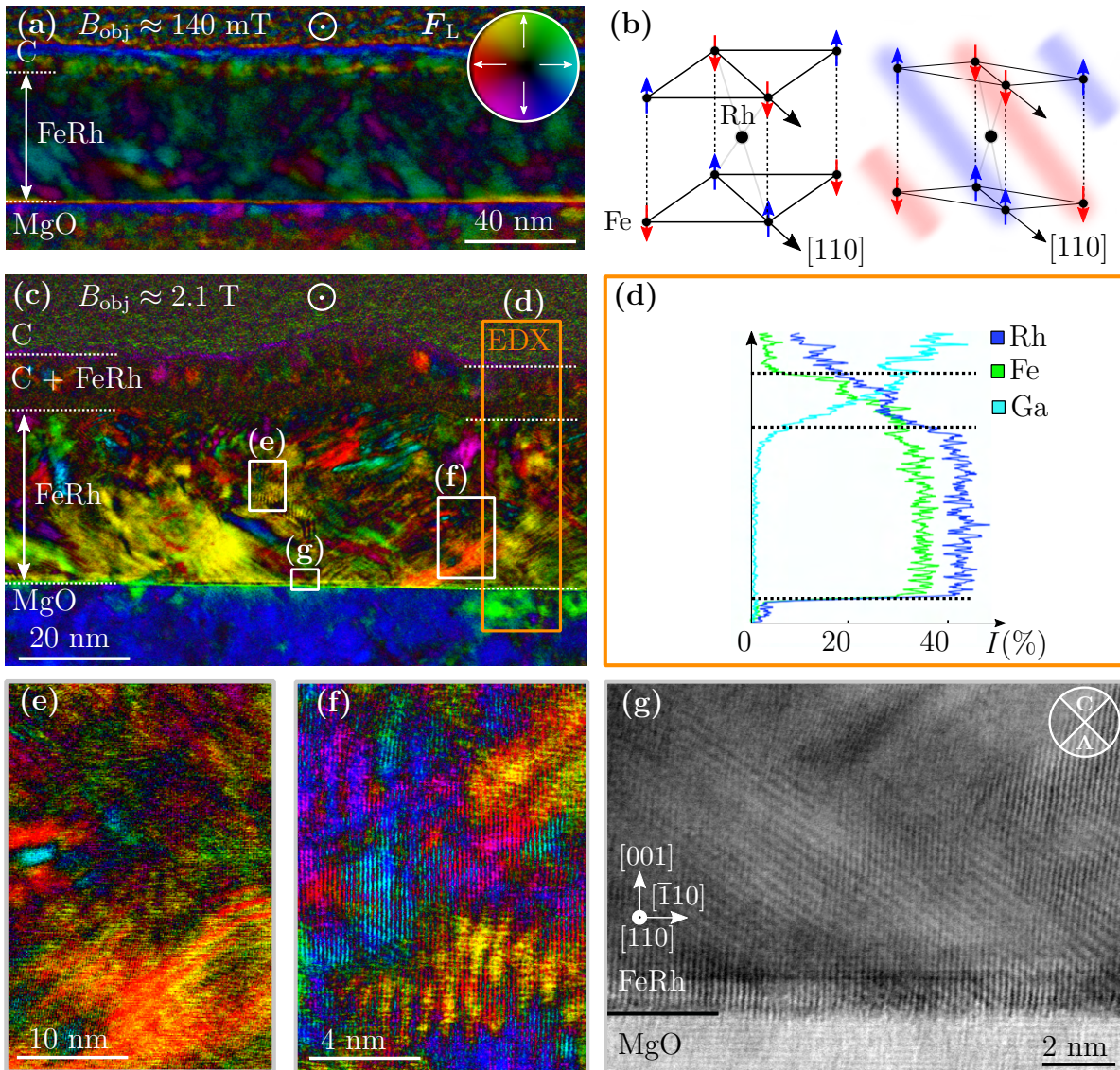
Figure 4.9: Magnetic imaging of the equiatomic AF FeRh thin film. (a) LM DPC scan of the FeRh thin layer with randomly distributed contrast suggesting AF ordering. **(b)** G-type configuration of AF moments expected for AF FeRh. A small deviation from the [110] ZA would result in the stripes of uniform signal of AF origin. **(c)** Scan of the DPC signal in the HR mode upon strong applied field showing significantly inhomogeneous contrast induced mainly by strain fields. Orange rectangle defines the region of the EDX analysis provided in **(d)**. Areas specified by the white rectangles are further evaluated in **(e)**, **(f)**, and **(g)**. **(d)** EDX scan of atomic ratios showing nearly equiatomic character of the FeRh layer together with a well-defined interface with MgO and a relatively low level of intermixing with the C capping. **(e)** Detail of the strain induced stripe like patterns present in the HR DPC scans. **(f)** Comparison of the DPC signal strength of the electrical fields from atomic planes with the strain induced contrast. **(g)** 1D DPC signal from A and C segments of the DPC detector demonstrating a possible candidate for the stripe like AF signal. The possible origin of this stripe-like signal is illustrated in **(b)**.

from the ZA reduces the effect of diffraction contrast. A DPC scan along this lattice direction is provided in Figure 4.9 **(c)**. We observe even more complex distribution of the DPC signal within the layer compared to Figure 4.9 **(a)**. Orange rectangle shows the area used for EDX mapping provided in Figure 4.9 **(d)**, and the regions surrounded by white rectangles are magnified in the 4.9 **(e)**, **(f)** and **(g)**. The EDX map of atomic ratios showed in Figure 4.9 **(d)** confirms a perfectly uniform, nearly equiatomic character of the FeRh thin layer. Here we assume certain discrepancy coming from the EDX quantification resulting in an offset between the Fe and Rh signals. The widened interface of the FeRh with the C capping indicates interfacial intermixing due to the absence of a Pt capping layer. Altogether, the chemical analysis supports the hypothesis of the FeRh layer to be AF. Magnified scans in Figures 4.9 **(e)**, **(f)** and **(g)** provide a closer look at the complex DPC signal structure. Figure 4.9 **(e)** shows a highly inhomogeneous signal including a strain-induced stripe-like pattern reminding a Moiré pattern [66]. Similarly, Figure 4.9 **(e)** provides this stripe-like pattern overlapped with the vertically aligned atomic planes. Undistinguishable atomic columns suggest a small deviation away from the [110] ZA. Finally, Figure 4.9 **(e)** shows a subtraction of the signal acquired from A and C segments, which corresponds to a 1D DPC signal. This image display a regular, relatively weak stripe-like signal with stripe spacing corresponding to approximately two atomic planes. Such spacing seems too low to be caused by the Moiré effect. Besides the other phenomena originating from the lattice properties, the signal may arise from the AF magnetic ordering of the sample. The potential origin of such a stripe-like pattern is schematically provided in Figure 4.9 **(b)**.

In summary, DPC represents a powerful tool for imaging the electric and magnetic fields in TEM compatible samples. However, the studied system of FeRh suffers from a tremendous amount of parasitic signals induced by internal lattice strain. The FM phase of FeRh can be relatively well distinguished. However, a reliable analysis of AF ordering using HR DPC needs to be further verified by analyzing other AF materials with reduced parasitic signals. Nevertheless, atomically resolved study of magnetic configurations in TEM would represent a revolutionary tool-set towards a more profound understanding of nanomagnetism, particularly in the rapidly evolving area of AF material research. Future development of the atomic-resolution field-free imaging in TEM has the potential to expand the applicability of HR DPC even beyond AF towards more conventional FM.

4.4.3. In-situ heating of FeRh

In-situ mapping of the phase transition in TEM requires using a built-in heating element in the vicinity of the specimen. For this purpose, we used the Fusion Select system by the Protochips company introduced in Figure 4.1. The unconventional sample fabrication process was in detail presented in Figure 4.4 including the temperature dependence of magnetic properties of the bulk specimen used for lamella fabrication. Analogically to the previous studies, [121, 123, 124], a 60 nm thick FeRh layer with the transition well above the room temperature was chosen for the analysis. Since there is no option for sample cooling, a relatively high transition temperature is required due to the significant drop in the transition temperature previously observed in spatially confined FeRh.

The thermal evolution of the DPC signal across the FeRh layer is provided in Figure 4.10. The FeRh thin layer corresponds to a region between the MgO substrate
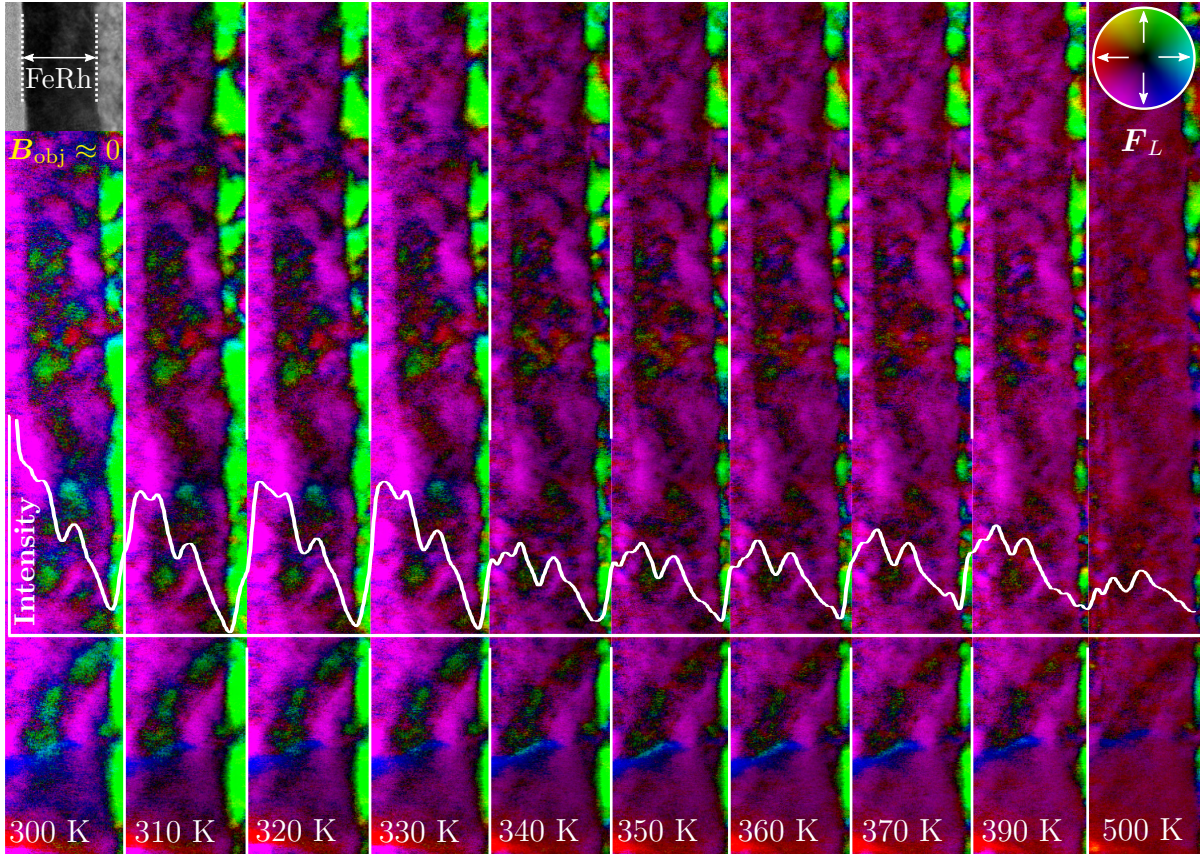
Figure 4.10: Temperature evolution of the field-free DPC signal. In-situ mapping of the DPC signal upon FeRh stripe heating. The FeRh layer profile is indicated in the top left corner by the TEM image. Absence of any increase of the DPC contrast change upon heating confirms the presence of FM phase across the studied temperature range. The intensity profile acquired from the horizontal white line shows the gray-scale intensity profile attenuation upon sample heating, which is typical for FM order.

exhibiting the bright green contrast and the capping layer possessing the purple signal. The TEM micrograph inset indicates the sample configuration in the top left corner. All DPC scans were acquired under field-free conditions. Temperature evolution of DPC does not show any significant signal change upon heating from room temperature up to 500 K, which denies the presence of MPT within the FeRh layer with increasing temperature. Besides that, DPC shows apparent attenuation of the signal within the FeRh layer. An intensity profile in the image shows the greyscale level of the acquired DPC signal qualitatively corresponding to the DPC signal strength. The profile was taken along the indicated horizontal white line. The attenuation of the FM magnetization is characteristic for FM order response to increasing temperature. These aspects confirm the FM character of the lamella across the studied temperature range.

The in-situ experiment in TEM confirmed the results published by [121], where the magnetization of the sample within the lamella is inconsistent with the VSM data of the thin film (Fig. 4.4 **(e)**). Such inconsistency most probably arises from the sample fabrication process introduced in 4.4. Loading the lamella onto the chip requires precise navigation within the dual-beam setup requiring both SEM and FIB scanning. The level of ion beam exposure in this FeRh layer is undoubtedly much more significant than

conventional lamella fabrication, which may result in substantial modification of the magnetic properties in FeRh films. This experiment corresponds well with the trend provided in section 3.4.2, showing that significant shifts of the transition temperature appear only in the FIB-made lamellae during in-situ TEM analysis. We conclude that ion irradiation has to be considered regarding the MPT shift on top of the strain relaxation phenomena. FIB irradiation is crucial, particularly during unconventional lamella fabrication, such as for the in-situ analysis. This result further highlights the importance of the TEM sample fabrication process. Recently, lattice reconstruction by annealing was proven to recover the ordered lattice of the specimen [124]. This restoration process may represent the critical step for successful in-situ MPT mapping in FeRh using TEM.

To sum up, the presented TEM study of magnetic behavior in FeRh thin films combined with in-situ sample heating confirms the inconsistency between magnetic properties of bulk and electron transparent geometry of the same specimen. Although the mapping of MPT in FeRh was not accomplished, we confirm the strong effect of ion irradiation during the unconventional sample fabrication required for in-situ analysis.

Apart from these difficulties, the in-situ TEM analysis represents a unique experimental tool allowing high-resolution analysis upon external control of the specimen. We characterized the sample fabrication process allowing simultaneous in-situ TEM analysis upon heating and biasing of the TEM specimen. We successfully tested the heating process, which confirmed previously published results. Following experiments will be aimed towards unique in-situ electrical biasing of the thin films in TEM. This unconventional tool expands the list of possible experiments, which can be performed within the used TEM setup.

Conclusion

This thesis presents a comprehensive TEM analysis of metamagnetic FeRh thin films, their structural, elemental, and particularly, magnetic properties. This analysis is supported by the evaluation of possible TEM sample fabrication processes that are of great significance for successful TEM analysis. In addition to the summary of the state of the art of TEM magnetic imaging, we have attempted to analyze not only the appearance of the conventional FM signal but uniquely to evaluate the presence of the AF signal using the STEM DPC technique. This analysis brings a novel approach to the metamagnetic phase transition analysis and further opens an unattended research area of atomic-scale magnetism using TEM. In addition, the in-situ heating process within the TEM setup, including the required sample fabrication process, is characterized.

The first thesis chapter introduces internal magnetic properties of both FM and AF magnetic orderings, explaining the features observable by magnetic imaging. Since the TEM conventionally operates in the sample immersion regime using the objective magnetic field, we also summarize the effects of this external field on both magnetic orderings. For both magnetic phases, we listed the conventional experimental techniques used for their magnetic imaging. In addition, the metamagnetic phase transition materials are introduced with a focus on the material properties of the FeRh system.

The second part is devoted to the general properties of TEM. We characterize the setup, TEM operation modes, as well as the principles of TEM image formation and sample fabrication processes. The following part reports the theoretical properties of electric and magnetic field mapping using TEM. Among various field sensitive techniques, the DPC is considered the most suitable for mapping metamagnetic materials due to the direct link between the DPC contrast and the magnetic field distribution. We evaluate high resolution DPC signal properties and the associated mathematical formalism of the field quantification based on a recent publication. Finally, we summarize pioneering studies towards AF phase imaging using TEM, as well as the state of the art of TEM analysis performed on FeRh systems.

The last part reports on the experimental evaluation of the TEM sample fabrication techniques and subsequent TEM analysis suitable for FeRh thin films. We compared the FIB-made lamella fabrication with the chemical detachment of the thin film from the substrate. It was shown that the lamellae made from MgO substrates used for FeRh growth generally suffer from significant bending induced by the lattice strain. Associated lattice deformation results in a strongly inhomogeneous diffraction signal. However, the versatility and reproducibility of the lamella fabrication process are preferred over uncontrollable topology of chemically etched freestanding FeRh layers. Hence, FIB-made lamellae are exclusively used for TEM analysis of FeRh systems. Finally, we present an unconventional lamella fabrication process for the in-situ heating/biasing TEM holder form the Protochips company. However, this process results in a substantially larger ion irradiation level than the conventional lamella fabrication process.

The ability of the DPC to map the magnetic field distribution was experimentally demonstrated on the amorphous ferromagnetic Py microstructures made by EBL. Within these, we are able to map the magnetic field distribution as well as to extract quantitative information about the field strength. Secondly, we analyzed the DPC signal of MgO monocrystals to map the influence of the sample crystallinity on the acquired DPC maps. Although we can map the electric field distribution up to the atomic level, the signal

is locally overwhelmed by the diffraction signal at the microscale. Subsequent analysis of the lamellae made from FeRh thin films grown on MgO confirmed the predominantly adopted BCC lattice of FeRh even in the spatially confined geometry. Although the lamellae were fabrication from films possessing metamagnetic behavior, a rare occurance of metastable FCC lattice of FeRh was confirmed in one of the samples. The presence of this phase suggests non-negligible effect of the sample fabrication process on the sample crystallography.

The characterization of FeRh magnetic properties via DPC was performed on two lamellae made from chemically different FeRh thin films. The FM character of an Fe-rich FeRh lamella was confirmed by the homogeneous DPC signal suggesting a uniform magnetization, which disappears upon application of strong objective field. In the lamella made from from equiatomic FeRh featuring AF order, the signal confirmed a lack of macroscopic magnetization. Instead, strain field induced, highly inhomogeneous DPC signal dominates, which makes the detection of AF signal even more challenging. However, atomic-scale DPC mapping then locally unveils a weak, periodic, stripe-like signal representing a potential candidate for the AF signal. Further analysis is required to confirm this hypothesis. Nevertheless, it represents another pioneering step towards atomically resolved magnetism.

The final part is dedicated to the DPC mapping of FeRh upon in-situ heating. The lamella was made from the FeRh thin film undergoing MPT well above room temperature. The attenuation of the DPC signal with increasing temperature typical for FM order indicates the absence of MPT in the lamella due to substantial ion irradiation during the sample fabrication process. However, this experimental configuration combining the versatility of the TEM analysis with an in-situ electrical control of the specimen enables many novel experiments to be performed.

The main limiting factor of the FeRh DPC imaging appears to be the strain-induced parasitic signal induced by the substrate. A well-controlled fabrication process of free-standing films may fully address this issue. Sample annealing represents a complementary approach to restore the unstrained crystallinity. Another limiting factor that has to be addressed is the DPC signal interpretation within more complex systems. An interplay between various signals originating from the structural, magnetic, or other sample properties must be fully understood.

In summary, this thesis represents an initial step towards high-resolution magnetic imaging using TEM. This type of analysis was previously limited due to the requirement of the field-free TEM operation mode, which is not needed for AF order imaging. Atomic-scale magnetic imaging would not only help to explain the coexistence between the magnetic phases in metamagnetic materials, but it would bring a new revolutionary tool towards a more profound understanding of nanomagnetism in general.

Bibliography

[1] WOLF, S. A. Spintronics: A Spin-Based Electronics Vision for the Future. *Science.* 2001, **294**(5546), 1488-1495. DOI: 10.1126/science.1065389. ISSN 0036-8075.

[2] HIROHATA, A., et al. Review on spintronics: Principles and device applications. *Journal of Magnetism and Magnetic Materials.* 2020, **509**. DOI: 10.1016/j.jmmm.2020.166711. ISSN 0304-8853.

[3] CHUMAK, A. V., et al. Magnon spintronics. *Nature Physics.* 2015, **11**(6), 453-461. DOI: 10.1038/nphys3347. ISSN 1745-2473.

[4] REZENDE, S., et al. Introduction to antiferromagnetic magnons. *Journal of Applied Physics.* 2019, **126**(15). DOI: 10.1063/1.5109132. ISSN 0021-8979.

[5] COLOMBO, M., et al. Biological applications of magnetic nanoparticles. Chemical Society Reviews. 2012, **41**(11). DOI: 10.1039/c2cs15337h. ISSN 0306-0012.

[6] JUNGWIRTH, T., et al. Antiferromagnetic spintronics. *Nature Nanotechnology.* 2016, **11**(3), 231-241. DOI: 10.1038/nnano.2016.18. ISSN 1748-3387.

[7] THIELE, J.-U., S. MAAT and E. E. FULLERTON. FeRh/FePt exchange spring films for thermally assisted magnetic recording media. *Applied Physics Letters.* 2003, **82**(17). DOI: 10.1063/1.1571232. ISSN 0003-6951.

[8] MARTI, X., et al. Room-temperature antiferromagnetic memory resistor. *Nature Materials.* 2014, **13**(4), 367-374. DOI: 10.1038/nmat3861. ISSN 1476-1122.

[9] ANNAORAZOV, M. P., et al. Alloys of the Fe-Rh system as a new class of working material for magnetic refrigerators. *Cryogenics.* 1992, **32**(10), 867-872. DOI: 10.1016/0011-2275(92)90352-B ISSN 0011-2275.

[10] STERN-TAULATS, E., et al. Barocaloric and magnetocaloric effects in $Fe_{49}Rh_{51}$. *Physical Review B.* 2014, **89**(21). DOI: 10.1103/PhysRevB.89.2141054. ISSN 1098-0121.

[11] KRIZEK, F., et al. Atomically sharp domain walls in an antiferromagnet. 2020. *Preprint, arXiv:* 2012.00894.

[12] CHAPMAN, J. N., et al. The direct determination of magnetic domain wall profiles by differential phase contrast electron microscopy. *Ultramicroscopy.* 1978, **3**, 203-214. DOI: 10.1016/S0304-3991(78)80027-8. ISSN 0304-3991.

[13] LAZIĆ, I., et al. Phase contrast STEM for thin samples: Integrated differential phase contrast. *Ultramicroscopy.* 2016, **160**, 265-280. DOI: 10.1016/j.ultramic.2015.10.011. ISSN 0304-3991.

[14] COEY, J. M. D. *Magnetism and magnetic materials.* Cambridge: Cambridge University Press, 2010. ISBN 05-218-1614-9.

[15] BLUNDELL, S. *Magnetism in condensed matter.* New York: Oxford University Press, 2001. ISBN 01-985-0592-2.

[16] SPALDIN, N. A. *Magnetic materials: fundamentals and applications.* 2nd ed. Cambridge: Cambridge University Press, 2011. ISBN 978-0-521-88669-7.

[17] EINSTEIN, A. and de HAAS, W. J. Experimenteller Nachweis der Ampèreschen Molekularströme. *Verhandl. Deut. Phys. Ges.*, 1915. **17**, 152–170.

[18] KITTEL, C. *Introduction to solid state physics.* 8th ed. Hoboken, NJ: Wiley, 2005. ISBN 978-0471415268.

[19] AHARONOV, Y. and BOHM, D. Significance of Electromagnetic Potentials in the Quantum Theory. *Physical Review.* 1959, **115**(3), 485-491. DOI: 10.1103/PhysRev.115.485. ISSN 0031-899X.

[20] RALPH, D.C. and M.D. STILES. Spin transfer torques. *Journal of Magnetism and Magnetic Materials.* 2008, **320**(7), 1190-1216. DOI: 10.1016/j.jmmm.2007.12.019. ISSN 0304-8853.

[21] STONER, E. C. Collective electron ferromagnetism. *Proc. Roy. Soc. London*, 1938, **372**(A165).

[22] ŽUTIĆ, I., FABIAN, J. and DAS SARMA, S. Spintronics: Fundamentals and applications. *Reviews of Modern Physics.* 2004, **76**(2), 323-410. DOI: 10.1103/RevModPhys.76.323. ISSN 0034-6861.

[23] COMSTOCK, R. L. Modern magnetic materials in data storage. *Journal of Materials Science: Materials in Electronics.* 2002, **13**(9), 509-523. DOI: 10.1023/A:1019642215245. ISSN 0957-4522.

[24] MORÓN, C., et al. Magnetic Sensors Based on Amorphous Ferromagnetic Materials: A Review. *Sensors.* 2015, **15**(11), 28340-28366. DOI: 10.3390/s151128340. ISSN 1424-8220.

[25] PARKIN, S. S. P., M. HAYASHI and L. THOMAS. Magnetic Domain-Wall Racetrack Memory. Science. 2008, 320(5873), 190-194. DOI: 10.1126/science.1145799. ISSN 0036-8075.

[26] TOMASELLO, R., et al. A strategy for the design of skyrmion racetrack memories. *Scientific Reports.* 2015, **4**(1). DOI: 10.1038/srep06784. ISSN 2045-2322.

[27] BREITENSTEIN, L., et al. Stray field of a Landau magnetization pattern. *Journal of Applied Physics.* 2008, **104**(8). DOI: 10.1063/1.3000479. ISSN 0021-8979.

[28] VAŇATKA, M., et al. Magnetic vortex nucleation modes in static magnetic fields. *AIP Advances.* 2017, **7**(10). DOI: 10.1063/1.5006235. ISSN 2158-3226.

[29] SANDRATSKII, L. M. Insight into the Dzyaloshinskii-Moriya interaction through first-principles study of chiral magnetic structures. *Physical Review B.* 2017, **96**(2). DOI: 10.1103/PhysRevB.96.024450. ISSN 2469-9950.

[30] GRAEF, M. de and Y. ZHU. *Magnetic imaging and its applications to materials.* Academic Press, 2001. ISBN 9780080531373.

[31] NÉEL, L. Influence des fluctuations du champ moléculaire sur les propriétés magnétiques des corp. *Ann. Phys.* 1932, **18**(10). DOI: 10.1051/anphys/193210180005. ISSN 0003-4169.

[32] NÉEL, L. Magnetism and the local molecular field. *Nobel Lectures, Physics 1963-1970.* 1970.

[33] NOGUÉS, J. and Ivan K SCHULLER. Exchange bias. *Journal of Magnetism and Magnetic Materials.* 1999, **192**(2), 203-232. DOI: 10.1016/S0304-8853(98)00266-2. ISSN 0304-8853.

[34] HOU, D., et al. Spin transport in antiferromagnetic insulators: progress and challenges. *NPG Asia Materials.* 2019, **11**(1). DOI: 10.1038/s41427-019-0135-9. ISSN 1884-4049.

[35] MÁCA, F., et al. Room-temperature antiferromagnetism in CuMnAs. *Journal of Magnetism and Magnetic Materials.* 2012, **324**(8), 1606-1612. DOI: 10.1016/j.jmmm.2011.12.017. ISSN 0304-8853.

[36] SIDDIQUI, S. A., et al. Metallic antiferromagnets. *Journal of Applied Physics.* 2020, **128**(4). DOI: 10.1063/5.0009445. ISSN 0021-8979.

[37] WADLEY, P., et al. Current polarity-dependent manipulation of antiferromagnetic domains. *Nature Nanotechnology.* 2018, **13**(5), 362-365. DOI: 10.1038/s41565-018-0079-1. ISSN 1748-3387.

[38] BODNAR, S., et al. Writing and reading antiferromagnetic Mn_2Au by Néel spin-orbit torques and large anisotropic magnetoresistance. *Nature Communications.* 2018, **9**(1). DOI: 10.1038/s41467-017-02780-x. ISSN 2041-1723.

[39] SCHREIBER, F., et al. Concurrent magneto-optical imaging and magneto-transport readout of electrical switching of insulating antiferromagnetic thin films. *Applied Physics Letters.* 2020, **117**(8). DOI: 10.1063/5.0011852. ISSN 0003-6951.

[40] DUINE, R. A., et al. Synthetic antiferromagnetic spintronics. *Nature Physics.* 2018, **14**(3), 217-219. DOI: 10.1038/s41567-018-0050-y. ISSN 1745-2473.

[41] PARKIN, S. S. P., N. MORE and K. P. ROCHE. Oscillations in exchange coupling and magnetoresistance in metallic superlattice structures: Co/Ru, Co/Cr, and Fe/Cr. *Physical Review Letters.* 1990, **64**(19), 2304-2307. DOI: 10.1103/PhysRevLett.64.2304. ISSN 0031-9007.

[42] O'GRADY, K., et al. Anisotropy in antiferromagnets. *Journal of Applied Physics.* 2020, **128**(4). DOI: 10.1063/5.0006077. ISSN 0021-8979.

[43] PAPANICOLAOU, N. Antiferromagnetic domain walls. *Physical Review B.* 1995, **51**(21), 15062-15073. DOI: 10.1103/PhysRevB.51.15062. ISSN 0163-1829.

[44] SHIINO, T., et al. Antiferromagnetic Domain Wall Motion Driven by Spin-Orbit Torques. *Physical Review Letters.* 2016, **117**(8). DOI: 10.1103/PhysRevLett.117.087203. ISSN 0031-9007.

[45] HEDRICH, N. et al. Nanoscale mechanics of antiferromagnetic domain walls. 2020. *Preprint, arXiv:* 2009.08986.

[46] CHEONG, S.-W., et al. Seeing is believing: visualization of antiferromagnetic domains. *Npj Quantum Materials.* 2020, **5**(1). DOI: 10.1038/s41535-019-0204-x. ISSN 2397-4648.

[47] YAN, H., et al. A piezoelectric, strain-controlled antiferromagnetic memory insensitive to magnetic fields. *Nature Nanotechnology.* 2019, **14**(2), 131-136. DOI: 10.1038/s41565-018-0339-0. ISSN 1748-3387.

[48] GRUTTER, A. J., et al. Strain-induced competition between ferromagnetism and emergent antiferromagnetism in (Eu,Sr) MnO_3. *Physical Review Materials.* 2018, **2**(9). DOI: 10.1103/PhysRevMaterials.2.094402. ISSN 2475-9953.

[49] LI, G. et al. Strain relaxation induced coexistence of ferromagnetism and antiferromagnetism in (110)-oriented $LuMnO_3$ thin films on $YAlO_3$: A first-principles study. *Physical Review B.* 2018, **97**(8). DOI: 10.1103/PhysRevB.97.085140. ISSN 2469-9950.

[50] ARREGI, J. A., O. CAHA and V. UHLÍŘ. Evolution of strain across the magneto-structural phase transition in epitaxial FeRh films on different substrates. *Physical Review B.* 2020, **101**(17). DOI: 10.1103/PhysRevB.101.174413. ISSN 2469-9950.

[51] ARREGI, J. A., et al. Magnetization reversal and confinement effects across the metamagnetic phase transition in mesoscale FeRh structures. *Journal of Physics D: Applied Physics.* 2018, **51**(10). DOI: 10.1088/1361-6463/aaaa5a. ISSN 0022-3727.

[52] UHLÍŘ, V., J. A. ARREGI and E. E. FULLERTON. Colossal magnetic phase transition asymmetry in mesoscale FeRh stripes. *Nature Communications.* 2016, **7**(1). DOI: 10.1038/ncomms13113. ISSN 2041-1723.

[53] AIKOH, K., et al. Quantitative control of magnetic ordering in FeRh thin films using 30 keV Ga ion irradiation from a focused ion beam system. *Journal of Applied Physics.* 2011, **109**(7). DOI: 10.1063/1.3549440. ISSN 0021-8979.

[54] BORDEL, C., et al. Fe Spin Reorientation across the Metamagnetic Transition in Strained FeRh Thin Films. *Physical Review Letters.* 2012, **109**(11). DOI: 10.1103/PhysRevLett.109.117201. ISSN 0031-9007.

[55] PAPON, P., J. LEBLOND and P. H. E. MEIJER. *The physics of phase transitions: concepts and applications.* 2nd rev. ed. New York: Springer-Verlag, 2006. ISBN 978-3-540-33389-0

[56] WOHLFARTH, E. P. and P. RHODES. Collective electron metamagnetism. *Philosophical Magazine.* 1962, **7**(83), 1817-1824. DOI: 10.1080/14786436208213848. ISSN 0031-8086.

[57] JACOBS, I. S. and P. E. LAWRENCE. Metamagnetic Phase Transitions and Hysteresis in FeCl 2. *Physical Review.* 1967, **164**(2), 866-878. DOI: 10.1103/PhysRev.164.866. ISSN 0031-899X.

[58] ROY, S. B. First order magneto-structural phase transition and associated multi-functional properties in magnetic solids. *Journal of Physics: Condensed Matter.* 2013, **25**(18). DOI: 10.1088/0953-8984/25/18/183201. ISSN 0953-8984.

[59] MAAT, S., J.-U. THIELE and E. E. FULLERTON. Temperature and field hysteresis of the antiferromagnetic-to-ferromagnetic phase transition in epitaxial FeRh films. *Physical Review B.* 2005, **72**(21). DOI: 10.1103/PhysRevB.72.214432. ISSN 1098-0121.

[60] CEBALLOS, A., et al. Effect of strain and thickness on the transition temperature of epitaxial FeRh thin-films. *Applied Physics Letters.* 2017, **111**(17). DOI: 10.1063/1.4997901. ISSN 0003-6951.

[61] BARUA, R., F. JIMÉNEZ-VILLACORTA and L. H. LEWIS. Predicting magnetostructural trends in FeRh-based ternary systems. *Applied Physics Letters.* 2013, **103**(10). DOI: 10.1063/1.4820583. ISSN 0003-6951.

[62] CASTIELLA, M., et al. Structural investigation of magnetic FeRh epitaxial films. *Materials Research Express.* 2015, **2**(8). DOI: 10.1088/2053-1591/2/8/086401. ISSN 2053-1591.

[63] SWARTZENDRUBER, L. J. The Fe-Rh (Iron-Rhodium) system. *Bulletin of Alloy Phase Diagrams.* 1984, **5**(5), 456-462. DOI: 10.1007/BF02872896. ISSN 1054-9714.

[64] SHIRANE, G., R. NATHANS and C. W. CHEN. Magnetic Moments and Unpaired Spin Densities in the Fe-Rh Alloys. *Physical Review.* 1964, **134**(6A), A1547-A1553. DOI: 10.1103/PhysRev.134.A1547. ISSN 0031-899X.

[65] ROSENBERG, M., et al. A Mössbauer spectroscopy and magnetic study of FeRh. *Journal of Magnetism and Magnetic Materials.* 1998, **177-181**. DOI: 10.1016/S0304-8853(97)00662-8. ISSN 0304-8853.

[66] WILLIAMS, D. B. and CARTER, C. B. *Transmission electron microscopy: a textbook for materials science.* Second edition. New York: Springer, 2009. ISBN 978-0-387-76500-6.

[67] BROGLIE, L. de. XXXV. A tentative theory of light quanta. *The London, Edinburgh, and Dublin Philosophical Magazine and Journal of Science.* 1924, **47**(278), 446-458. DOI: 10.1080/14786442408634378. ISSN 1941-5982.

[68] KLEIN, O. Quantentheorie und fünfdimensionale Relativitätstheorie. *Zeitschrift für Physik.* 1926, **37**(12), 895-906. DOI: 10.1007/BF01397481. ISSN 1434-6001.

[69] GORDON, W. Der Comptoneffekt nach der Schrödingerschen Theorie. *Zeitschrift für Physik.* 1926, **40**(1-2), 117-133. DOI: 10.1007/BF01390840. ISSN 1434-6001.

[70] DIRAC, P. A. M. The quantum theory of the electron. *Proceedings of the Royal Society of London. Series A, Containing Papers of a Mathematical and Physical Character.* 1928, **117**(778), 610-624. DOI: 10.1098/rspa.1928.0023. ISSN 0950-1207.

[71] LICHTE, H. and M. LEHMANN. Electron holography—basics and applications. *Reports on Progress in Physics.* 2008, **71**(1). DOI: 10.1088/0034-4885/71/1/016102. ISSN 0034-4885.

[72] RAYLEIGH, Lord. XXXI. Investigations in optics, with special reference to the spectroscope. *The London, Edinburgh, and Dublin Philosophical Magazine and Journal of Science.* 1879, **8**(49), 261-274. DOI: 10.1080/14786447908639684. ISSN 1941-5982.

[73] PENNYCOOK, S. J., et al. Materials Advances through Aberration-Corrected Electron Microscopy. *MRS Bulletin.* 2006, **31**(1), 36-43. DOI: 10.1557/mrs2006.4. ISSN 0883-7694.

[74] KISIELOWSKI, C., et al. Detection of Single Atoms and Buried Defects in Three Dimensions by Aberration-Corrected Electron Microscope with 0.5-Å Information Limit. *Microscopy and Microanalysis.* 2008, **14**(5). DOI: 10.1017/S1431927608080902. ISSN 1431-9276.

[75] KRIVANEK, O.L., T.C. LOVEJOY and N. DELLBY. Aberration-corrected STEM for atomic-resolution imaging and analysis. *Journal of Microscopy.* 2015, **259**(3), 165-172. DOI: 10.1111/jmi.12254. ISSN 00222720.

[76] RUTHERFORD, E. LXXIX. The scattering of α- and β-particles by matter and the structure of the atom. *The London, Edinburgh, and Dublin Philosophical Magazine and Journal of Science.* 1911, **21**(125), 669-688. DOI: 10.1080/14786440508637080. ISSN 1941-5982.

[77] BORN, M. and E. WOLF. *Principles of optics: electromagnetic theory of propagation, interference and diffraction of light.* 7th expanded ed. Cambridge: Cambridge Univ. Press, 1999. ISBN 05-216-4222-1.

[78] MASTERS, B. M. *Superresolution optical microscopy: The Quest for Enhanced Resolution and Contrast.* Springer, 2020. ISBN 978-3-030-21690-0.

[79] ROSE, H. and C. F. KISIELOWSKI. On the Reciprocity of TEM and STEM. *Microscopy and Microanalysis.* 2005, **11**(S02). DOI: 10.1017/S1431927605507761. ISSN 1431-9276.

[80] KRAUSE, F. and A. ROSENAUER. Reciprocity relations in transmission electron microscopy: A rigorous derivation. *Micron.* 2017, **92**, 1-5. DOI: 10.1016/j.micron.2016.09.007. ISSN 0968-4328.

[81] ZERNIKE, F. Das Phasenkontrastverfahren bei der mikroskopischen Beobachtung. *Z. Techn. Physik.* 1935, **16**(454). 454-457.

[82] MALAC, M. et al. Phase plates in the transmission electron microscope: operating principles and applications. *Microscopy.* 2021, **70**(1), 75-115. DOI: 10.1093/jmicro/dfaa070. ISSN 2050-5698.

[83] SCHERZER, O. The Theoretical Resolution Limit of the Electron Microscope. *Journal of Applied Physics.* 1949, **20**(1), 20-29. DOI: 10.1063/1.1698233. ISSN 0021-8979.

[84] KIRKLAND, E. J. *Advanced Computing in Electron Microscopy.* Springer, 2010. ISBN 978-1-4419-6532-5.

[85] PENNYCOOK, S. J. *Scanning Transmission Electron Microscopy: Imaging and Analysis.* Springer, 2011. ISBN 978-1-4419-7199-9.

[86] NELLIST, P.D. and S. J. PENNYCOOK. The principles and interpretation of annular dark-field Z-contrast imaging. *Advances in Imaging and Electron Physics.* 2000, **113**, 147-203. DOI: 10.1016/S1076-5670(00)80013-0. ISSN 1076-5670.

[87] ZHANG, H. K., et al. Novel techniques of preparing TEM samples for characterization of irradiation damage. *Journal of Microscopy.* 2013, **252**(3), 251-257. DOI: 10.1111/jmi.12085. ISSN 0022-2720.

[88] SEIDL, R. *Specimen Preparation for Transmission Electron Microscopy by Focused Ion Beam: Refinement of Post-Treatment using Focused Low Energy Argon Ion Milling.* Graz, 2016. Master's thesis. Graz University of Technology. Supervisor: Ao. Univ.-Prof. Dipl.-Ing. Dr. techn. Werner Grogger.

[89] *Omniprobe - Cu grids* [online]. 2spi, 2021. [cit. 2021-05-10]. Available from: https://www.2spi.com/item/1033c-xa.

[90] GORJI, S., et al. Nanowire facilitated transfer of sensitive TEM samples in a FIB. *Ultramicroscopy.* 2020, **219**. DOI: 10.1016/j.ultramic.2020.113075. ISSN 0304-3991.

[91] EDLER, T. and MAYR, S. G. Film Lift-Off from MgO: Freestanding Single Crystalline Fe-Pd Films Suitable for Magnetic Shape Memory Actuation - and Beyond. *Advanced Materials.* 2010, **22**(44), 4969-4972. DOI: 10.1002/adma.201002183. ISSN 0935-9648.

[92] *Holey carbon films - copper* [online]. Agar Scientific, 2021. [cit. 2021-05-14]. Available from: https://www.agarscientific.com/holey-carbon-films.

[93] *Lacey carbon films - copper* [online]. Agar Scientific, 2021. [cit. 2021-05-14]. Available from: https://www.agarscientific.com/lacey-carbon-films.

[94] *TEM Membrane Window Grids* [online]. 2spi, 2021. [cit. 2021-05-10]. Available from:https://www.2spi.com/category/grids-membrane-window/.

[95] MÜLLER, K., et al. Atomic electric fields revealed by a quantum mechanical approach to electron picodiffraction. *Nature Communications.* 2014, **5**(1). DOI: 10.1038/ncomms6653. ISSN 2041-1723.

[96] EDSTRÖM, A., et al. Quantum mechanical treatment of atomic-resolution differential phase contrast imaging of magnetic materials. *Physical Review B.* 2019, **99**(17). DOI: 10.1103/PhysRevB.99.174428. ISSN 2469-9950.

[97] BURNS, G. Atomic Shielding Parameters. *The Journal of Chemical Physics.* 1964, **41**(5), 1521-1522. DOI: 10.1063/1.1726113. ISSN 0021-9606.

[98] SHIBATA, N., et al. Electric field imaging of single atoms. *Nature Communications.* 2017, **8**(1). DOI: 10.1038/ncomms1563. ISSN 2041-1723.

[99] MÜLLER-CASPARY, K., et al. Measurement of atomic electric fields and charge densities from average momentum transfers using scanning transmission electron microscopy. *Ultramicroscopy.* 2017, **178**, 62-80. DOI: 10.1016/j.ultramic.2016.05.004. ISSN 0304-3991.

[100] WINKLER, F., et al. Quantitative measurement of mean inner potential and specimen thickness from high-resolution off-axis electron holograms of ultra-thin layered WSe_2. *Ultramicroscopy.* 2017, **178**, 38-47. DOI: 10.1016/j.ultramic.2016.07.016. ISSN 0304-3991.

[101] HAAS, B., et al. Direct comparison of off-axis holography and differential phase contrast for the mapping of electric fields in semiconductors by transmission electron microscopy. *Ultramicroscopy.* 2019, **198**, 58-72. DOI: 10.1016/j.ultramic.2018.12.003. ISSN 0304-3991.

[102] DENNEULIN, T., F. HOUDELLIER and M. HŸTCH. Differential phase-contrast dark-field electron holography for strain mapping. *Ultramicroscopy.* 2016, **160**, 98-109. DOI: 10.1016/j.ultramic.2015.10.002. ISSN 0304-3991.

[103] CHAPMAN, J. N. and M. R. SCHEINFEIN. Transmission electron microscopies of magnetic microstructures. *Journal of Magnetism and Magnetic Materials.* 1999, **200**(1-3), 729-740. DOI: 10.1016/S0304-8853(99)00317-0. ISSN 0304-8853.

[104] SHIBATA, N., et al. Atomic resolution electron microscopy in a magnetic field free environment. *Nature Communications.* 2019, **10**(1). DOI: 10.1038/s41467-019-10281-2. ISSN 2041-1723.

[105] OPHUS, C., et al. Recording and Using 4D-STEM Datasets in Materials Science. *Microscopy and Microanalysis.* 2014, **20**(S3), 62-63. DOI: 10.1017/S1431927614002037. ISSN 1431-9276.

[106] YANG, H., et al. 4D STEM: High efficiency phase contrast imaging using a fast pixelated detector. *Journal of Physics: Conference Series.* 2015, **644**. DOI: 10.1088/1742-6596/644/1/012032. ISSN 1742-6588.

[107] YANG, H., et al. Efficient phase contrast imaging in STEM using a pixelated detector. Part II: Optimisation of imaging conditions. *Ultramicroscopy.* 2015, **151**, 232-239. DOI: 10.1016/j.ultramic.2014.10.013. ISSN 0304-3991.

[108] SCHATTSCHNEIDER, P., et al. Detection of magnetic circular dichroism using a transmission electron microscope. *Nature.* 2006, **441**(7092), 486-488. DOI: 10.1038/nature04778. ISSN 0028-0836.

[109] CHAPMAN, J. N. The investigation of magnetic domain structures in thin foils by electron microscopy. *Journal of Physics D: Applied Physics.* 1984, **17**(4), 623-647. DOI: 10.1088/0022-3727/17/4/003. ISSN 0022-3727.

[110] PENG, L.-C., et al. Lorentz transmission electron microscopy studies on topological magnetic domains. *Chinese Physics B.* 2018, **27**(6). DOI: 10.1088/1674-1056/27/6/066802. ISSN 1674-1056.

[111] SCHNARS, U. and W. JUEPTNER. *Digital holography: digital hologram recording, numerical reconstruction, and related techniques.* Berlin: Springer, 2005. ISBN 35-402-1934-X.

[112] WOLF, D., et al. Electron holographic tomography. *Current Opinion in Solid State and Materials Science.* 2013, **17**(3), 126-134. DOI: 10.1016/j.cossms.2013.05.002. ISSN 13590286. Dostupné z: doi:10.1016/j.cossms.2013.05.002

[113] RUSZ, J., et al. Achieving Atomic Resolution Magnetic Dichroism by Controlling the Phase Symmetry of an Electron Probe. *Physical Review Letters.* 2014, **113**(14). DOI: 10.1103/PhysRevLett.113.145501. ISSN 0031-9007.

[114] THERSLEFF, T., et al. Detection of magnetic circular dichroism with sub-nanometer convergent electron beams. *Physical Review B.* 2016, **94**(13). DOI: 10.1103/PhysRevB.94.134430. ISSN 2469-9950.

[115] WANG, Z., et al. Atomic scale imaging of magnetic circular dichroism by achromatic electron microscopy. *Nature Materials.* 2018, **17**(3), 221-225. DOI: 10.1038/s41563-017-0010-4. ISSN 1476-1122.

[116] ALI, H. et al. Atomic resolution energy-loss magnetic chiral dichroism measurements enabled by patterned apertures. *Physical Review Research.* 2020, **2**(2). DOI: 10.1103/PhysRevResearch.2.023330. ISSN 2643-1564.

[117] VERBEECK, J., et al. Optimal aperture sizes and positions for EMCD experiments. *Ultramicroscopy.* 2008, **108**(9), 865-872. DOI: 10.1016/j.ultramic.2008.02.007. ISSN 0304-3991.

[118] LIDBAUM, H., et al. Quantitative Magnetic Information from Reciprocal Space Maps in Transmission Electron Microscopy. *Physical Review Letters.* 2009, **102**(3). DOI: 10.1103/PhysRevLett.102.037201. ISSN 0031-9007.

[119] LOUDON, J. C. Antiferromagnetism in NiO Observed by Transmission Electron Diffraction. *Physical Review Letters.* 2012, **109**(26). DOI: 10.1103/PhysRevLett.109.267204. ISSN 0031-9007.

[120] MCLAREN, M. J. *Transmission Electron Microscope Characterisation of Iron-Rhodium Epilayers.* 2014. Doctoral thesis. The University of Leeds. Supervisors: R. M. D. Brydson and C. H. Marrows.

[121] ALMEIDA, T. P., et al. Quantitative Differential Phase Contrast Imaging of the Magnetostructural Transition and Current-driven Motion of Domain Walls in FeRh Thin Films. *Microscopy and Microanalysis.* 2018, **24**(S1), 936-937. DOI: 10.1017/S1431927618005172. ISSN 1431-9276.

[122] KANDE, D., et al. Enhanced B2 Ordering of FeRh Thin Films Using B2 NiAl Underlayers. *IEEE Transactions on Magnetics.* 2011, **47**(10). DOI: 10.1109/TMAG.2011.2157963. ISSN 0018-9464.

[123] GATEL, C., et al. Inhomogeneous spatial distribution of the magnetic transition in an iron-rhodium thin film. *Nature Communications.* 2017, **8**(1). 10.1038/ncomms15703. ISSN 2041-1723.

[124] ALMEIDA, T. P., et al. Direct visualization of the magnetostructural phase transition in nanoscale FeRh thin films using differential phase contrast imaging. *Physical Review Materials.* 2020, **4**(3). DOI: 10.1103/PhysRevMaterials.4.034410. ISSN 2475-9953.

[125] FAN, R., et al. Ferromagnetism at the interfaces of antiferromagnetic FeRh epilayers. *Physical Review B.* 2010, **82**(18). DOI: 10.1103/PhysRevB.82.184418. ISSN 1098-0121.

[126] HARADA, K., et al. Double-biprism electron interferometry. *Applied Physics Letters.* 2004, **84**(17), 3229-3231. DOI: 10.1063/1.1715155. ISSN 0003-6951.

[127] MOTYČKOVÁ, L. *Magnetic properties of self-assembled FeRh nanomagnets.* 2020. Master's thesis. Brno University of Technology. Supervisor M.Sc. Jon Ander Arregi Uribeetxebarria.

List of abbreviations

AF	Antiferromagnetism, antiferromagnetic
AF-FM	Metamagnetic phase transition from AF to FM phase
BF	Bright field
BFP	Back focal plane
CBED	Convergent beam electron diffraction
CCD	Charge coupling device
CMOS	Complementary metal-oxide-semiconductor
CL	Cathodoluminiscence
COM	Center of mass
CTEM	Conventional transmission electron microscopy
CTF	Contrast transfer function
DF	Dark field
DFT	Density functional theory
DPC	Differential phase contrast
EBID	Electron beam induced deposition
EBL	Electron beam lithography
EDX	Energy dispersive X-ray spectroscopy
EELS	Electron energy loss spectroscopy
EH	Electron holography
EMCD	Electron magnetic circular dichroism
FEG	Field-emission gun
FeRh	Iron-rhodium
FIB	Focused ion beam
FM	Ferromagnetism, ferromagnetic
FT	Fourier transform
FT^{-1}	Inverse Fourier transform
GIS	Gas injection system

HAADF	High angle angular dark field
HR	High-resolution
HRTEM	High resolution transmission electron microscopy
IBID	Ion beam induced deposition
IP	In plane
LTEM	Lorentz transmission electron microscopy
MgO	Magnesium oxide
MIP	Mean inner potential
MPT	Metamagnetic phase transition
NM	Nano-manipulator
OOP	Out of plane
PCTF	Phase contrast transfer function
SAED	Selected area electron diffraction
SAF	Synthetic antiferromagnet
SEM	Scanning electron microscope
STEM	Scanning transmission electron microscopy
TEM	Transmission electron microscopy
XMCD	X-ray magnetic circular dichroism
XMLD	X-ray magnetic linear dichroism
Z	Atomic number